Supersonic Jet Impingement on a Flat Surface at Angles from -5^0 to -30^0

by

Amro Mohammad Al-Qutub

A Thesis Presented to the

FACULTY OF THE COLLEGE OF GRADUATE STUDIES

KING FAHD UNIVERSITY OF PETROLEUM & MINERALS

DHAHRAN, SAUDI ARABIA

In Partial Fulfillment of the
Requirements for the Degree of

MASTER OF SCIENCE

In

MECHANICAL ENGINEERING

August, 1992

Order Number 1354089

Supersonic jet impingement on a flat surface at angles from −5° to 30°

Al-Qutub, Amro Mohammad, M.S.

King Fahd University of Petroleum and Minerals (Saudi Arabia), 1992

U·M·I
300 N. Zeeb Rd.
Ann Arbor, MI 48106

SUPERSONIC JET IMPINGEMENT ON A FLAT SURFACE AT ANGLES FROM -5° TO 30°

BY

AMRO MOHAMMAD AL-QUTUB

A Thesis Presented to the

FACULTY OF THE COLLEGE OF GRADUATE STUDIES

KING FAHD UNIVERSITY OF PETROLEUM & MINERALS

DHAHRAN, SAUDI ARABIA

In Partial Fulfillment of the
Requirements for the Degree of

MASTER OF SCIENCE

In

MECHANICAL ENGINEERING

AUGUST, 1992

KING FAHD UNIVERSITY OF PETROLEUM & MINERALS

DHAHRAN, SAUDI ARABIA

This thesis, written by **AMRO MUHAMMAD KHALID AL-QUTUB**, under the direction of his Thesis Committee, and approved by all the members, has been presented to and accepted by the Dean, College of Graduate Studies, in partial fulfillment of the requirements for the Degree of **MASTER OF SCIENCE IN MECHANICAL ENGINEERING.**

Thesis Committee

Chairman (Dr. Mohammad Budair)

Member (Dr. Hassan Badr)

Member (Dr. M.A. Z. Hassan)

Dr. Abdulghani A. Al-Farayedhi
Department Chairman

Dr. Ala H. Al-Rabeh
Dean, College of Graduate Studies

Date: Aug. 16, 1992.

ACKNOWLEDGEMENT

Praise and gratitude be to Allah the Almighty, with whose gracious help it was possible to accomplish this work. Acknowledgement is due to King Fahd University of Petroleum & Minerals for extending all the facilities and providing financial support.

I would like to express my appreciation and gratefulness for to my advisor and committee chairman Dr. Mohammad Budair. His guidance, innovative and pragmatic suggestions and continuous encouragement were of vital help in achieving this goal. I am also thankful to my committee members Dr. Mohammed A.Z. Hasan and Dr. Hasan Badr for their critical evaluation and suggestions for the improvement of the work. Special thanks are due to Dr. W. Stahl for initiating me into this research and for his valuable guidance and support.

Also, thanks are due to Mr. Bakr, the Workshop Supervisor, for his cooperation and help in constructing the mechanical layout of the experiment. Last, but not least, I am thankful to all the faculty, staff, colleagues and friends who made my stay at King Fahd University of Petroleum & Minerals a memorable and valuable experience.

TABLE OF CONTENTS

All dimensions mentioned in mm. unless otherwise stated.

LIST OF TABLES

LIST OF FIGURES

NOTATIONS

a: Acoustic speed.

A^*: Area of the exit nozzle throat.

A_t: Area of the tube of the tunnel.

b: Plate length.

c: Distance between the plate center of gravity and axis of rotation.

C_F: Normal force coefficient.

C_{FP}: Normal force coefficient by pressure integration.

C_{FS}: Normal force coefficient by strain gage.

C_{FT}: Theoretical normal force coefficient.

d_{max}: Maximum deflection of the cantilever.

D_n: Nozzle exit diameter.

e: Plate thickness.

E: Modulus of elasticity.

ε: Strain.

f: Frequency.

F_1,F_2: Forces on the cantilever beam due to setting L_1 and L_2.

F_p: Normal force on the plate surface.

γ: Gas constant.

h: Distance between nozzle lip and plate leading edge.

I_o: Plate moment of inertia about its rotating axis.

K_t: Torsional stiffness of the cantilever about the plate rotating axis.

L: Length of the cantilever

L_1,L_2: Distance between the axis of the Y-bearings and the cantilever bearing.

L_T: Length of the tube tunnel.

L_p: Distance between the axis of the Y-bearing and the normal force acting on the plate.

m: Mass of the plate.

M_o: Moment about the plate axis of rotation.

M: Local Mach number.

M_n: Mach number of the nozzle exit.

M_t: Mach number of the flow in the tube of the tunnel.

n: Cycle number of the jet flow.

P: Plate surface pressure (gage).

P_o: Stagnation pressure of the jet.

P_e: Static pressure of the jet at the nozzle exit.

P_p: Pitot pressure of the free jet.

P_t: Wind tunnel tube pressure.

PR: The ratio of jet pressure at the nozzle exit to the surrounding pressure (underexpansion ratio).

R: Universal gas constant.

s: Height of the cantilever.

σ_t: Tensile stress.

σ_y: Yield strength.

t: Time.

t_j: Jet duration.

T_t: Total temperature of gas inside the tube.

τ_s: Shear stress.

θ: Angle between the jet axis and the plate surface.

$\Delta\theta$: Angular deflection of the plate.

w: Width of the cantilever.

X: Coordinates dimension along the flow centerline on the plate surface referenced at jet centerline intersection.

X_p: Coordinates dimension along the flow of centerline on the plate surface referenced at the leading edge.

Y: Coordinates dimension on the plate surfaces vertical to X-axis and referenced on the centerline.

Z_n: Axial distance from the jet nozzle.

خلاصة الرساله

عنـــوان الرســاله : دراسـة عنـد اصطدام نفـات ذو سـرعة
جريان فـوق صوتيـه علـي سطح مسـتوى
عنـــد زوايـا تتراوح مـــن - ٥° إلـى ٣٠°.

اســم الطالب : عمـرو محمـد خـالـد القطـب
التخـصـص : هنـدسـة ميكـانيكيـه .

تاريخ الدرجـه : صفـر ١٤١٣ هـ / اغسطـس ١٩٩٢ م .

ان القوة العامودية وتوزيع الضغط على سطح مستوى الناتج عند اصطدام نفاث ذو سرعة جريان فوق صوتيه عند زوايا اقل من ٢٠° لم تخضع من قبل للبحث التجريبي . ويهدف هذا البحث الى دراسة معامل القوه العمودي وتوزيع الضغط على هذا السطح المستوى عند زوايا تتراوح من - ٥° الى ٣٠° بالاضافه الى توضيح العلاقه بين توزيع الضغط ونمط الجريان السطحي . وتتضمن هذه ايضا عدة تجارب وهي قياس مدى استجابه انبوبه بيتو لقياس الضغط ومعايرة انبثاق المنفث وقياس ضغط انبوبه بيتو على طول محور المنفث . وقد تم قياس القوة العمودية على السطح باستخدام مقياس جهد الاستطاله . وقد ابدت نتائج قياس القوة العمودية للزوايا الموجبه ان معامل القوة الفعلي اكبر من معامل القوة المتوقع نظرياً خاصه عندما تكون الزاويه تساوي او اقل ٢٠° حيث يكون الاختلاف أكثر من ٢٥ ٪ . أيضا نتائج تجربه الحاله المقارنه لتجربه لامونت وهنت عند الزوايه كانت مشابهة لنتائجهم .

درجة الماجستر في العلوم
جامعة الملك فهد للبترول والمعادن
الظهران - المملكة العربية السعودية
صفر ١٤١٣ هـ / اغسطس ١٩٩٢ م .

THESIS ABSTRACT

NAME OF STUDENT : AMRO MOHAMMAD AL-QUTUB

TITLE OF STUDY : SUPERSONIC JET IMPINGEMENT ON A FLAT SURFACE AT ANGLES FROM -5° TO 30°

MAJOR FIELD : MECHANICAL ENGINEERING

DATE OF DEGREE : JULY, 1992

The normal force and pressure distribution acting on a flat plate resulting from underexpanded supersonic jet impingement at angles lower than 20° has never been experimentally investigated. The objectives of the present investigation are to study the normal force coefficient and pressure distribution on a flat-surface at angles from -5° to 30° as well as the correlation between the surface flow visualization and the surface pressure distribution. This investigation also includes Pitot response measurement, jet calibration and Pitot pressure measurement along the free jet axis. The normal force was measured using a strain-gage. Results showed that for positive angles, the actual force coefficient C_{FS} was larger than the one predicted theoretically, especially at angles $\theta \leq 20°$ where the deviation was larger than 25%. Moreover, the results of the comparative case with Lamont and Hunt [2] at $\theta = 30°$ were in good agreement.

MASTER OF SCIENCE

KING FAHD UNIVERSITY OF PETROLEUM & MINERALS

DHAHRAN, SAUDI ARABIA

1. INTRODUCTION

Recent developments in the technology of rocket engine enhanced the motivation for more experimental studies. These studies have many actual applications, such as the multi-stage rocket separation, space model attitude control thrusters and impingement of missiles exhaust on the fuselage, wing and tail sections of fighter aircrafts. The thrusters exhaust on controlling fins of large rockets, for instance, can be used to improve their maneuverability when flying at low speeds.

When an underexpanded supersonic jet impinges on a flat surface at different inclinations in the near field (supersonic domain of the jet), a very complex flow structure forms on the surface. This is due to the interaction between the shocks reflected from the flat surface and the shock system of the free jet.

The first experimental study was conducted by Hinderson in 1966 [1]. He investigated under-expanded supersonic jet impingement on a flat surface at inclinations ranging from $\theta = 20^{\circ}$ to 90°. He applied uniform jet with different Mach numbers i.e., 1.8, 2.01 and 2.14. He used widely spaced pressure tappings to read the surface pressure and consequently had a lack of definition for the pressure distribution [2]. In a similar study, Coleman and Richard [3] used a sonic orifice to produce a jet at under-expanded ratios from 1.1 to 3.57 with the flat surface inclined at angles between 15° and 90° and at distances from the nozzle exit of 1.96 to 58.7 nozzle diameters. Their main concern was to find regions of separation in the flow and radial velocity gradient at the

centerline. Their results included the pressure distribution on the flat surface near the point of impingement. In 1980, Lamont and Hunt [2] in their investigation of the same phenomenon, studied the under-expanded supersonic jet impingement on a flat plate at inclinations from 30° to 90° at distances from the nozzle exit of the jet ranging from 2 to 15 nozzle diameters. From measurements of pressure distribution on the plate and shadow graph pictures, they identified the maximum pressure regions, stagnation bubbles and plate shock locations for different under-expanded ratios of the jet. From integration of pressure distribution on the plate, they found that the normal force and normal force coefficient are independent of the plate distance from the jet nozzle. This was in good agreement with the Lockheed bloom program. Furthermore, they developed a simplified theoretical expression for prediction of normal force coefficient on a flat plate.

Lloyd and Viendra [4] studied the pressure pulsation on a flat plate normal to an under-expanded supersonic jet . They used a sonic orifice to produce a jet with under-expansion ratios ranging from 1.8 to 8 and a spacing of the plate at 1 and 1.5 nozzle diameters downstream the nozzle exit. Using a high response pressure transducer, (rise time of 2 μ sec. and frequency response up to 40 KHz), mounted flush on the surface, they measured the pressure on the plate. They concluded that for the given conditions the peak pressure fluctuation frequencies ranged from 8.75 KHz to 20.6 KHz.

More recently, Koppenvallner, Rammenzweig and Stahl [5] studied the impingement of underexpanded supersonic jet on a flat plate

at angles less than 15°. Unlike the previous investigations, where continuous jet was used, they used impulsive type of jet produced by 25 meter long and 0.025 meter in diameter Ludwieg tube wind tunnel. The duration of the jet was close to 0.14 sec with fully developed flow period close to 0.1 sec. Their investigation included inclination angles from 20° down to -5° for the flat plate. The Ludwieg tube was operated at different pressures, ranging from 30 bar to 100 bar and a Mach number of 2.5 at the nozzle exit.

Using shadow-graph techniques and oil surface flow visualization, they observed that even at low and negative angles of the flat plate to the jet axis, the jet may still have a considerable pressure influence on the flat plate. To confirm this, they recommended that pressure measurements are needed at such inclinations.

Normal force and pressure distribution on a flat plate under the impingement of a supersonic flow at inclinations less than 20° have not been experimentally investigated. Inclinations of less than 20° have a special application to the launching of missiles from a fighter such as shown in Figures 1.1, 1.2, and to the feasibility of using thrusters directed to fins to control large rockets during their initial low-speed trajectories.

The present investigation aims at studying experimentally the flow phenomenon of supersonic jet impingement on a flat plate at angles of attack ranging between -5° and +30°. The data include surface pressure, and normal force measurements in addition to the surface flow visualization. It is hoped that such additional information will enhance

the understanding of this complex flow phenomenon. The experiments involved in this investigation are:

1. Free jet calibration
2. Surface flow visualization
3. Evaluation and selection of pressure measuring technique
4. Surface pressure measurement
5. Normal force measurement.

2. EXPERIMENTAL PROCEDURE AND APPARATUS

2.1 Ludwieg-Tube Tunnel

The experimental work was conducted using the Ludwieg-tube tunnel [6] situated in the wind tunnel laboratory at King Fahd University of Petroleum & Minerals (KFUPM). The tunnel was designed by Professor W. Stahl and built in the Mechanical Engineering Shop of the Mechanical Engineering Department. It consists of a 24 meter long cylindrical tube of inside diameter of 34 mm with one end closed and the other end connected to a supersonic nozzle (Fig. 2.2). The flow through the nozzle is controlled by an electromagnetic valve and a simple electric-time-delay system.

The schematics of nozzle configuration electromagnetic valve and the tunnel layout are shown in Figs. 2.1 and 2.2. The tunnel provided an under expanded supersonic jet with a Mach number of 2.57.

2.2 Pitot Response Measurement

Since all pressure measurements had to be taken over a very short duration (0.126 sec), an experiment was designed to measure the pitot response to a sudden change in pressure. Three pitot-tube configurations were designed and constructed to be fitted to a pressure transducer, type 8206 R-100, as shown in Fig. 2.3. The pitot-assembly was connected to the tunnel as shown in Fig. 2.4. With different pressures in the tube tunnel, the flow was controlled by an electromagnetic valve which when switched on, a sudden opening between the pitot assembly and the tube tunnel was provided. The response of the pitot tube to the pressure change was monitored on an oscilloscope type 546 B. The response signal was recorded on a FM recorder type B&K 7005 with FM unit type ZM 0053 for later examination.

One of the major difficulties encountered in monitoring the electrical signal of the pressure transducer was the weak signal which was of the same order of magnitude of the noise level. The problem was solved by using a special operational amplifier (Fig. 2.5) constructed by using an instrumentation amplifier, type INA 101 HP. The amplifier when connected to the pressure transducer gave a gain of 104 times the transducer output signal, and thus a one-bar gage pressure signal, for instance, is amplified from 0.1 mV to 10.4 mV and the noise level was filtered down from about 20 mV to 2 mV. Fig. 2.6A shows the schematic for electrical layout.

2.3 Jet Calibration

As a result of the tube tunnel construction, the flow of the gas to the atmosphere is accompanied by some pressure losses. The jet calibration was aimed at relating the stagnation pressure of the jet (P_o) to the tube pressure (P_t). In order to determine P_o at different P_t, the pitot tube was placed immediately at the exit of the nozzle ($Z_n = 0.0$) with the horizontal tube aligned with nozzle center line (Fig. 2.7). Due to the relatively large curvature of the shock wave that forms upstream of the pitot tube, the portion of the shock wave at the centerline of the nozzle may be considered a normal shock. Hence, the flow felt by the pitot tube is a subsonic flow. The ratio of the pressure measured by the pitot tube (P_p) to the stagnation pressure of the jet upstream the shock (P_o) is given by:

$$\frac{P_o}{P_p} = \left(1+\frac{\gamma-1}{2}M_1^2\right)^{\left(\frac{\gamma}{\gamma-1}\right)} \frac{1}{\left(\frac{\gamma+1}{2}\right)M_1^2}\left[\frac{\frac{\gamma+1}{2}M_1^2}{\frac{2\gamma}{\gamma+1}M_1^2-\frac{\gamma-1}{\gamma+1}}\right]^{\left(\frac{1}{1-\gamma}\right)} \qquad (1)$$

where γ is the gas constant, and M_n is the nozzle Mach number.

At $M_n = 2.7$, and $\gamma = 2.4$, equation (1) reduces to

$$P_o = 2.12\, P_p \qquad (2)$$

Therefore, the experimental calibration relates the measured tube pressure (P_t) to the stagnation pressure of the jet as induced from the pitot pressure measurement (P_p) through equation (2).

Theoretical Value for $\frac{P_o}{P_t}$

As given by Zucrow and Hoffman [7], the ratio of the tube area (A_t) to the critical area A* in terms of tube Mach number (M_t) is given by

$$\frac{A_t}{A^*} = \frac{1}{M_t} \left[\frac{2}{\gamma+1} \left(1 + \frac{\gamma-1}{2} M_t\right)\right]^{\frac{\gamma+1}{2(\gamma-1)}} \tag{3}$$

From [8], the theoretical value of the ratio $\frac{P_o}{P_t}$ is given by

$$\left(\frac{P_o}{P_t}\right)_{\text{theoretical}} = \left[\frac{1 - \frac{\gamma-1}{2} M_t}{1 + \frac{\gamma-1}{2} M_t}\right]^{\frac{(n-1)2}{\gamma-1}} * \left[\frac{(1+ \frac{\gamma-1}{2} M_t^2)^{\frac{\gamma}{\gamma-1}}}{(1+ \frac{\gamma-1}{2} M_t)^{\frac{2}{\gamma-1}}}\right] \tag{4}$$

where n is the cycle number of the flow, and P_t is the tube pressure. Since the experiment was conducted during the first cycle, hence the value of n in Eq. (4) is set at 1. Equation (4) thus reduces to

$$\left(\frac{P_o}{P_t}\right)_{theoretical} = \frac{\left(1 + \frac{\gamma - 1}{2} M_t^2\right)^{\frac{\gamma}{\gamma-1}}}{\left(1 + \frac{\gamma-1}{2} M_t\right)^{\frac{2}{\gamma-1}}} \qquad (5)$$

The tube tunnel in our investigation has $A_t = 907.5\ mm^2$ $A^* = 176.6\ mm^2$ Therefore.

$$\frac{A_t}{A^*} = 5.14$$

with substitution in Eqn. 3,

$$M_t = 0.1114$$

and from Eqn. 5.

$$\left[\frac{P_o}{P_t}\right]_{theoretical} = 0.865.$$

Calculation of Theoretical Jet Duration

Since nitrogen was the gas used in this experiment and with a temperature $T_t = 20°C \equiv 293.15\ K$. the speed of sound is

$$a = \sqrt{\gamma RT_t}. \qquad (6)$$

So, $a = 343.2$ m/s and the length of the tube l_t is 24 m. So, the duration of the steady jet (t_j), as given by Ludwieg [6]

$$t_i = 2\frac{l}{a} = 0.9 = 0.126 \text{ sec.} \qquad (7)$$

2.4 Pitot Pressure Along the Free Jet Axis

For an underexpanded supersonic jet, pitot pressure distribution along the jet axis reveals some of its main characteristics. Some of these characteristics are local Mach number variation, Mach disc location, inviscid flow region, expansion and recompression regions.

In this experiment, the pitot tube was located along the free Jet axis at different distances, Z_n, from the jet exit (Fig. 2.7). The jet was operated on both under-expansion ratios of 2.0 and 2.2. For each case, the pressure distribution along the jet axis was recorded. Due to the large variation of pressure along Z_n in the near region ($Z_n \leq D_n$), the spacing between successive pitot locations was set at 0.1 of the exit nozzle diameter (D_n). For larger $D_n \leq Z_n \leq 4\ D_n$, the spacing between the points was set at 0.2 D_n. The electrical set up is shown in Fig. 2.6B.

2.5 Surface Flow Visualization

A series of surface flow visualization experiments were conducted in this investigation. The reason for these experiments arose from the need to:

(1) check the flow symmetry and determine the centerline of symmetry of the flow on the flat plate.

(2) determine flow boundaries of different regions.

(3) determine the location of the pressure measurements.

(4) correlate the pressure distribution on the flat plate with the surface flow visualization.

The surface flow visualization was made for the plate positions presented in Table 1. For each position, a mixture of light oil and yellow powder, with a ratio of 2 to 1 by volume was sprayed on the plate using an electric spray gun. Then, the jet was operated setting the electric timer to 0.15 sec. This was repeated while adjusting the mixture film thickness until the clearest trace on the plate was achieved. Then, the trace of the jet on the plate was photographed for later examination.

2.6 Pressure Distribution on the Plate

One of the objectives of this investigation was to measure the normal force on the flat plate as a result of jet impingement at different angles of attack. One means of obtaining the normal force is through measurement of pressure distribution over the plate.

Pressure measurements on the plate surface can also be used to provide information about locations of shock reflection and separation regions in the flow field [3].

Pressure measurements on the surface of the plate were conducted at different plate inclinations ranging between $\theta = -5^{\circ}$ and 30°. The measurement took place at selected positions on the plate. The choice of pressure measurement points was guided by flow visualization pictures. Furthermore, the experiment on the pitot response measurement was used to determine the size of the pressure connector which connects the taps on the surface to the pressure transducers (Fig. 2.8).

Three longitudinal rows of pressure taps, each of diameter 1.5 mm, were drilled through the surface. The configuration of the tap on the surface is shown in Fig. 2.9. With this type of configuration and the flexibility in moving the plate assembly in the side-wise (y) and stream-wise (x) direction, as shown in Fig. 2.10, pressure readings were obtained in regions bounded by $0.0 \le Y \le 0.4\ D_n$, $0.5\ D_n \le Y \le 1.2\ D_n$, and $-1.3\ D_n \le Y \le -1.9\ D_n$ (see Figure 2.11). Spacing between two points

could be made as small as 0.1 D_n in side-wise and stream-wise direction.

Three pressure transducers with their pressure connectors (Fig. 2.8) were used. Hence, three pressure data points could be recorded at one time. The spacing between the taps are constrained by the size of pressure transducers. The electrical layout for pressure measurement is shown in Fig. 2.5.

Before taking a full map of the pressure measurements, the centerline pressure distribution was first measured. The pattern of the surface flow visualization was used as a guide to determine the distance between successive data point on the centerline. In regions where the surface flow visualization shows narrow and sudden changes in the flow pattern, the distance between the data points was set at 0.1 D_n.

After taking the pressure measurements along the centerline, symmetry in the flow over the plate was checked by taking some pressure measurements along the positive and negative Y-axis, for the same X location.

The information provided by both centerline pressure measurement and surface flow visualization was used to determine the locations of pressure measurements over the rest of the plate. Pressure taps on line A (Fig. 2.9) were used to measure the pressure bounded in the region $0.0 \le Y \le 0.4\ D_n$, while pressure taps on line B were used to measure the pressure bounded in the region $0.5\ D_n \le y \le 1.2\ D_n$, and for line C, the region was bounded by $-1.3\ D_n \le Y \le -1.9\ D_n$.

The pressure signal was recorded on the FM tape recorder, in the DC mode, and was replayed later on the oscilloscope after rejecting all the frequencies ranging from 50 Hz to 20 KHz using the universal filter. The average of the minimum and maximum values of the pressure signal between 60 ms and 120 ms was considered as the actual pressure. The same pressure measuring technique was used for all plate positions.

2.7 Measurement of Normal Force on the Plate Using Strain-Gage Technique

2.7.1 Introduction

For underexpanded supersonic jet impingement on a flat plate, theoretical prediction of the normal force coefficient was first achieved by the Lockheed blume program through numerical integration. Lamont and Hunt [2] developed a simplified theoretical expression for prediction of normal force coefficient. They found the normal force coefficient experimentally by integrating the pressure distribution on the plate. There were deviations between their experimental values and theoretical predication of the normal force coefficient. This was referred, in their discussion, to errors in pressure readings created by the pressure transducer. Referring to their results, the deviation between their experimental and theoretical values were more than 15% in some cases.

So, to limit the errors in evaluating the normal force coefficient on the plate, a strain gage was used, in this experiment, to measure the normal force acting on the plate in a more direct way.

On the other hand, when strain gage is used, the forces created by natural frequencies of the plate assembly affect the force measurement signal. Due to the short jet duration, the oscillating force created by the natural frequency cannot be damped physically. So, a suitable solution was devised to filter the force signal electrically. As a

result, the first step in this experiment was to measure the natural frequency of the plate assembly.

2.7.2 Measurement of the Natural Frequency

As we can see in Fig. 2.12, the experimental layout is composed of mechanical and electrical parts. For the mechanical part, an upper flat plate was mounted on the plate assembly (Fig. 2.10). At the front, near the jet exit, the plate was supported by two y-bearings aligned on the same axis perpendicular to the jet axis. Under the downstream end of the plate, a force transducer with a ball bearing supported the plate. This is done to eliminate all side forces that might be exerted on the load cell, allowing only the normal force to act on it, while the other forces are taken by the y-bearings. A tension spring, at the end of the flat plate, was set at a prenormal force on the force transducer in order to keep the plate in contact with the transducer during the vibration of the plate assembly.

At the beginning of the experiment, the conditional amplifier was set to frequency response of 1 Hz to 30 x 10^3 Hz and directly connected to the oscilloscope. Then, a plastic hammer was used to give an impact on the plate and the force signal was observed on the oscilloscope .

After several trials, it was found that more than one natural frequency was present, and the frequency of 93 Hz was clearly observed. Subsequently, the filter was used to reject only frequencies lower than 70 Hz. Then, an impulse was applied to the plate by the hammer. The force signal showed an oscillation of 93 Hz with a mean

value of zero. This part was repeated several times and the same result was obtained in each trial.

In the next step, the filter was set to reject only frequencies higher than 80 Hz. Then, the experiment was repeated, as before, several times. The result was a force oscillating at a frequency of 40 Hz with mean value of zero.

In these experiments, the time range of the oscilloscope was set to 20 ms which gave the full screen of 200 ms time range. This range is able to contain the whole jet duration (140 ms). With this time setting of the oscilloscope , only the two frequencies of 93 Hz and 40 Hz were observed during the experiment.

2.7.3 Normal Force Measurement

The mechanical layout was constructed as shown in Fig. 2.13. The upper plate, in which the normal force was to be measured, supported by two y-bearings, at two locations as shown in Fig. 2.14. The strain gage assembly (Fig. 2.15) was fixed in the place of the force cell used in the natural frequency measurement.

Before taking the force measurement, the strain gage had been calibrated. To do this, the electrical layout of the experiment was constructed as shown in Fig. 2.16. Then, standard weights ranging from 9.8 N to 400 N were applied at the rear end of the plate, at the location of the pre-load spring. The force signal was recorded for each weight. Calibration of the strain gage was made with the plate situated horizontally at $\theta = 0°$.

To measure the normal force acting on the plate by the jet, the experimental set up was used with a spring acting at a pre-load value of 100 N on the strain gage assembly. This prevented the plate from rebouncing during the experiment.

The y-bearings were fixed at 80 mm in front of the plate front edge (Fig. 2.14) and the plate assembly was adjusted to the required position. After that, the pressure regulator of the tube tunnel was set to fill the tube tunnel to the required pressure. The jet was operated several times while altering the electric filter to reject frequencies from the force signal caused by natural frequencies of the mechanical set up. In monitoring the force signal, it was found that setting the electric filter to reject all frequencies higher than 19 Hz gave a steady force signal for the last 80 ms of the jet duration. With filtering out all frequencies higher than 19 Hz, the jet was operated several times for the same condition and the values of the force F_1 were recorded. When the y-bearings were positioned at 80 mm downstream the plate front edge, the jet was operated several times and the values of the force F_2 were recorded. Using the same procedure as outlined before, the values F_1 and F_2 were obtained for all the required positions of the plate and conditions of the jet.

Design calculation of the strain gage cantilever and force measurement theory are shown in Appendix A and B respectively.

3. DISCUSSION

3.1 Introduction

In this chapter, results of the experiments are discussed according to their sequential order in Chapter 2. This was done due to the fact that results obtained in some of the first experiments were used to carry out later ones.

3.2 Pitot Response

The objective of measuring the time response of the three pitot-tube configurations at different tube tunnel pressures was to determine the time at which the tube reads the pressure signal correctly. Fig. 3.1 shows the pressure response of the first configuration of pitot tube (Fig. 3.2) to a 40-bar tunnel pressure. This case is taken as an example for the other pitot configurations. The signal, as can be seen, is divided into three segments, starting region, rising region, and settling region. The starting region is believed to be influenced by flow acceleration and valve opening action. The rising region represents the rise time from the starting level to the tube tunnel pressure. The settling region shows a signal oscillation that damps out after four cycles with a frequency of 250 Hz. The first cycle can be observed clearly since it has a maximum amplitude of 7% of the total signal. The second cycle has a maximum amplitude of 3% of the total signal and the third cycle has a maximum amplitude of less than 2%. So, the length of the settling region can be

defined as the time starting from the end of the rise time to the end of the second cycle. Taking the reading of the signal after the settling time will give an error of less than 2%. It was found that for all pitot configurations and various tube tunnel pressures, features of the response signals were similar to those of Fig. 3.1. The duration of the settling time was always the same for all cases tested. Figs. 3.2, 3.3 and 3.4 summarize the total time response of all the pitot-tube configurations at different tube-tunnel pressures. The total time response is the sum of time-durations of starting, rising, and settling regions. It was generally observed that the change in response time for different pitot-tube configurations is mainly a function of pitot-tube diameter for each tube-pressure setting. The time response increases as the pitot-diameter decreases. For example, rise time for a pressure of 60 bar was increased by 8% when using the third pitot in place of the second, while the decrease in the area is 74%.

3.3 Stagnation Pressure Measurement

Theoretical effective jet duration of the flow is ≅ 0.12 sec. This figure is in good agreement with the time found in the experiment which is 0.126 sec. as seen in Figure 3.5. During this time, the pitot pressure falls linearly by 2% to 4% over the jet duration. Hefer and Koppenwalner [12] obtained similar values for their experiments at M_e = 3.85, and M_t = 0.093. The fall in pressure during the flow is due to the development of the boundary layer inside the tube which, for a fixed frame, grows with time [6] and causes more turbulence and thus more pressure losses.

In Fig. 3.6, it is shown that the stagnation pressure at different tube pressures is always less than its respective tube pressure with a maximum deviation of 5%. This is believed to be caused by friction in the tube. Moreover, nonlinearity of the pressure transducer and the high turbulence of the jet are expected to induce errors in reading the stagnation pressure. Fig. 3.7 illustrates the variation of the underexpansion ratio of the jet with tube pressure.

3.4 Centerline Pitot Pressure Measurement

Figure 3.8A shows the structure of an under-expanded supersonic jet when flowing into still air [13]. Fig. 3.8B describes the variation of the pitot-pressure along the centerline of the free jet of under-expansions 2 and 2.2. It characterizes the shock system that exists up to 4 nozzle diameters downstream nozzle exit. Four regions are identified. The first region extends from the nozzle exit upto $Zn = 0.7\ D_n$. As we can see in Fig. 3.8B, the pitot pressure for both under expansions of 2 and 2.2, drops sharply as we move downstream the nozzle exit along the jet axis. This drop in the pitot-pressure in this region shows an increase in the local Mach number due to the nature of the radial flow at the nozzle exit which causes greater stagnation pressure loss through the shock in front of the pitot as the Mach number increases (2). In the second region, downstream, pitot pressure increases with Z_n. This is due to the decreasing Mach number which causes a weaker shock in front of the pitot and led to the decrease of total pressure losses. This recompression is taking place for both underexpansions at $Z_n \cong 0.8\ D_n$. The recompression region is due to the shape of the nozzle shock (2) which is a weak shock caused by the overexpansion in the nozzle downstream of the throat. The third region, just behind the Mach disk shows a constant pitot pressure distribution. This is due to the fact that the flow is subsonic and consequently inviscid. For both underexpansion ratios, this region starts at $Z_n = 2.6\ D_n$ but ends at $Z_n = 3\ D_n$ for PR = 2.2 and for PR = 2.0 it ends later at $Z_n = 3.6\ D_n$.

From Fig. 3.8B, it can be deduced that the Mach disc for both underexpansion ratios is located at $Z_n = 2.6\ D_n$. On the other hand, the size of the first cell in the shock system of the jet is very sensitive to the pressure ratio, where for PR = 2.0 it was 3.1 D_n and for PR = 2.2, the cell size was 3.6 D_n. It was also found that large pressure fluctuation is taking place at the end of the cell. This is probably due to the fact that at the end of the cell, the supersonic flow region has a sharp end and any small fluctuation of this region will cause the pitot tube to be dislocated from this region to the supersonic region which has a large pitot pressure difference.

The location of the recompression region was indicated for both underexpansions and matches very well with the results obtained by Lamont and Hunt [2] where they found the location of the recompression region at $Z_n \cong 0.85\ D_n$ which was in good agreement with the result predicted by the Lockheed bloom program.

3.5 Surface Flow Visualization

Fig. 3.8C describes the interaction process of the jet with the plate at $\theta = 30°$ [2]. Figs. (3.9A to 3.18A) show surface flow visualization pictures for the supersonic jet impingement on the flat plate at inclinations ranging from $\theta = +30°$ to $\theta = -5°$. The surface flow features from the visualization pictures are compared with repective surface pressure measurements along the plate centerline given in Figs. 3.9B to 3.18B. The arrangement of the sequence of figures was chosen to provide a correlation between the pressure measurements and the surface flow visualization pictures.

Comparing the surface flow picture, Fig. 3.9A, with the pressure along the centerline of the plate, Fig. 3.9B, one observes that the two maximum pressure regions indicated in Fig. 3.9B compare with the two clear regions on the plate (Fig. 3.9A). The location of the first spot is upstream of the point of impingement with the plate, while the second clear spot occurs downstream of the point of impingement. Before entering the first region, the flow passes through the first shock reflection, designated by Lamont and Hunt [2] as the upper tail shock reflection, and still maintains most of its kinetic energy. The combination of high pressure and velocity cause the blow out of the oil mixture. The second maximum pressure region, further downstream, is caused by a second shock reflection designated in [2] as intermediate shock reflection. This region appears in Fig. 3.9A as a small triangular clear spot followed by heavy mixture accumulation. This heavy mixture

accumulation is probably caused by both deceleration of the flow and the demolished part of the oil mixture upstream. The small size of the clear spot is believed to be due to both low local velocity, since the flow has passed through two shock reflections, and the accumulation of the oil mixture transferred from upstream. The triangular shape of the oil mixture accumulation here has a narrow end and corresponds to a compression region for a supersonic flow.

For the PR = 2.2 and Z_n/D_n = 7.2 as can be seen from Figures 3.10A, 3.11A and 3.12A, the flow patterns have a common shape for the angles 30° through 15° and very similar to the pattern of PR = 2.0 with Z_n/D_n = 2.1 (Fig. 3.9A). This means that there are two pressure peaks on the plate surface. The first peak is indicated by the clear spot and the second pressure peak is just before the triangular shape of oil mixture accumulation. Also, it is obvious that more regions on the plate are influenced longitudinally as the plate angle decreases. This is due to the fact that at lower angles, the plate surface is closer to the supersonic region of the jet (upstream) and, hence, larger area is exposed to the shock system.

For θ = 5°, as shown in Figure 3.14A, the flow is quite different. At this condition, the surface at the front edge is only 0.04 D_n away from the nozzle and the clear parabolic spot shows that the higher pressure region occurs at $X_p \cong D_n$. Following this at $X_p \cong 3.5\ D_n$, the flow pattern shows a contraction region, a second high pressure region. This region coincides with the location at the end of the first cell in the free jet where the flow has a minimum velocity and high static pressure.

Further downstream, the flow goes through a succession of expansion and contraction which is indicated by the elliptical patterns, which decrease in width as the flow progresses. This succession perhaps represents the effect of expansion and compression taking place inside the shock cells of the jet.

When the plate surface is parallel to the jet axis, and at $h = 0.04\ D_n$, it is obvious from Fig. 3.15A, that the flow pattern is very similar to the case when $\theta = 5°$. On the other hand, the flow region is much narrower from the sides. As the distance h is increased to $0.24\ D_n$, (Fig. 3.16A), the same pattern shrinks from the sides and when the distance h is increased to $0.5\ D_n$, (Fig. 3.17A), the effect of the pressure fluctuation in the shock cells has already disappeared.

In Fig. 3.18A, where $\theta = -5°$, the flow pattern near the jet exit at $X_p \leq 4\ D_n$, shows a similar flow behavior to that at $\theta = 5°$, but with a narrower sides, especially at the end of the region which indicates lower pressure $\theta = 5°$ at the same spot. Downstream, the flow pattern shows a completely different behavior where the flow is directed towards the centerline with no sign of shock cell effect on the plate surface. This means that the flow over the surface is subsonic and it is a suction region.

3.6 Surface Pressure

3.6.1 Centerline Pressure

At the start of this discussion, the centerline pressure for the case where the conditions are set as $\theta = 30°$, PR = 2, and $Z_n/D_n = 2.1$, is compared with a similar case done by Lamont and Hunt [2], where they set $\theta = 30°$, PR = 2, and $Z_n/D_n = 2.0$. Looking at the centerline pressure presented in Fig. 3.19B, one can see the similarity between the results. There are two pressure peaks. The first one is located at X = -1.2 D_n for both experiments, and it is due to the upper tail shock reflection. The second pressure peak caused by the intermediate tail shock reflection for this experiment is at X = 0.9 D_n, while for Lamont and Hunt [2] experiment, it is located at X = 0.5 D_n. Furthermore, the minimum pressure between the two maximum pressure regions, occurs just in front of the second pressure peak for both experiments. Also, the trends in the pressure gradient throughout the center line of the flow are similar in both experiments. The deviation in pressure values and location of the second pressure peak between the two experiments is mainly due to the difference in Mach number of the jet nozzle used.

For PR = 2.2 and $Z_n/D_n = 7.2$ the centerline pressure distribution for the plate surface was measured for the angles ranging from 5° to 30°. Figures (3.10B to 3.14B) present the pressure distribution in detail. Also, Figure 3.19A shows the centerline pressure distribution at different angles of attack. It can be seen that for all

angles, there are two pressure peaks, one in the positive and the other in the negative X/D_n axis, except for $\theta = 5^\circ$ where both peaks are in the negative X/D_n.

The centerline pressure distribution was measured for two cases when the plate was parallel to the free jet axis ($\theta = 0^\circ$) and positioned at two vertical distances from the jet nozzle lip of $h = 0.04\ D_n$ and $h = 0.24\ D_n$, are shown in Fig. 3.15B and Fig. 3.16B respectively. Only the first two pressure peaks are shown for this case since they were much larger than the other pressure peaks down stream.

3.6.2 Maximum Pressure Regions

For angles 30° to 10° of the plate, the two maximum pressure regions as shown in the 3-dimensional Figures (3.9C - 3.13C) are due to the shock reflections. These pressure regions extend side ways in the y direction to $\pm\ 1.2\ D_n$ for $\theta = 30^\circ$ and contract to $\pm\ 0.8\ D_n$ for $\theta = 10^\circ$. The location of maximum pressure regions and their sizes agree well with the results obtained by the surface flow visualization.

From the 3-dimensional figures of the pressure distribution, it is clear that the maximum value of pressure is always on the centerline of the flow. Moreover, at $\theta = 30^\circ$, the upstream peak has a maximum pressure of $0.075\ P_o$ while downstream peak has a maximum pressure of $0.11\ P_o$. At $\theta = 20^\circ$, the peak pressure in both maximum pressure regions has almost the same value $\cong 0.06\ P_o$. While as the angle of the plate is decreased, the second maximum pressure region has a lower

peak than the first. Also, the peak pressure decreases when 0 is decreased, except at 0 = 10° where the first maximum pressure region peaked at a value of ≅ 0.054 P_o while at 0 = 15° the peak pressure was only ≅ 0.045 P_o. The behavior at 0 = 10° could be due to the plate surface being closer to the second shock cell structure of the jet which may have created a stronger shock reflection (higher angle of reflection) on the plate.

At 0 = 5°, as shown in Fig. 3.14B and 3.14C, the first two maximum pressure regions peaked at very close values (0.04 P_o for the first and 0.035 P_o for the second). The first maximum region, upstream, is a result of the shock reflections near the nozzle exit (upper tail shock reflection) where the pressure peaks at the location X = -6.4 D_n (X_p ≅ 0.8 D_n) and extends side ways to y ± 0.9 D_n forming a bow that is very clear in the surface flow visualization (Fig. 3.14A). The second maximum pressure region peaks at the location X = -2.4 D_n or (X_p ≅ 4.8) just downstream the first shock cell of the free jet, which means that it is probably caused by an intermediate tail shock reflection. This region extends to y ≅ ± 0.8 D_n sideways.

Comparing Fig. 3.9C at 0 = 30°, PR = 2 and Z_n/D_n = 2.1 with the isobar graph for the experiment done by Lamont and Hunt (2), it is found that the first maximum pressure region created by the upper tail shock reflection extends 0.8 D_n sideways, in the Y-direction, and occupies a similar location. On the other hand, the second maximum pressure region in Fig. 3.9C is shifted downstream by 0.4 D_n compared

to the experiment that is obtained by Lamont and Hunt (2). However, the extension of this region in the same in Y-direction is the same for both cases. In general, the results show a similar flow behavior.

3.6.3 Suction Region

Suction is defined here as the pressure less than atmospheric which means that it will have a negative value. Using this definition, a suction region, between the two maximum pressure regions, exists only for angles $\theta \leq 15°$. It is clear from the figure (3.19A) that the minimum pressure in the suction region decreases as the plate angle decreases, starting with a value of -0.009 P_o for $\theta = 15°$ down to -0.015 P_o for $\theta = 5°$. Moreover, the suction region increases in size as the angle θ decreases, which means greater negative effect on the normal force acting on the plate surface. The suction region starts acting on a small area for $\theta = 15°$ bounded by $-0.2\ D_n \leq X \leq 0.6\ D_n$ and $-0.7\ D_n \leq Y \leq 0.7\ D_n$ and grows to an area bounded by $-4.4\ D_n \leq X \leq -3\ D_n$ and $-0.4\ D_n \leq Y \leq 0.4\ D_n$. This suction region is due to the expansion following the shock reflection.

3.6.4 Parallel and Negative Plate Angle Pressure Distribution

From surface flow visualization it was deduced that when the plate surface was set parallel to the jet axis, ($\theta = 0$), the jet has pressure influence only at $h = 0.04\ D_n$ and $0.24\ D_n$ with well defined regions on the plate surface.

The centerline pressure distribution and 3-dimensional graph of

the pressure distribution on the plate surface at ($\theta = 0°$), and $h = 0.04\ D_n$ are presented in Fig. 3.15B and 3.15C . As shown in these figures, the pressure peaks at three locations. The first is located at $X_p = 0.4\ D_n$ (10 mm from the leading edge of the plate), and at this location, the maximum pressure was measured to be $0.024\ P_o$. This pressure region as shown in the surface flow visualization starts near the leading edge of the plate ($X_p \cong 0$), and ends at $X_p = 1.6\ D_n$. From the 3-dimensional figure (Fig. 3.15C), this region extends sideways for at least $0.5\ D_n$ in the $\pm$ Y-direction. Since the plate distance from the nozzle lip is only $0.04\ D_n$, the surface of the plate intercepts the nozzle shock at its maximum angle relative to the plate. This could explain the maximum pressure in this region. This statement seem to be supported by the curved backward shape of the maximum pressure region as seen in Fig. 3.15C. The second maximum pressure region is centered at $X_p = 6.0\ D_n$, with a peak value of $0.04\ P_o$. The side-ways extension of this region is at $Y = \pm 0.7\ D_n$. The third high pressure zone is centered at about $X_p = \cong 12.0\ D_n$. On the other hand, there are two suction regions on the plate.

In the case of $\theta = 0°$ (Fig. 3.16B) and $h = 0.24\ D_n$, the maximum pressure is much less than the previous case ($h = 0.04\ D_n$) and the first maximum pressure starts at $X_p = 0.6\ D_n$ and peaks at $X_p = 1.2\ D_n$ at a value of $0.08\ P_o$. This is only half the value of the peak pressure in the second maximum pressure region which is located at $X_p = 5.2\ D_n$. From the 3-dimensional graph in Fig. 3.16C, it can be

seen that the pressure regions are relatively narrow (extending only up to $\pm$ 0.4 D_n in the Y-direction), which means that the jet shock cells have a much smaller pressure effect on the plate surface than for $h = 0.04\ D_n$.

For $\theta = -5°$ with $h = 0.04$ (Fig. 3.18B), the first maximum pressure region starts from the plate leading edge, as shown in the surface flow visualization, while the pressure reading starts at $X_p = 0.4\ D_n$ with a value of 0.01 P_o. The effect of recompression region in the first shock cell of the jet can be seen at $X_p \cong 0.8\ D_n$. So, from the pressure distribution and magnitude, it looks like there is no sign of reflected shock in the first maximum pressure region. Further downstream, the pressure continues to drop in the suction region till it reaches a minimum of 0.014 P_o at $X_p = 2.4\ D_n$ (near the location of the Mach disc at the end of the first shock cell). After that, the pressure distribution flattens out at this minimum value up to $X_p = 3.2\ D_n$ (near the end of the first shock cell). Then, it increases sharply to reach a second peak, at the second maximum pressure region, (at $X_p \cong 4.2\ D_n$) with a value of 0.025 P_o. This pressure distribution behaves in the same way as the pitot pressure in the centerline of the free jet, which means that even though the flow above the plate is 3-dimensional, still the surface pressure is mainly effected by the flow in the shock cell. Finally, the 3-dimension graph (Fig. 3.18C) of the pressure distribution shows that the pressure regions are bounded by $-0.5\ D_n \le Y \le +0.5\ D_n$.

3.7 Normal Force

3.7.1 Normal Force by Pressure Measurements

The normal force on the plate surface was first computed by integrating the measured surface pressure. Each pressure measurement location presents an area according to the space between each other. The experimental force coefficient as given by Lamont and Hunt [2] is:

$$C_{FP} = \frac{F_p}{P_o A_n} \tag{24}$$

and the theoretical force coefficient as given by (2) is:

$$C_{FI} = \text{Sin } 0 \frac{P_c}{P_o} \left(1 - \frac{1}{PR} + \gamma M_n^2\right) \tag{25}$$

The results are given in Table (2), and plotted in Fig. 3.20.

As we can see, the force coefficient computed by pressure integration was only done for angles 30° to 5°. This is due to the fact that the error induced by pressure reading (0.025 bar) when integrated over the surface area, will produce an error in their force $\cong$ 100 N which is already > 100% of the total computed force for 0 = 5°. On the other hand, for other angles the deviation between C_{FP} and C_{FI} ranged between 27% and -8%. Another possible source of error, in computing (C_{FP}), is the large spacing between the pressure taps (0.4 D_n) for some regions.

3.7.2 Normal Force by Strain Gage Technique

The forces measured by strain gage technique was decreasing linearly by only 3 to 5% over the duration of the jet. The average normal force (F_p) force coefficient (C_{FS}) and center of pressure location (X_F) were calculated for all configurations and the results are presented in Table 3.

Repetition of the force measurement did not show any deviation between trials. The maximum error in the force measurement using the strain gage is < 5%.

The center of pressure location was always downstream the point of intersection between the jet centerline and the plate surface (positive X) for all positive θ. As we can see in Table 3, for PR = 2.2 and Z_p/D_n = 7.2, X_F increases from 2.14 D_n at θ = 30° to a maximum value of 4.0 D_n at θ = 10°, which is a small variation compared to the extension of the pressure field. This increase in X_F is due to the fact that the location of the second pressure peak, at θ = 10°, has shifted downstream by 2.5 D_n compared to the case of θ = 30°, as shown in Fig. 3.19. On the other hand, at θ = 5°, the center of pressure is shifted forward to X_F = 2.9 D_n which has resulted from the location of the first shock reflection (at X_F = −7.0 D_n close to the leading edge of the plate).

3.7.3 Comparison with the Theory

The results of computing C_{FT}, C_{FP} and C_{FS} are presented in Fig.

3.20. The maximum deviation of C_{FP} from theoretical prediction, C_{FT}, is 0.45.

On the other hand, the actual force coefficient obtained by Strain-gage technique (C_{FS}) was always higher than the theoretical value by 25% to 33%, at $5° \leq \theta \leq 20°$, while the difference is reduced to 8% for $\theta = 30°$. For the comparative case with Lamont, the actual force coefficient was 14% higher than the theoretical value which compares very well with the about 13% deviation figure obtained by Lamont and Hunt [2].

The increase in the normal force coefficient is probably due to the fact that the flow separation is taking place on the plate surface at locations of shock reflections which will force part of the flow to be deflected away from the plate surface. This will result in a deflection in the total flow which means that the flow will leave the plate surface with an angle and not as the theory assumes that the flow leaves parallel to the plate.

When the plate surface was situated at $\theta = 0$, only at $h = 0.04\ D_n$ (1 mm), a force was recognized by the strain gage and the force coefficient was calculated to be 0.0283 while the center of pressure was at $X_p \cong 19\ D_n$. This means that the jet momentum was deflected by an angle of $\cong 3°$, away from the plate surface, which is a result of the radial flow near the nozzle exit of the jet.

In the case where $\theta = -5°$, the net result of the pressure force was negative (suction) and the force coefficient was $C_{FS} = -0.0209$. This

could be due to the entrainment of fluid caused by viscous effects in the mixing region of the jet.

4. CONCLUSION

1. The tube tunnel used in this investigation was able to sustain a steady flow for at least 120 ms at various tunnel pressures (30-80 bar). Maximum drop in the stagnation pressure of the tunnel during this period was 4%. The three pitot-tube configurations investigated in this study gave time response values much smaller than the duration of the jet. The pitot-tube with the smallest diameter was chosen to carry out the pressure measurements. Smaller pitot-tube diameters were not attempted due to pracatical limitations. The error in measuring the pressure was less than 2%.

2. Pitot pressure measurement along the centerline of the free jet can reveal different regions inside the first shock cell. The location of the recompression region was the same for the pressure ratios (PR) tried in this investigation. On the other hand, the size of the first shock cell in the free jet increases with pressure ratio, as was obtained by Lamont and Hunt (2).

3. The surface pressure measurements and the surface flow visualization pictures are used to enhance the understanding of jet impingement flow phenomena on the plate. A high pressure that is due to shock reflection on the surface is recognized by a clear area in the surface flow visualization, which has a bow shape for the first shock reflection upstream. The second maximum pressure region caused by the intermediate shock

reflection is recognized by a small clear spot followed by oil mixture accumulation that shows an inward flow towards the centerline. This indicates that there is a compression region with low velocity and a possible separation region. Moreover, suction in the subsonic region was indicated in the surface flow visualization by continuous inward flow towards the centerline till the end of the plate, for $\theta = -5°$. As a result, the surface flow visualization is a simple and economical means of identifying different pressure regions on the plate surface. Also, it can be utilized as a guideline in determining the pressure reading locations and resolutions.

4. The distribution of the surface pressure for inclined positions of the plate ($\theta > 0$) shows that there are always two high pressure regions which have the dominant contribution to the normal force. On the other hand, suction regions were only observed at angle $\leq 15°$. In general, suction regions increase in area when θ is decreased.

5. The normal force on the plate, as measured by the strain-gage technique, was found to be always greater than that predicted by the theory with the deviation reaching 27% in the range of $5° \leq \theta \leq 20°$. The deviation could be due to the assumption implied in the theoretical model which indicates that the jet is deflected, after impingement with the plate, in a parallel direction to the plate surface. The deflection with an angle from the surface comes as a result of boundary layer separation, after the shock

reflection [3], which, in turn, causes part of the flow to be deflected away from the surface. There seems to be a need for incorporating a correction factor in the theoretical expression for predicting the normal force. Therefore, further investigation on the normal force resulting from supersonic jet impingement, is needed for different plate inclinations at different nozzle Mach number, pressure ratio, and nozzle plate spacing (Z_n/D_n).

At $\theta = 0$, the normal force coefficient C_{f_n} was small (0.028), for $h = 0.04\ D_n$, and there was no sign of normal force as the distance was increased to $h = 0.24\ D_n$. This force was due mainly to the radial flow of the jet at the nozzle exit which caused the first shock reflection on the plate to appear as a high pressure region. Finally, the effect of jet mixing layer was clear at $\theta = 5°$ and caused a small negative normal force (suction) on the plate surface ($C_{f_n} = -0.0209$).

REFERENCES

1. Henderson, L.F., Z. Angew, Math. Phys. 17, 553, 1966.

2. Lamont, P.J. and Hunt, B.L., The Impingement of Underexpanded Axisymmetric Jet on Perpendicular and Inclined Flat Plates. J. Fluid Mech. 100, 471, 1980.

3. Coleman Dup D. and Richard, S.S., "A Study of Free Jet Impingement. Part I. Mean Properties of Free and Impinging Jets". J. Fluid Mech. 45, 281, 1971.

4. Lloyd, H. Back and Virendra Sarohia, Pressure Pulsation on a Flat Plate Normal to an Underexpanded Supersonic Jet. A.I.A.A.J., 16, 634, 1978.

5. Koppenwallner, G., Rammenzweig, D. and Stahl, W. "Einige Untersuchungen Zur SichtbarMachung eines Uberschallstrahls", IB 222-85, A34. DFVLR, Gottingen, Germany, 1985.

6. Ludwieg, H. Tube Wind Tunnel. A Special Type of Blowdown Tunnel. AGARD Wind Tunnel Panel Hypersonic Meeting Scheveningen, Holland, 1957.

7. Maurice J. Zucrow and Joe D. Hoffman, "Gas Dynamics", John Wiley & Sons, New York, Vol.I, 1976.

8. Theo Hottner, "Unterschungen an einem Modell-Rohrwindkanal

bei Machzahlen von Ma = 3 bis 6", Z.F.W. Heft. 7, 1965.

9. Joseph E. Shigley and Larry D. Mitchell. "Mechanical Engineering Design", McGraw-Hill, 4th edition, 1983.

10. Bearing Maintenance and Replacement Guide, SKF, 1986.

11. Hibbeler, R.C., "Engineering Mechanics (Dynamics)", Fourth Edition, 1986.

12. Hefer, G., Koppenwallner G., "Kurzzeitverschusstand Zur Triebstrahlsimulation bei hohen Druckverhaltnessen", IB 252-76 H12, DFVLR, 1976.

13. Sanford M. Dash and David E. Wolf, "Interactive Phenomena in Supersonic Jet-Mixing Problems", AIAA Journal, Vol. 22, No.7, July, 1984.

14. Christopher Chant, "Encyclopaedia of Modern Aircraft Armament," Patrick Stephens, 1988.

APPENDIX - A

Design Calculation of the Strain Gage Cantilever

The first part of the calculation deals with the design of the strain gage cantilever which has four aspects:

1. Force and stress analysis.
2. Maximum deflection.
3. Measuring system natural frequencies.
4. Effect of pre-load spring in reading the force.

The cantilever shown in Fig. 2.14 was made out of cold drawn steel (AISI 1018) which has a yield strength of σ_y = 30 Mpa, maximum allowable strain of ε = 0.15 and modulus of elasticity E = 2.07 Gpa [9].

l = 60 mm (length of the cantilever)

w = 19 mm (width of the cross section)

s = 16 mm (height of the cross section).

On the basis of the pressure measurements over the plate surface, the maximum expected average force on the cantilever bearing, including the pre-load of the spring and the weight of the plate is F_{max} = 500 N.

For checking the strength of the cantilever, the maximum tensile stress (σ_t) as given in [9] is :

$$\sigma_t = \frac{6 F_{max} L}{WS^2} = 37.0 \text{ Mpa} \qquad (8)$$

and assuming uniform shear stress on the cross-section, the shear stress, τ_s, is given by Shigly and Mitchell [9]

$$\tau_s = \frac{F_{max}}{WS} = 1.6 \text{ Mpa} \qquad (9)$$

From the above calculations, it is clear that the stresses are very small compared with the strength of the material used for the cantilever. Thus, the cantilever can be used safely for this experiment.

The bearing used in the cantilever assembly has a designation No. 6200-2Z which has an allowable static load of 2.240 N [10]. This figure is much higher than the expected force (F_{max} = 500 N) and shows that it is safe to use.

The maximum deflection of the cantilever (d_{max}) during the jet operation is given in [9] as:

$$d_{max} = \frac{4 F_{max} L^3}{E W S^3} \qquad (10)$$

Substituting for the values in the equation yields

d_{max} = 0.0268 mm.

The maximum angular deflection of the flat plate due to the d_{max} may be identified by ($\Delta\,0_{max}$), and this can be determined by the simple form:

$$\Delta\,0_{max} = \tan^{-1}\frac{d_{max}}{L} \qquad (11)$$

Substituting in this formula, we find that $\Delta\,0_{max}$ = 0.0028° which means that it will have no effect on the experiment since this error is negligible compared to the angle settings of this experiment.

Since the cantilever supporting the plate is elastic with no damping effect, the plate will oscillate when suddenly impinged by the jet. The frequency of this oscillation (f) is determined by the simple form [11]:

$$f = \frac{1}{2\pi}\sqrt{\frac{K_t}{I_o}} \qquad (12)$$

where:

I_o = is the moment of inertia of the plate about its rotating axis.

K_t = is the torsional stiffness of the cantilever about the rotating

axis of the plate.

Assuming that:

c = Thickness of the plate.

w_p = The plate width.

b = The plate length.

c = The distance between the axis of rotation and the plate center of gravity.

m = Mass of the plate.

Since the plate is made of aluminum which has a density of 2711 kg/m^3 [9], I_o can be expressed in the form (13):

$$I_o = \frac{1}{12} m (b^2 + 12 c^2) \qquad (13)$$

Substituting for the values in the equation,

$$I_o = (9.760 c^2 + 0.2928) \text{ kg. m}^2.$$

Also, from the geometry of the mechanical set up shown in Fig. 2.13 it can be deduced that

$$K_t = \frac{F_{max} (c + 0.17)^2}{d_{max}} \qquad (14)$$

Substituting:

$$K_t = 1.866 \times 10^7 (c + 0.17)^2 \text{ N m /rad.}$$

So, the final expression for the frequency f is

$$f = \frac{220\,(c+0.17)}{\sqrt{c^2 + 0.03}} \quad \text{Hz}$$

When the plate assembly was set to measure F_1, the distance between the axis of rotation and the center of mass for the plate was

$$c = 0.38 \text{ m.}$$

Subsequently, the frequency of the oscillating plate was:

$$f_1 = 289 \text{ Hz}$$

On the other hand, when measuring F_2,

$$c = 0.22 \text{ m}$$

and the oscillation frequency of the plate was

$$f_2 = 306 \text{ Hz.}$$

These frequencies are much higher than the natural frequencies of the plate structure. Hence, they would not contribute to the signal whenever the electric filter rejected the effect of the natural frequencies of the plate assembly.

The following calculation was made to see the effect of the pre-load spring on the normal force measurement.

The summation of moments around the plate axis of rotation M_o was:

$$\Sigma M_o = 0. \qquad (15)$$

which led to

$$F_p \times L_p = \Delta\theta\,(k_t - k_s). \qquad (16)$$

where k_s is the torsional stiffness of the pre-load spring, which has a linear stiffness of 3000 N/m. So,

$$K_s = 3000\,(c + 0.3)^2 \text{ (Nm/rad.)}$$

but, $K_t = 1.866\times10^7\,(c+0.17)^2$ (Nm/rad.)

We can see that the value of $K_s << K_t$. So, the effect of the pre-load spring can be neglected when calculating the normal force and the expression of the normal force can be put in the following form:

$$F_p = \frac{\Delta\theta}{L_p} K_t \qquad (17)$$

APPENDIX - B

Force Measurement Theory

The measuring system was designed in such a way that the plate axis of rotation was always on the plane of the plate surface. Also, the other end of the plate was supported by the cantilever by a ball bearing with its axis parallel to the rotation axis of the plate. This was done in order to have all the shear forces on the plate surface be taken by the y-bearing and leaving the cantilever to take the moment created by the normal force about the rotational axis of the plate.

When the distance between the cantilever bearing and the axis of rotation is L_1, the reaction of the cantilever F_1 and the expression of the normal force on the plate F_p will be:

$$\Sigma M_0 = 0$$

$$\text{Hence,} \quad F_p = \frac{F_1 L_1}{L_p} \tag{18}$$

Also, when the distance between the cantilever bearing and the axis of rotation is L_2, the reactions of the cantilever is F_2, and the normal force on the plate F_p, is:

$$F_p = \frac{F_2 L_2}{L_p + L_1 - L_2} \tag{19}$$

From the above equations,

$$\frac{F_1 L_1}{L_p} = \frac{F_2 L_2}{L_p + L_1 - L_2} \tag{20}$$

So,

$$L_p = \frac{F_1 L_1 (L_1 - L_2)}{F_1 L_1 - F_2 L_2} \tag{21}$$

Now substituting Eq. 21 into Eq. 19, we get the expression of F_p as

$$F_p = \frac{F_1 L_1 - F_2 L_2}{L_1 - L_2} \tag{22}$$

In this experiment,

$L_1 = 0.55$ m and

$L_2 = 0.39$ m.

θ (Degree)	PR	Z_n/D_n	h/D_n
0	2.2	——	0.04
0	2.2	——	0.24
0	2.2	——	0.5
5	2.2	7.2	——
10	2.2	7.2	——
15	2.2	7.2	——
20	2.2	7.2	——
30	2.0	2.1	——
30	2.2	7.2	——
−5	2.2	——	0.04

Table 1 : Surface flow visualization.

θ (Degree)	PR	Z_n/D_n	C_{FP}	C_F (Theo.)
30	2	2.1	0.264	0.257
30	2.2	7.2	0.303	0.255
20	2.2	7.2	0.179	0.174
15	2.2	7.2	0.122	0.132
10	2.2	7.2	0.112	0.088
5	2.2	7.2	0.092	0.044

Table 2 : Normal force coefficient by pressure measurement integration .

θ (Deg.)	PR	Z_n/D_n or (h)	X_F/D_n	C_{FS}	C_F (Theo.)	ΔC_F
30	2	2.1	1.94	0.294	0.257	14 %
30	2.2	7.2	2.14	0.275	0.255	8 %
20	2.2	7.2	2.10	0.226	0.174	30 %
15	2.2	7.2	2.87	0.165	0.132	25 %
10	2.2	7.2	4.00	0.118	0.088	33 %
5	2.2	7.2	2.90	0.058	0.044	31 %
0	2.2	0.04	—	0.028	—	—
0	2.2	0.24	—	0.000	—	—
-5	2.2	0.04	—	-0.021	—	—

Table 3 : Normal force coefficient by strain gage .

Figure 1.1 : Launch of an AIM-20 AMRAAM
Air-To-Air Missile of an F-16 A [14].

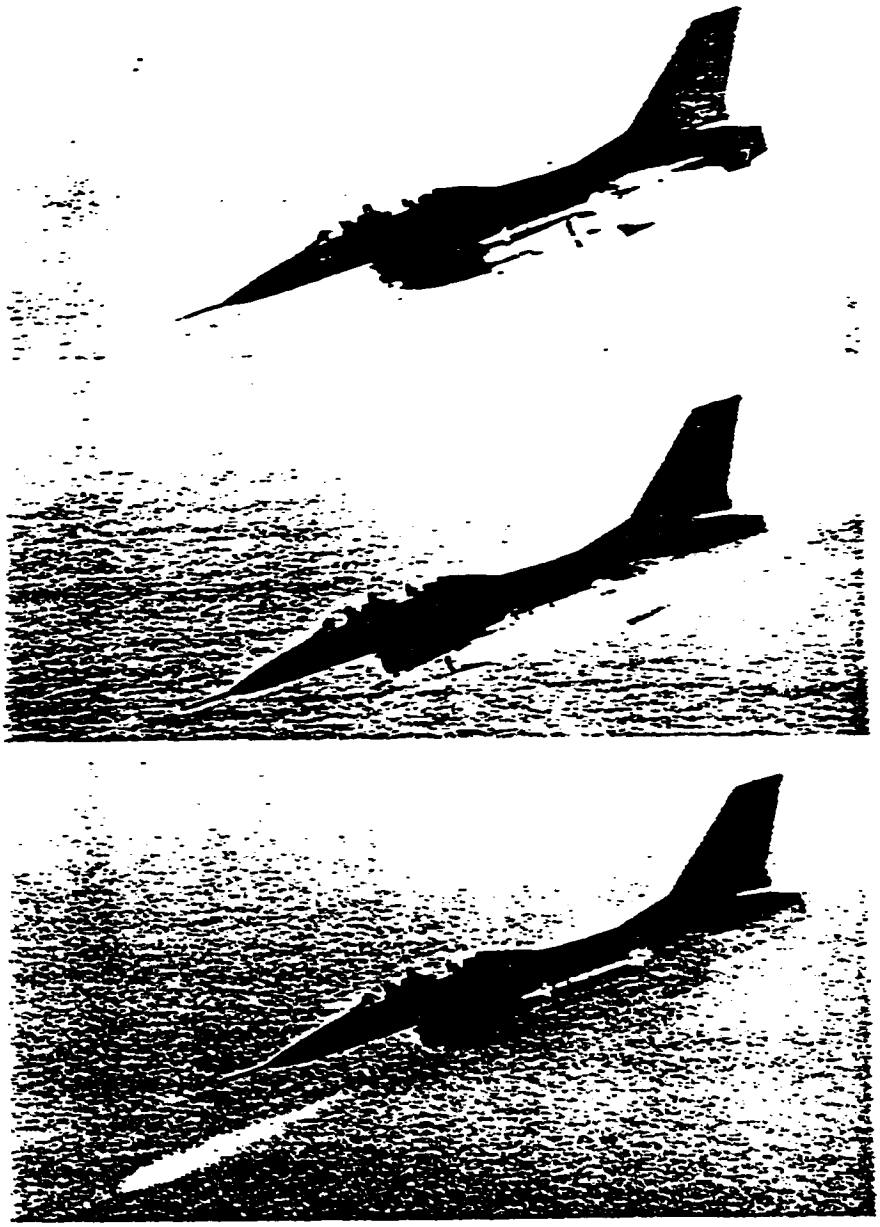

Figure 1.2 : Launch of an AGM-65 Air-To-Surface Missile of an F-16 B [14].

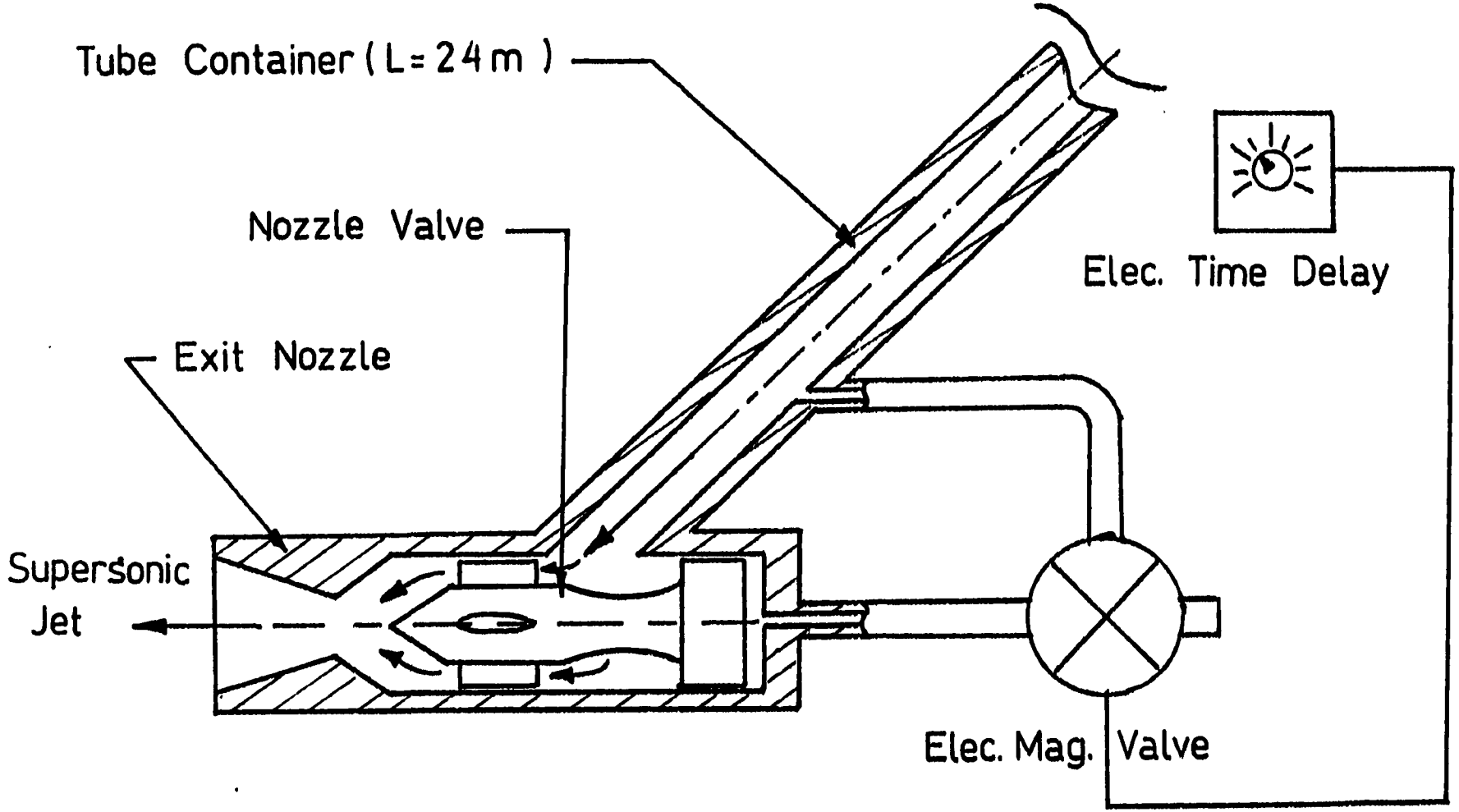

Figure2.1A: The Tube Wind Tunnel (Ludwieg Tube) .

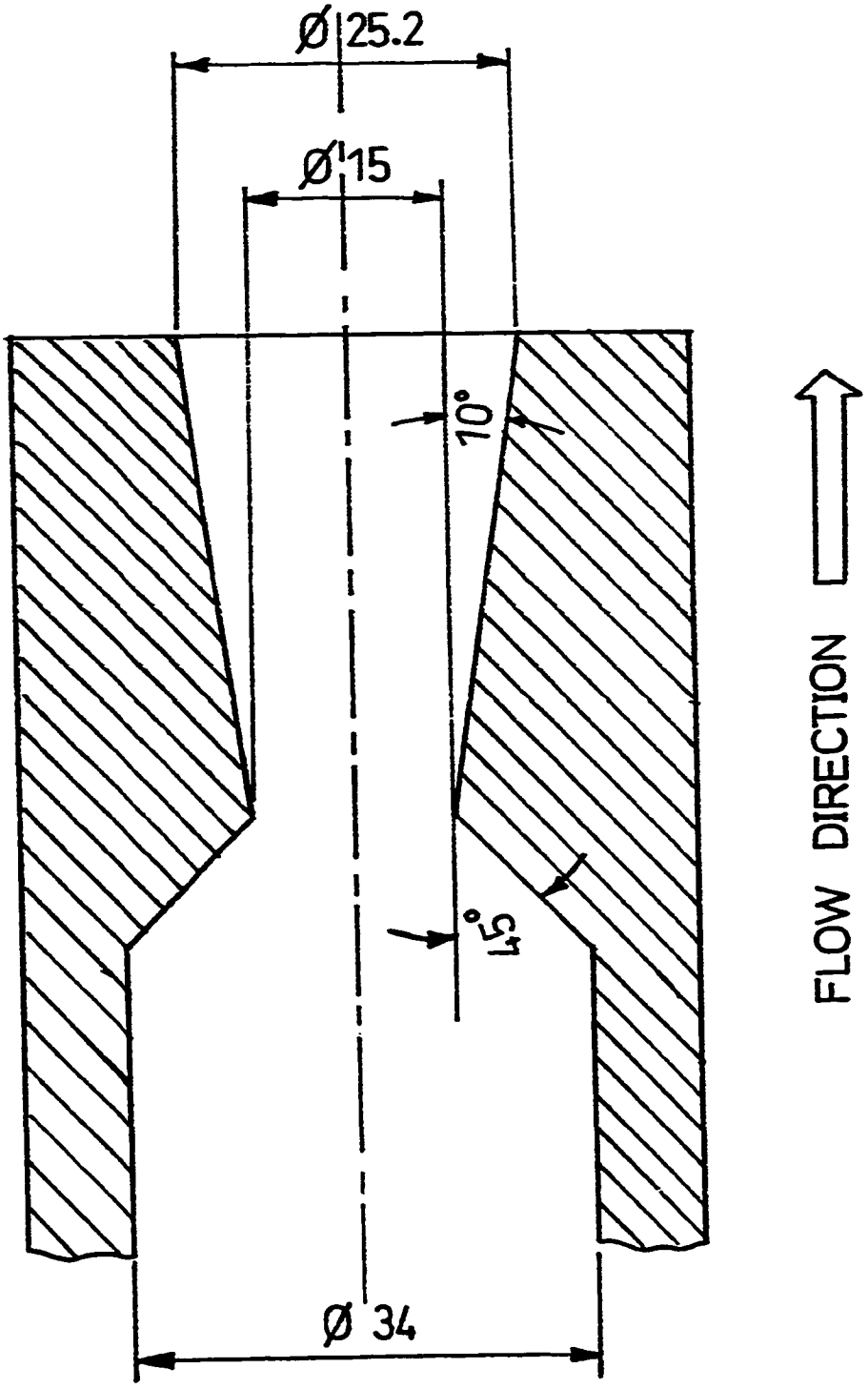

Figure 2.1 B: Jet nozzle .

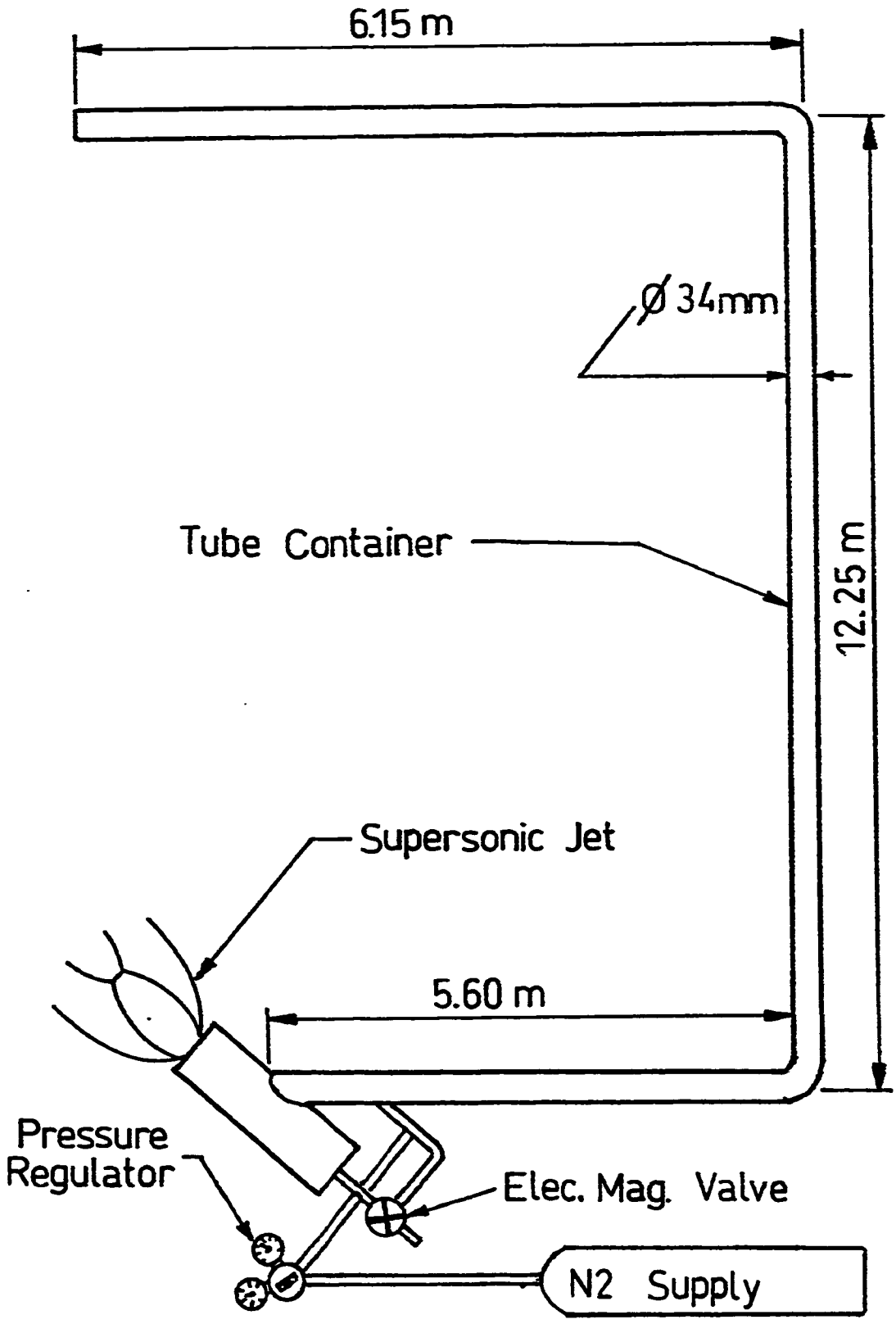

Figure 2.2 : Tube Tunnel Layout (KFUPM).

	D1 (mm)	L1 (mm)	D 2 (mm)	L 2 (mm)
Pitot 1	4.0	113	3.2	57
Pitot 2	2,0	113	2.0	57
Pitot 3	1.6	70	2.0	100

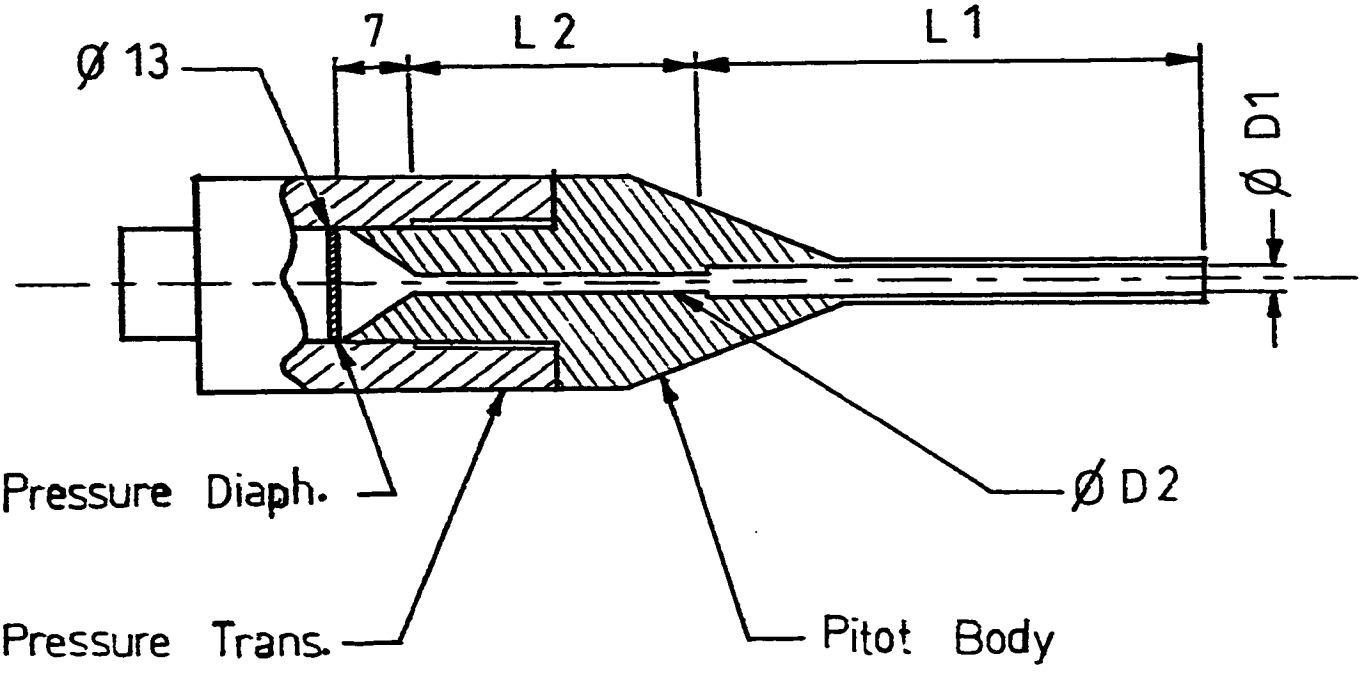

Figure 2.3 : Pitot assembly (time response exp.) .

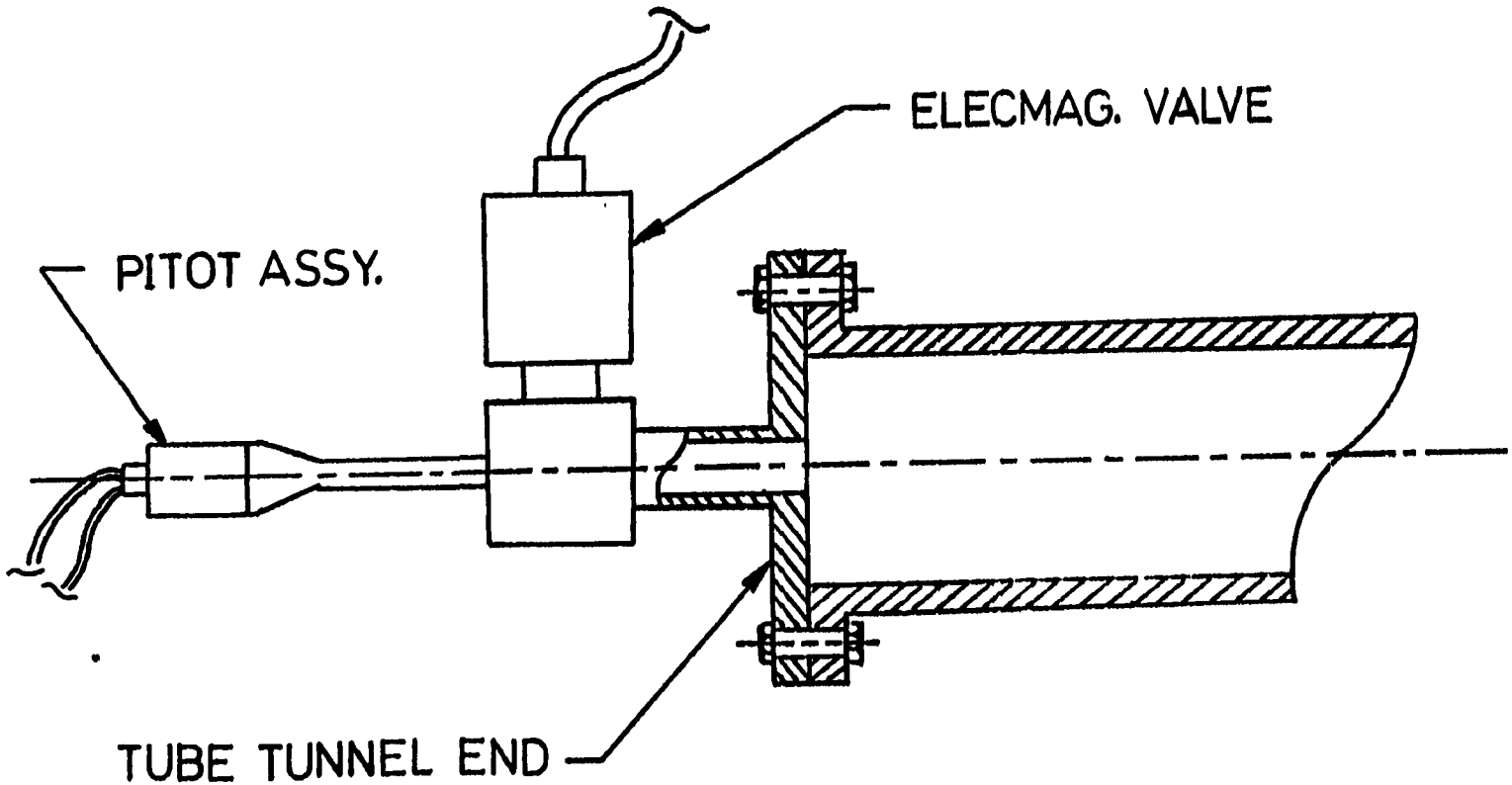

Figure 2.4 : Mechanical set up (pitot response).

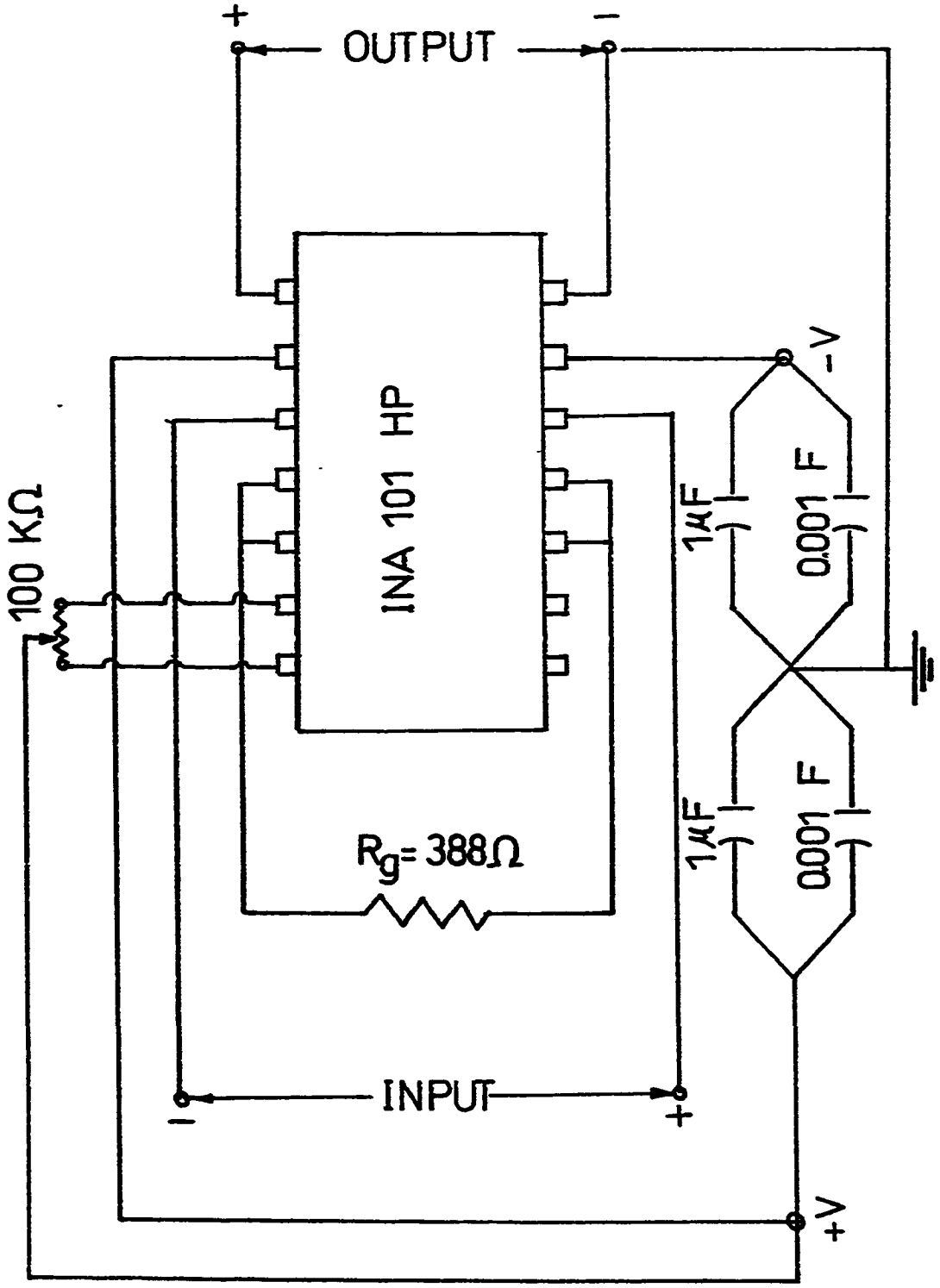

Figure 2.5: Operational amplifier for the pressure transducer.

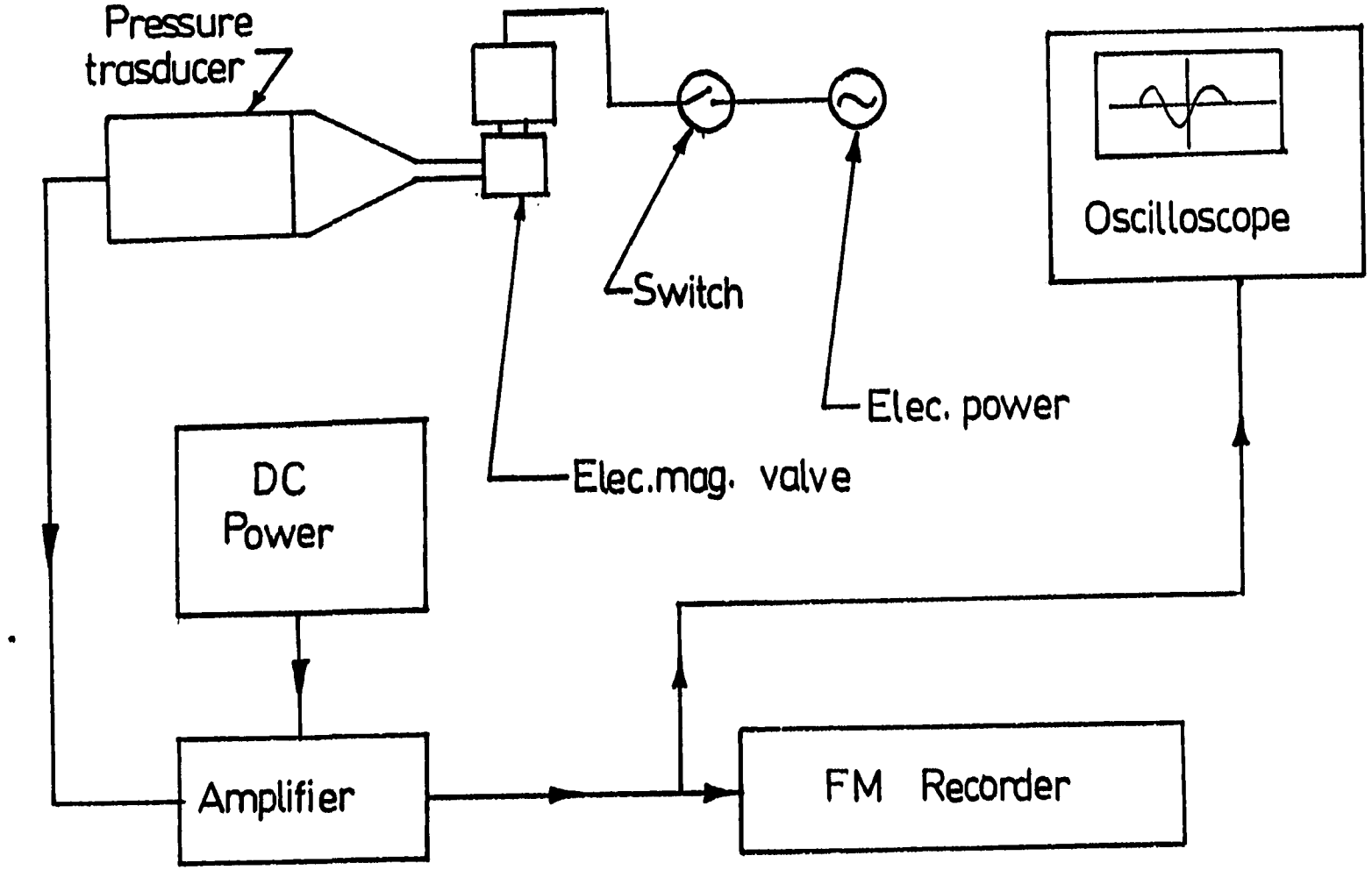

Figure 2.6 A : Pitot response (electrical set up) .

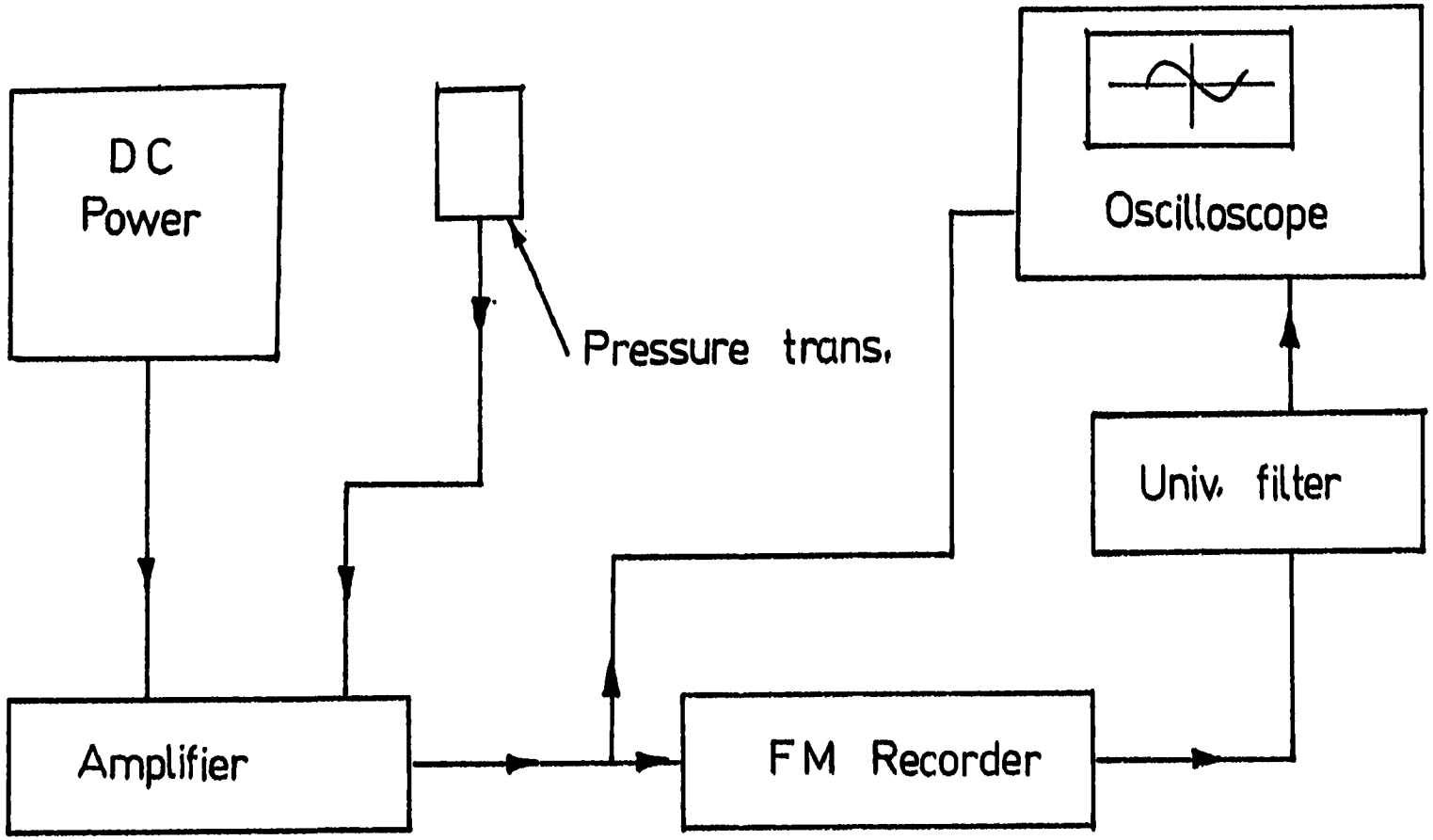

Figure 2.6B : Pitot pressure (electrical set up) .

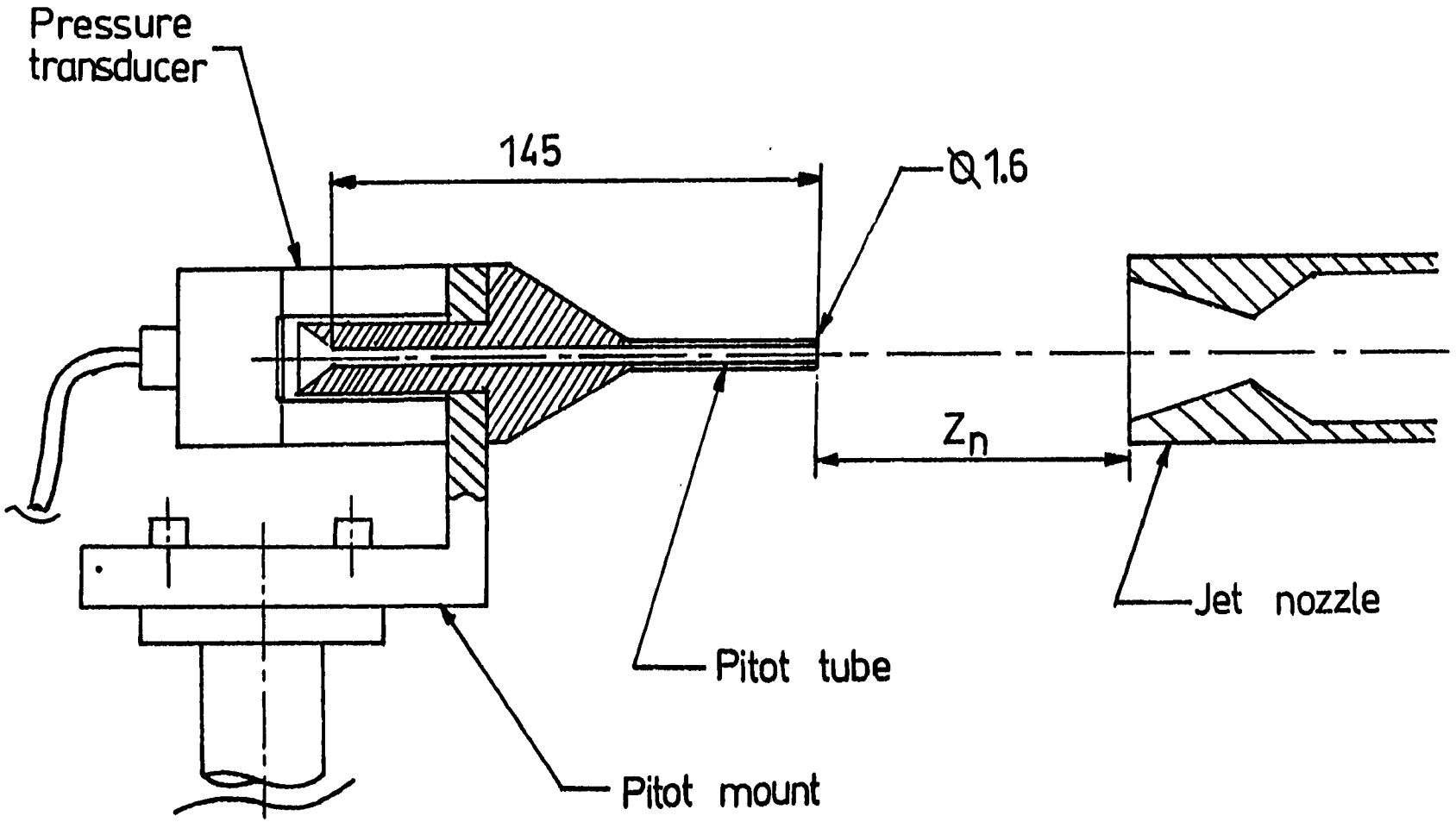

Figure 2.7 : Mechanical set-up of pitot pressure measurement.

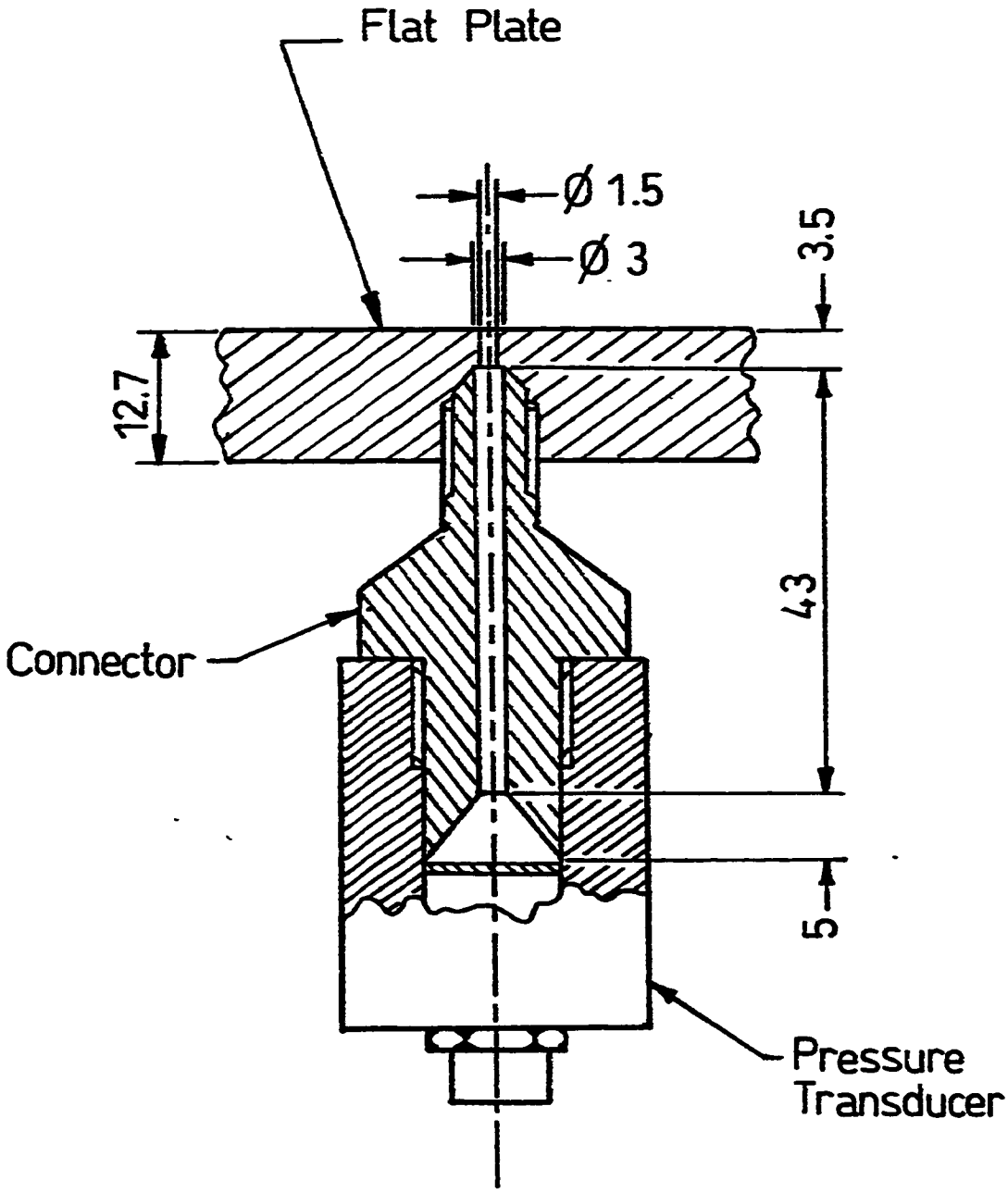

Figure 2.8 : Surface Pressure Connector .

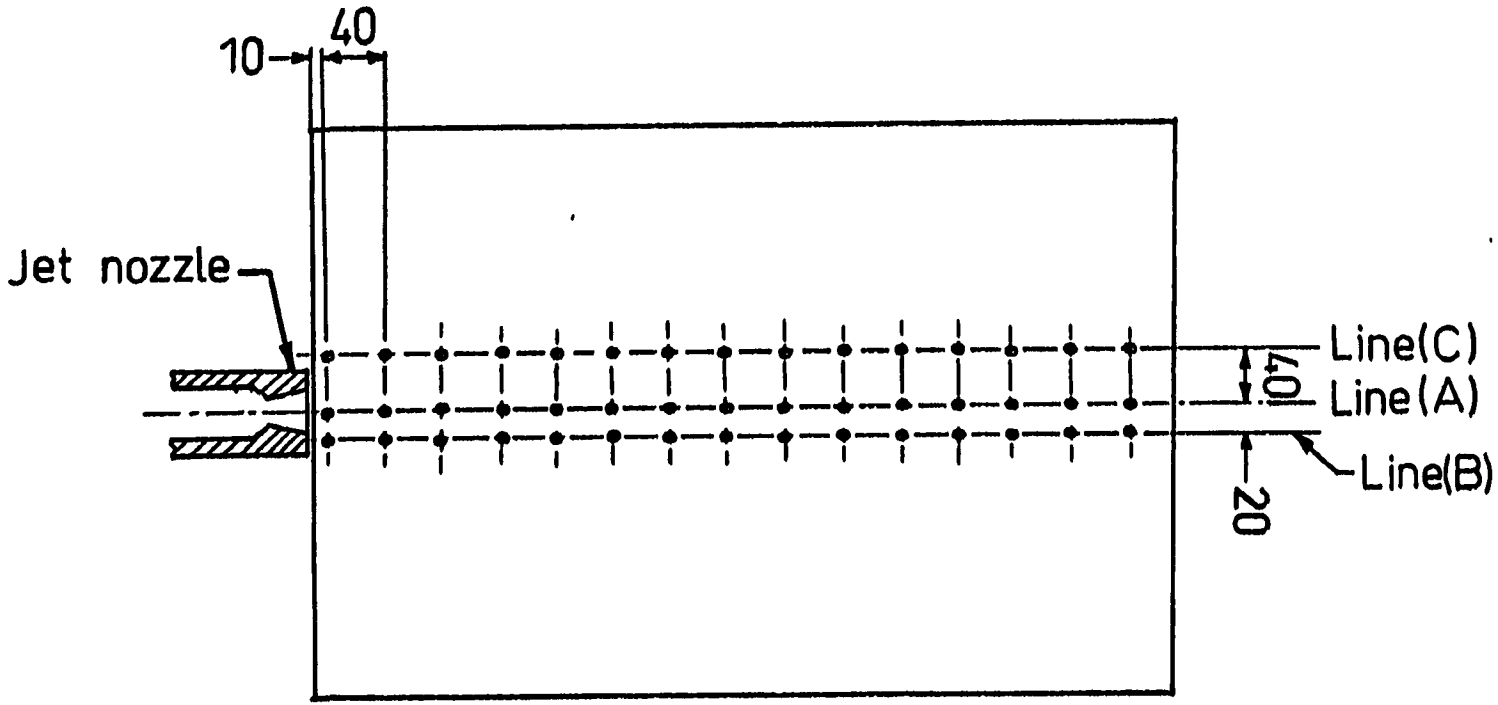

Figure 2.9 : Flat plate with pressure holes.

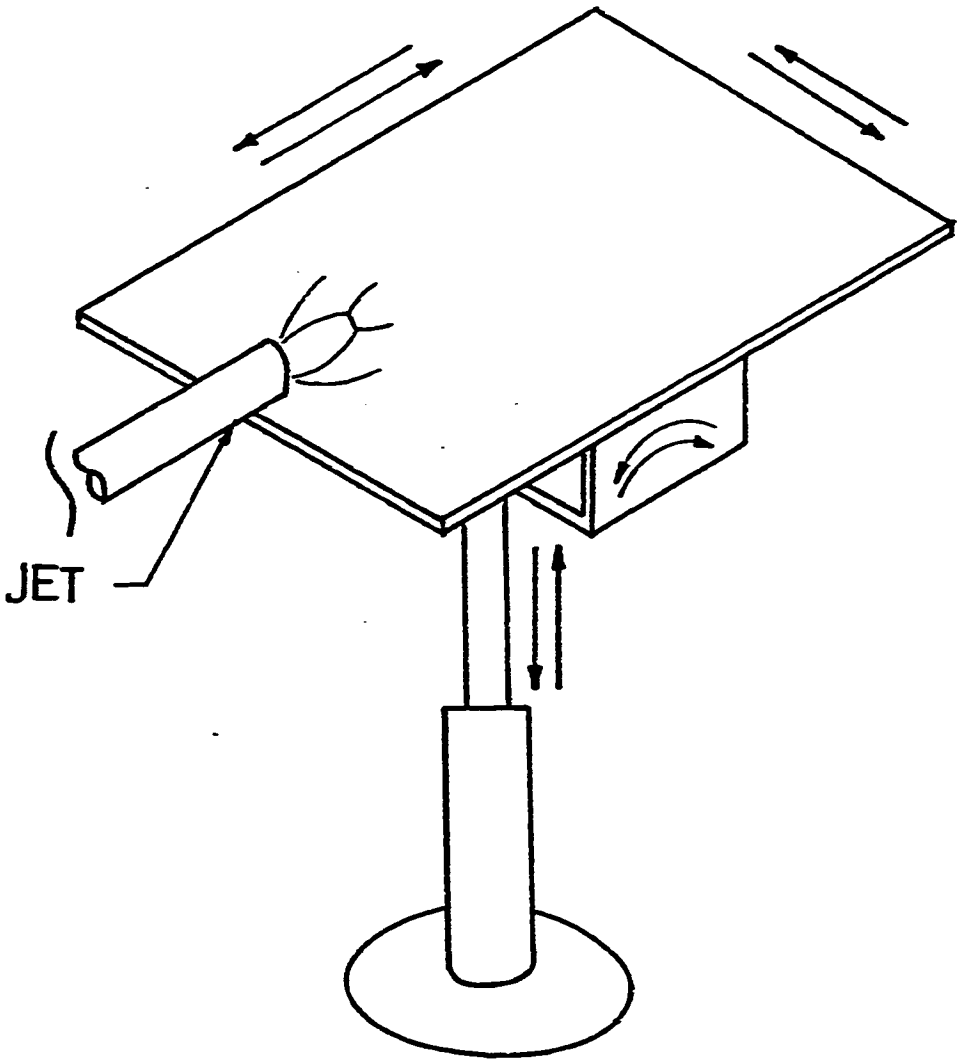

Figure 2.10 : Flat plate assembly.

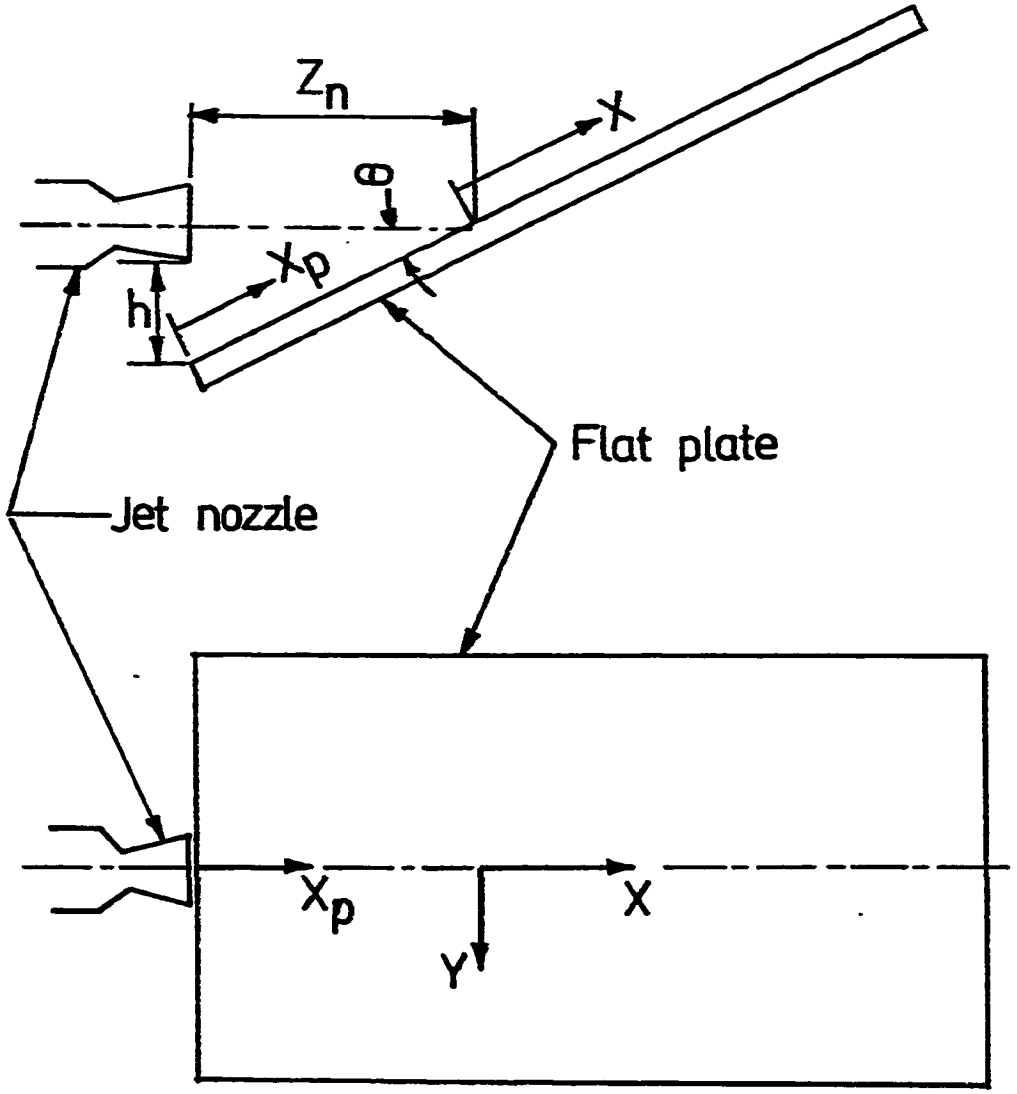

Figure 2.11 : Flat plate axis .

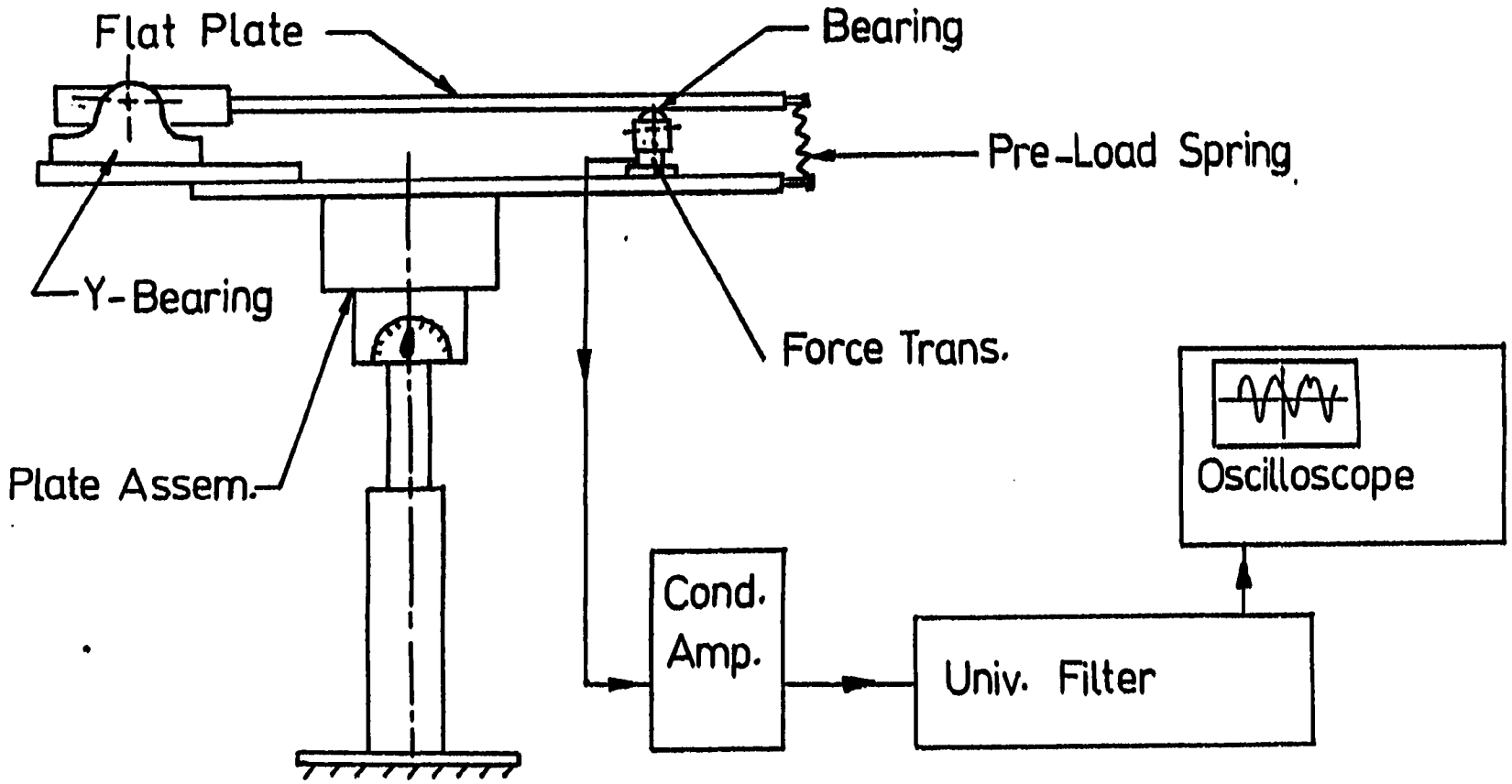

Figure 2.12 : Natural Frequencies Mechanical and Electrical Set-up .

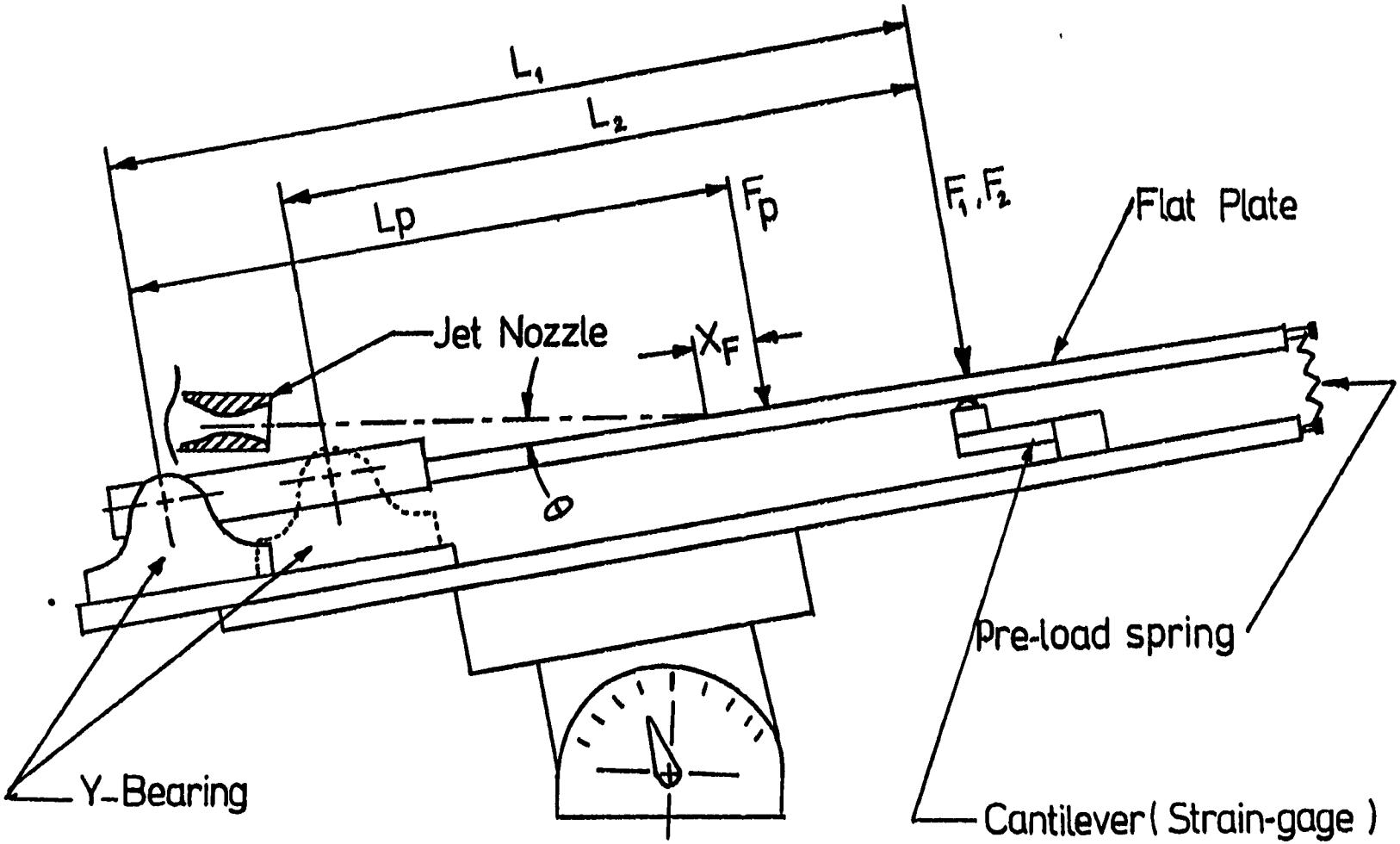

Figure 2.13 : Force measurement (Mechanical set-up).

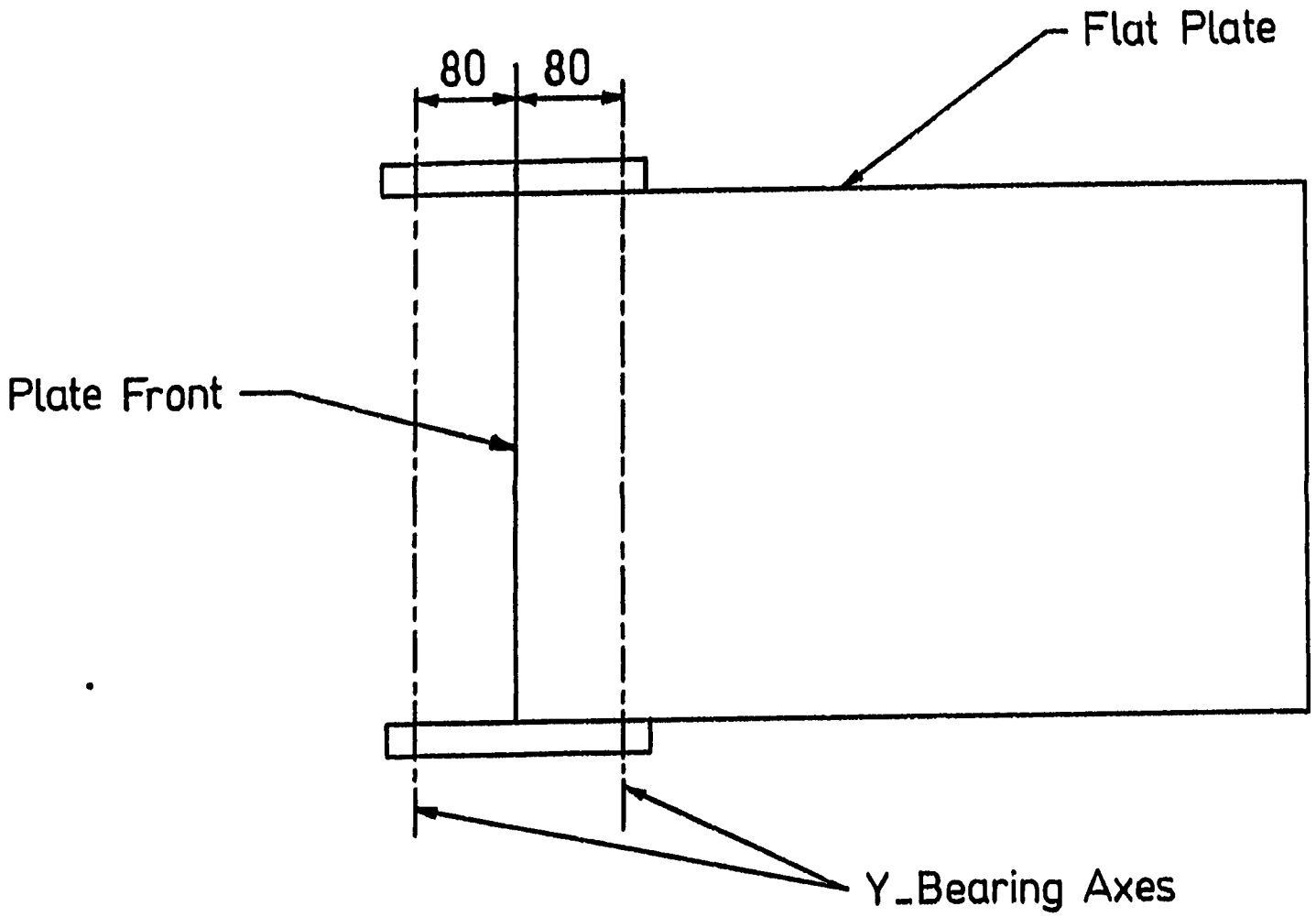

Figure 2.14 : Flat plate bearing axes locations .

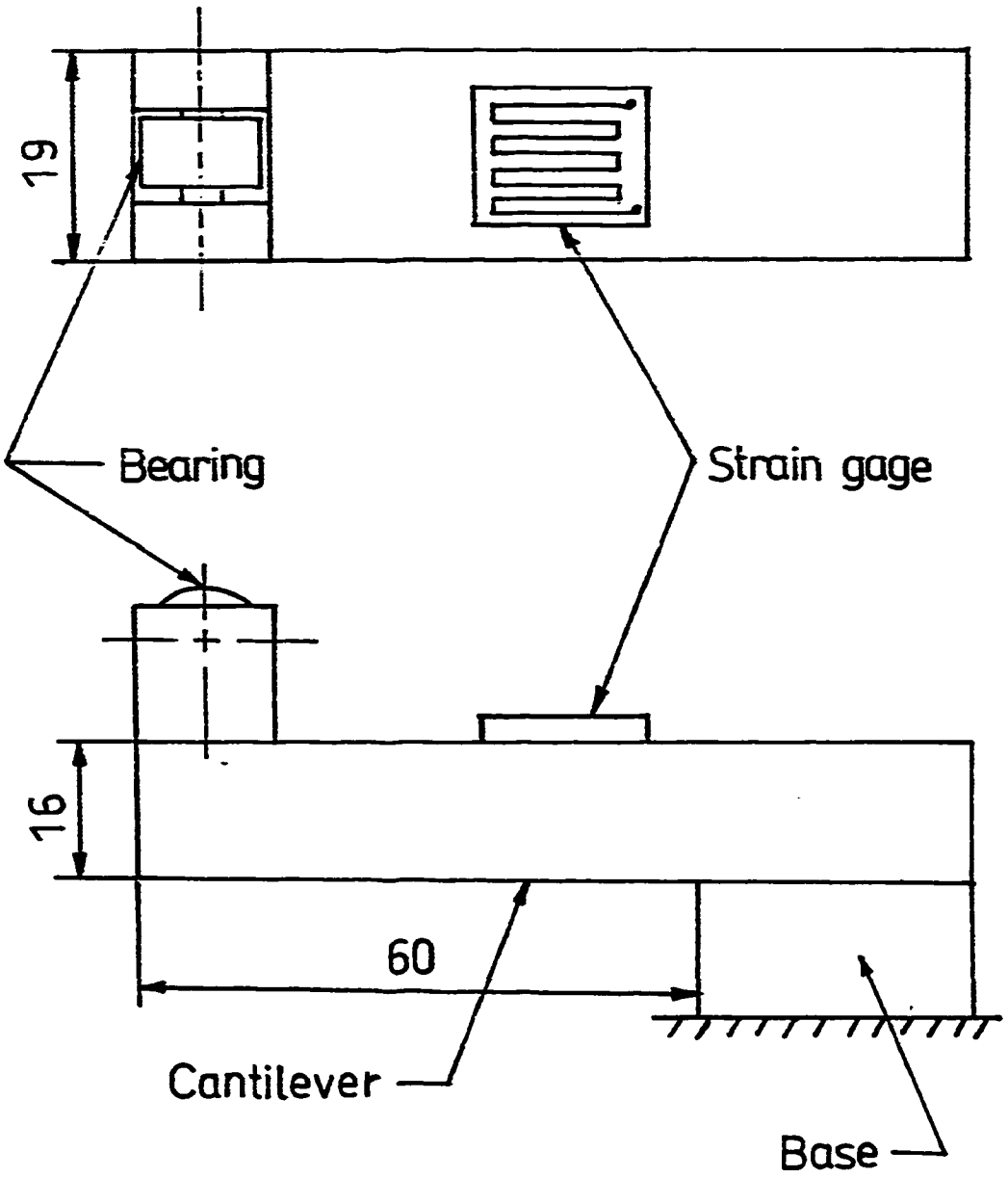

Figure 2.15: Strain gage and cantilever assembly .

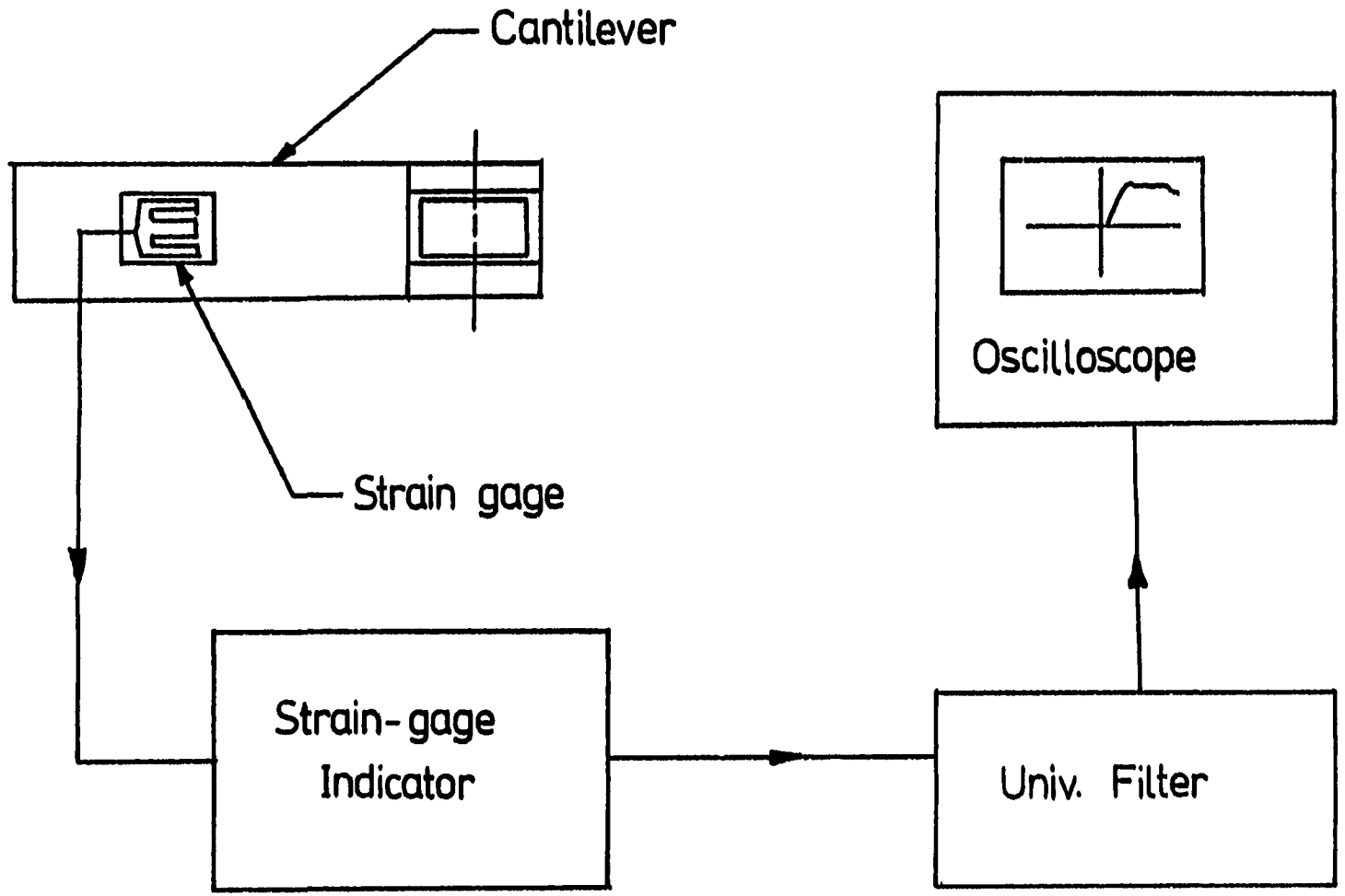

Figure 2.16 : Force measurement Electrical set-up .

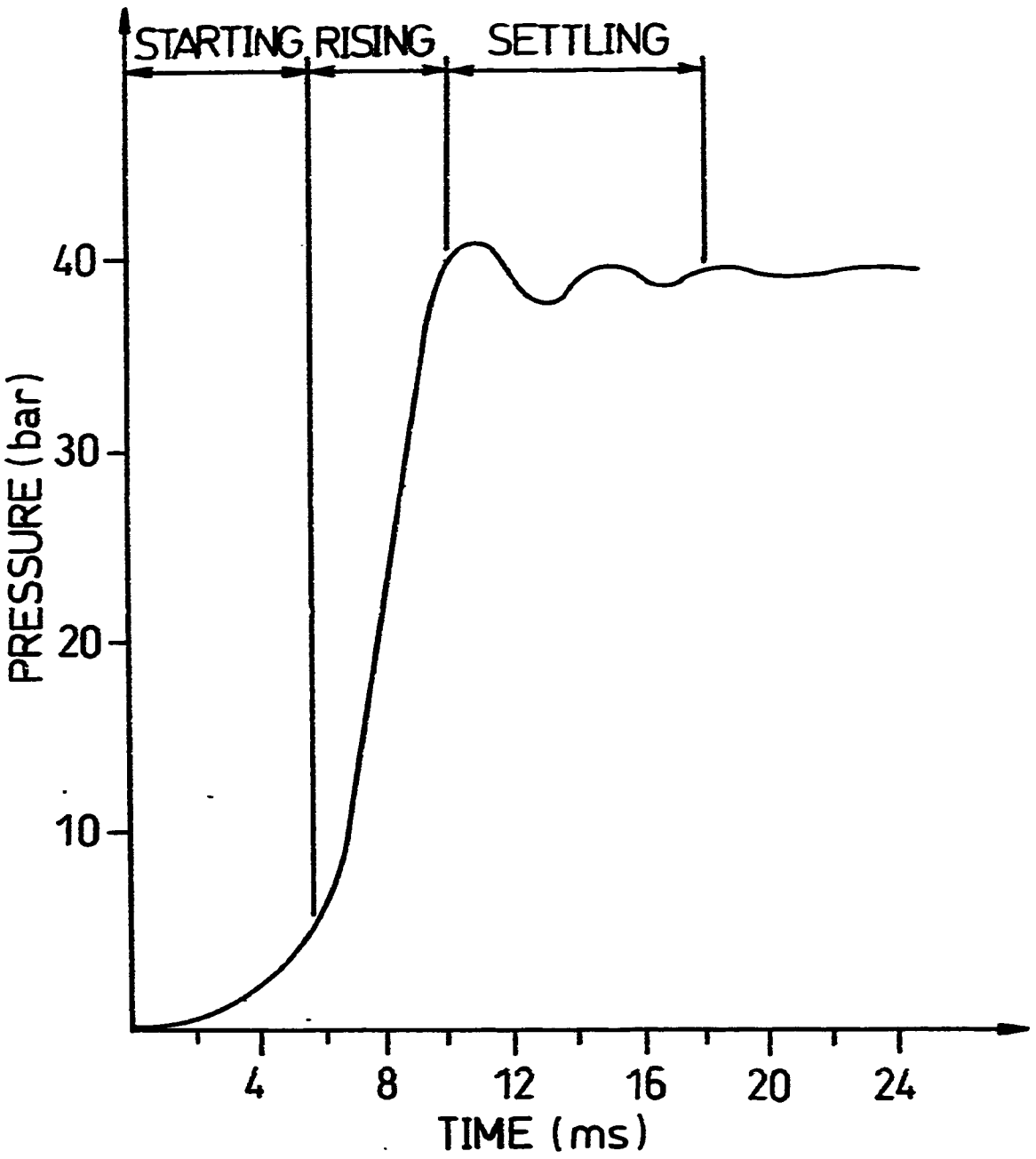

Figure 3.1 : Pitot assembly output signal (40 bar).

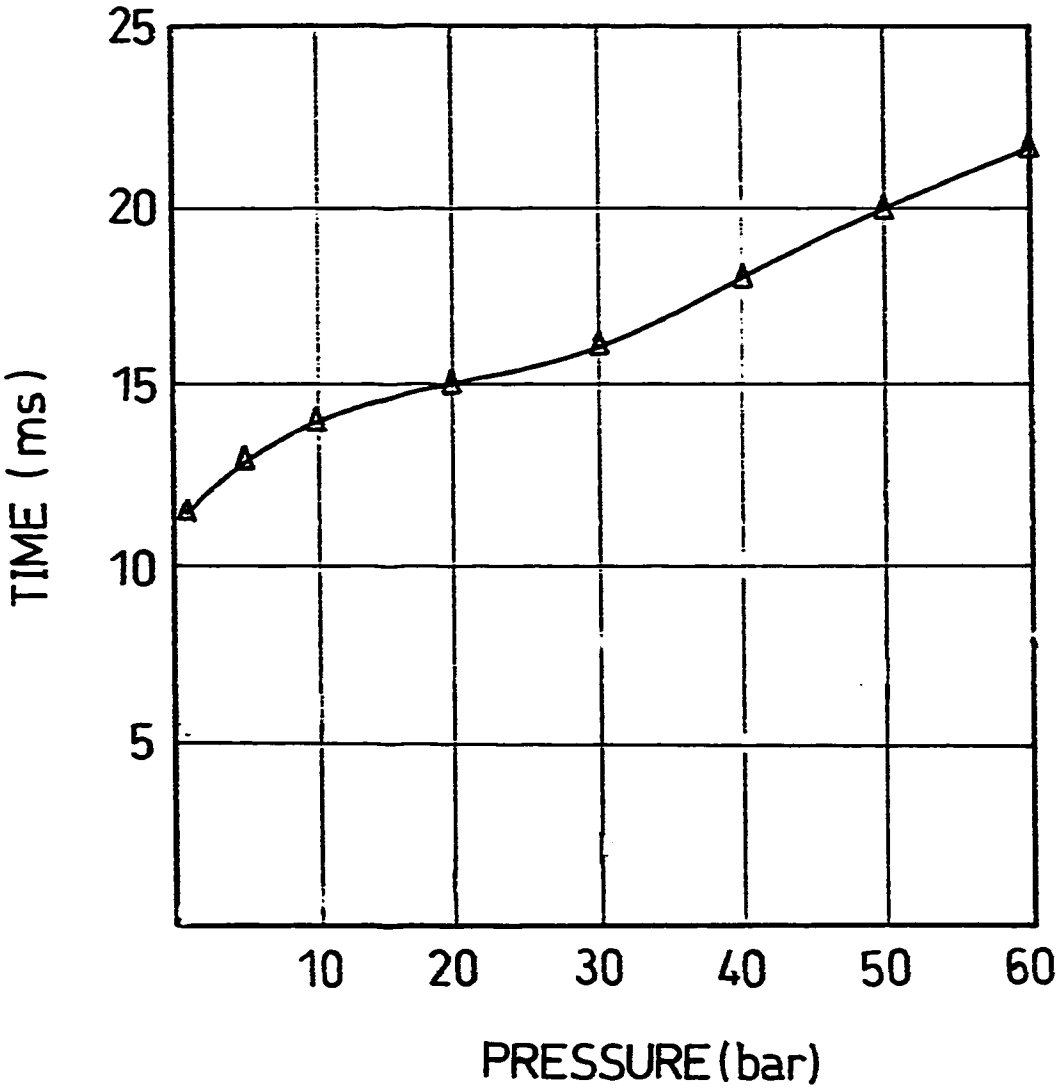

Figure 3.2 : Pitot assembly (1) response .

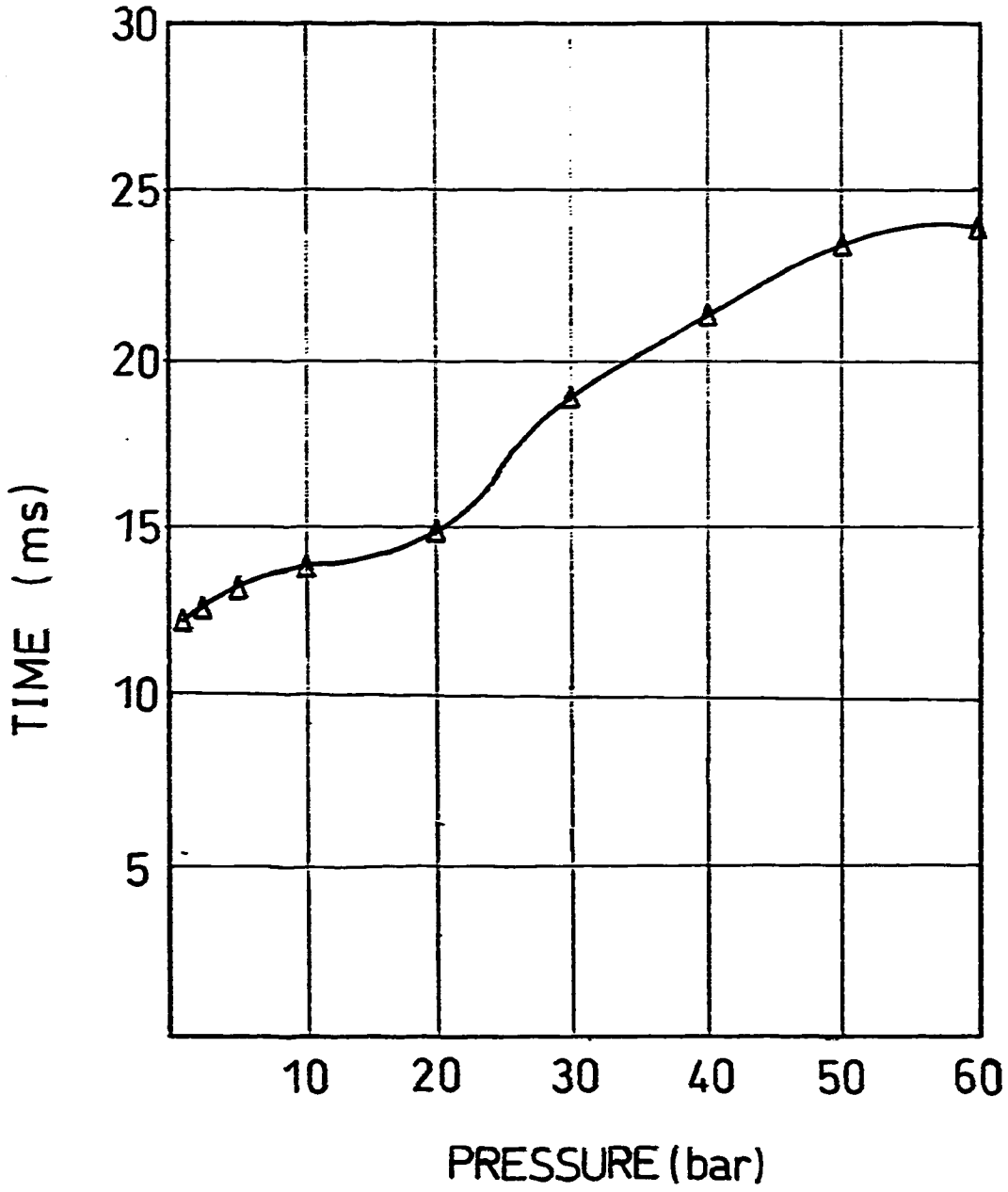

Figure 3.3 : Pitot assembly (2) response .

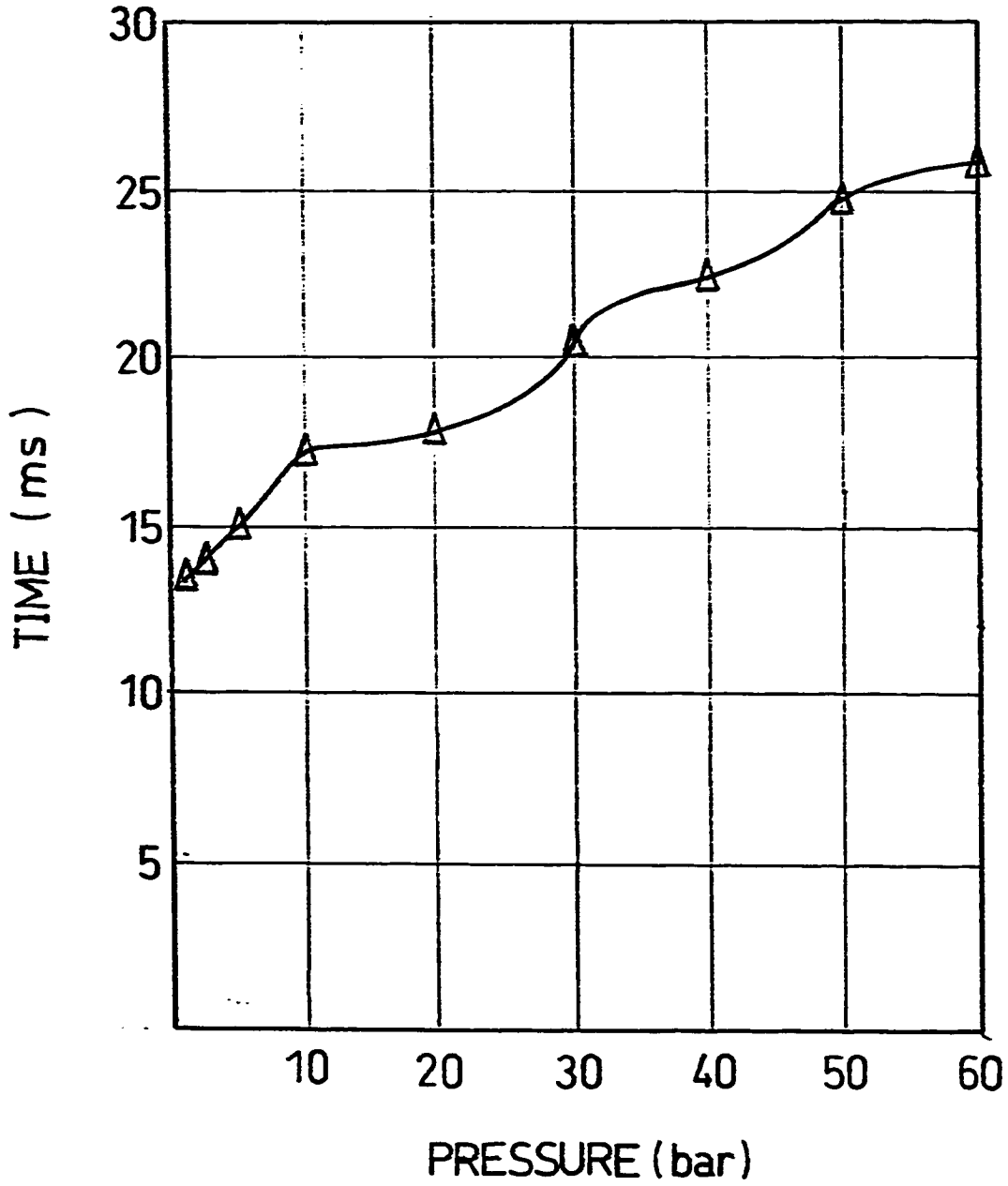

Figure 3.4 : Pitot assembly (3) response .

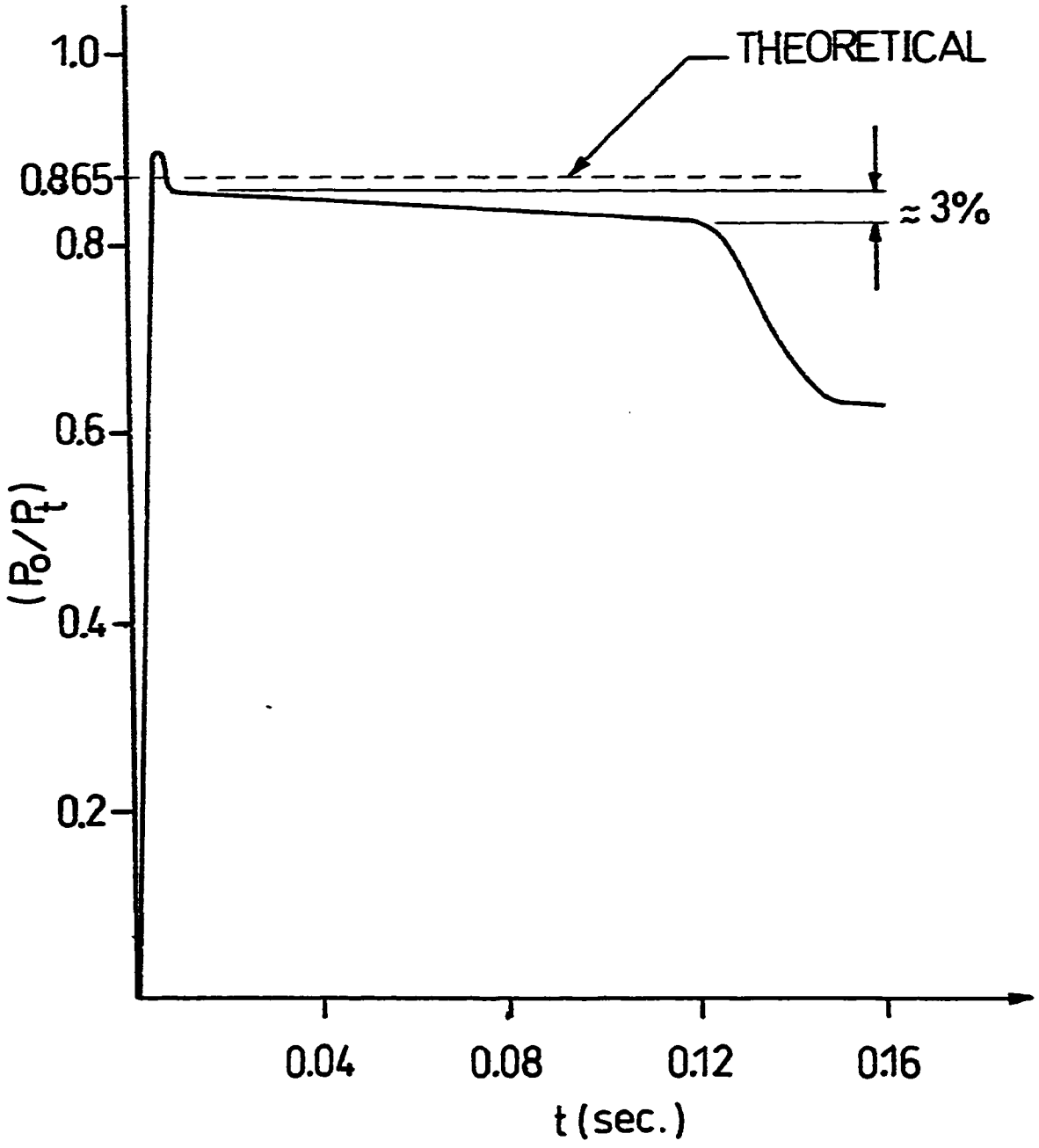

Figure 3.5 : Stagnation Pressure of The Free Jet .

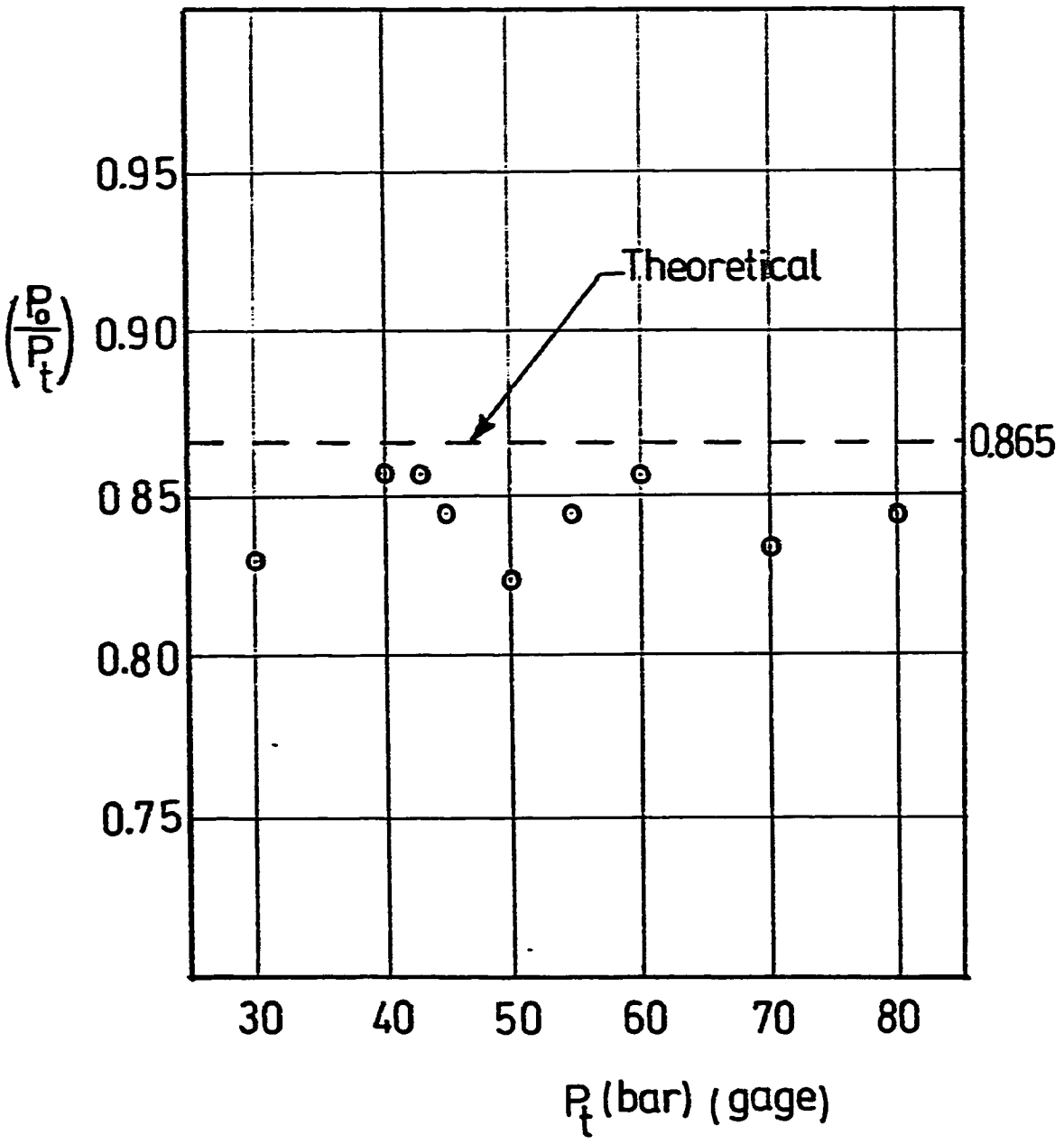

Figure 3.6 : Stagnation pressure at different (P_t) .

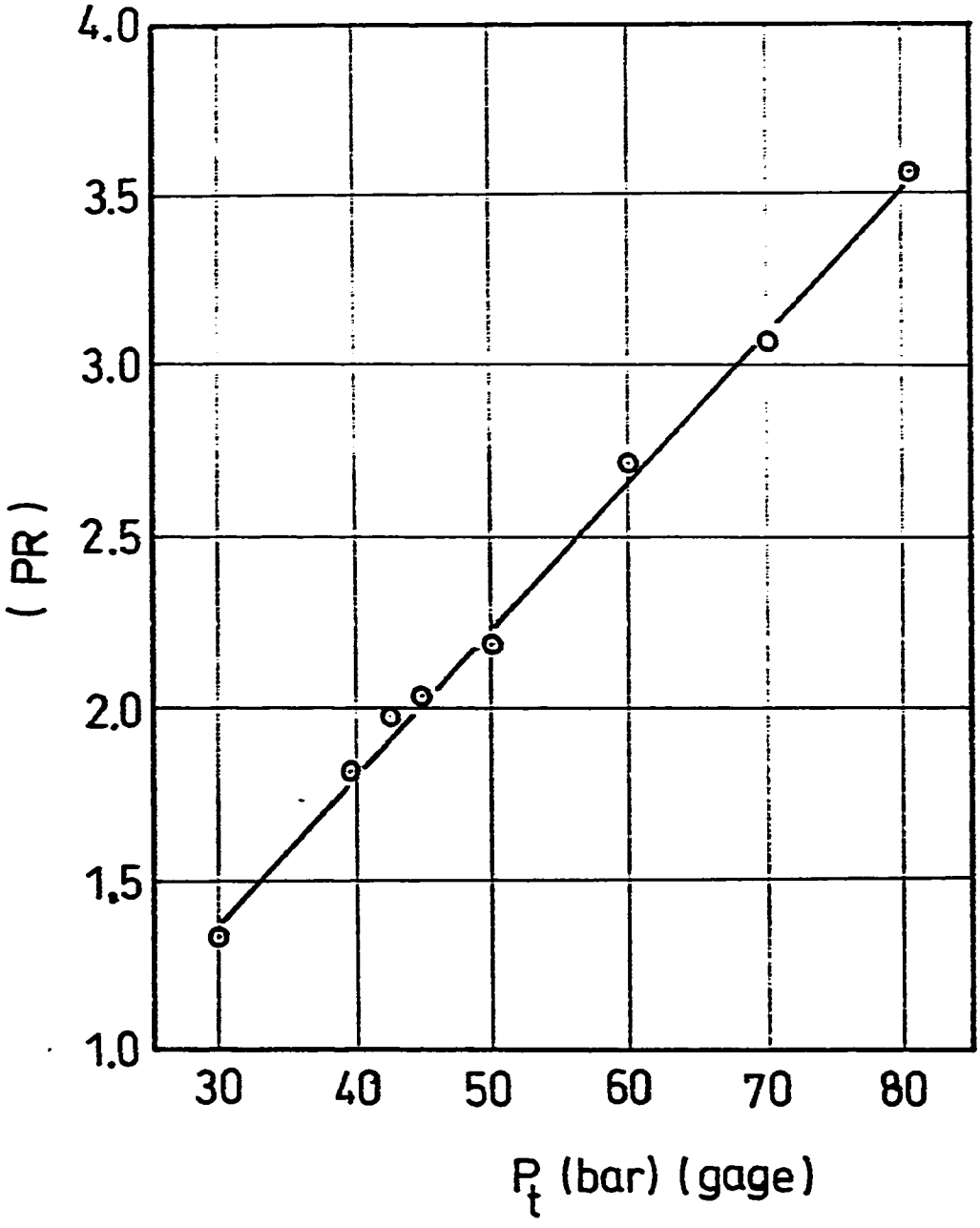

Figure 3.7 : Jet underexpantion ratio at different (P_t).

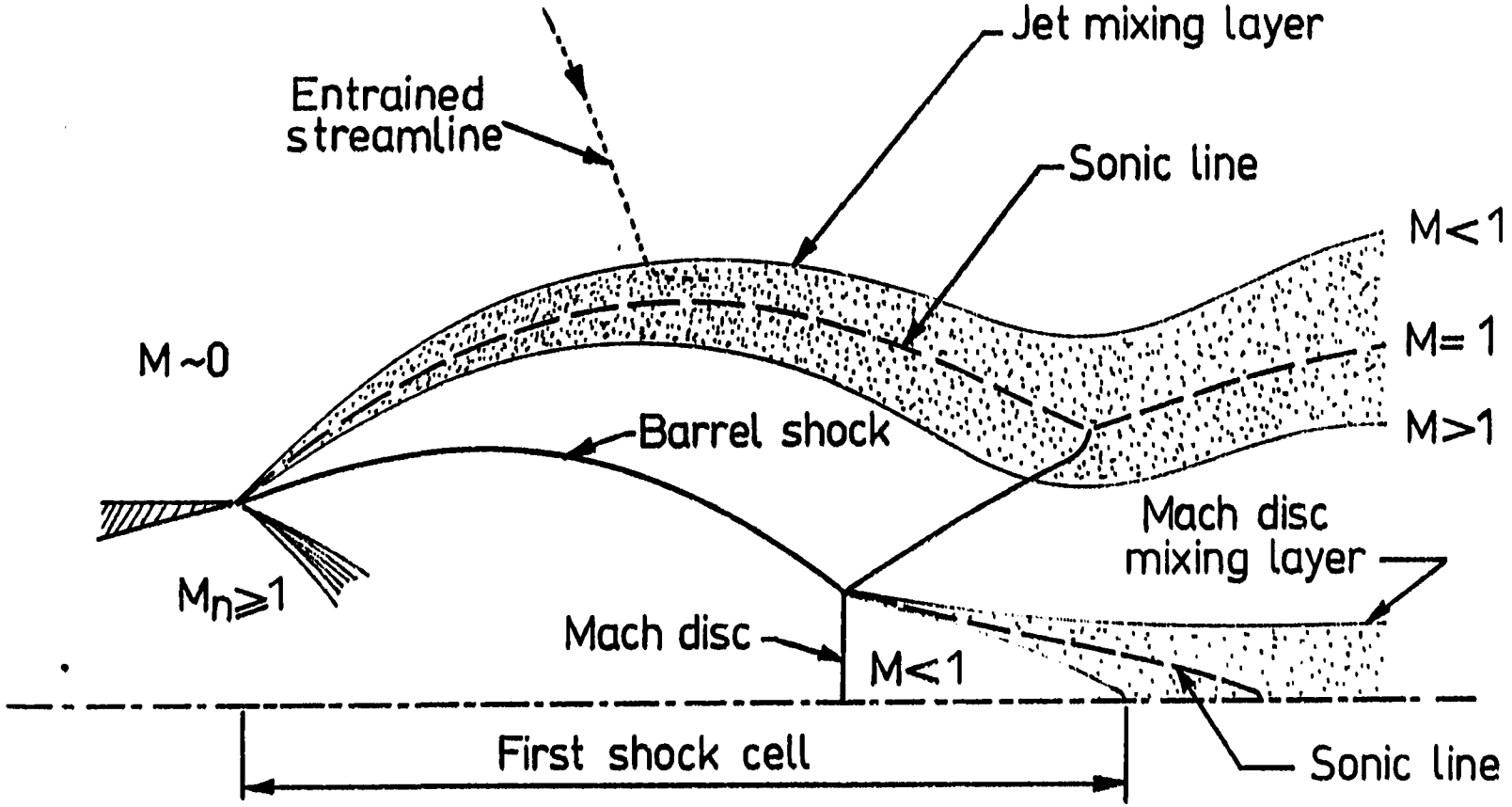

Figure 3.8A : Underexpanded supersonic jet near field structure [13].

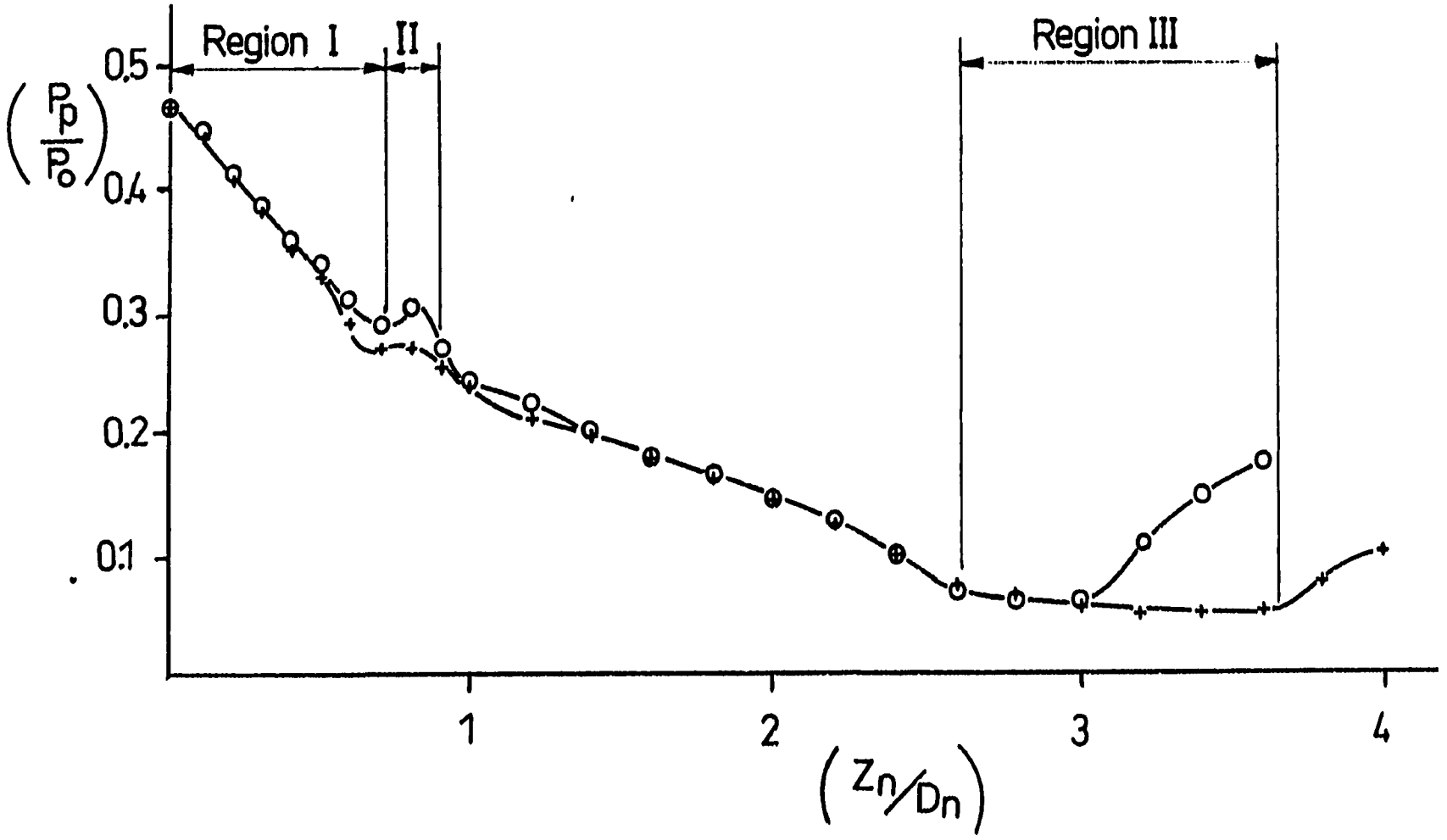

Figure 3.8 B: Pitot pressure distribution of the free jet $M_n = 2.57$.
—o—, PR = 2; —+—, PR = 2.2.

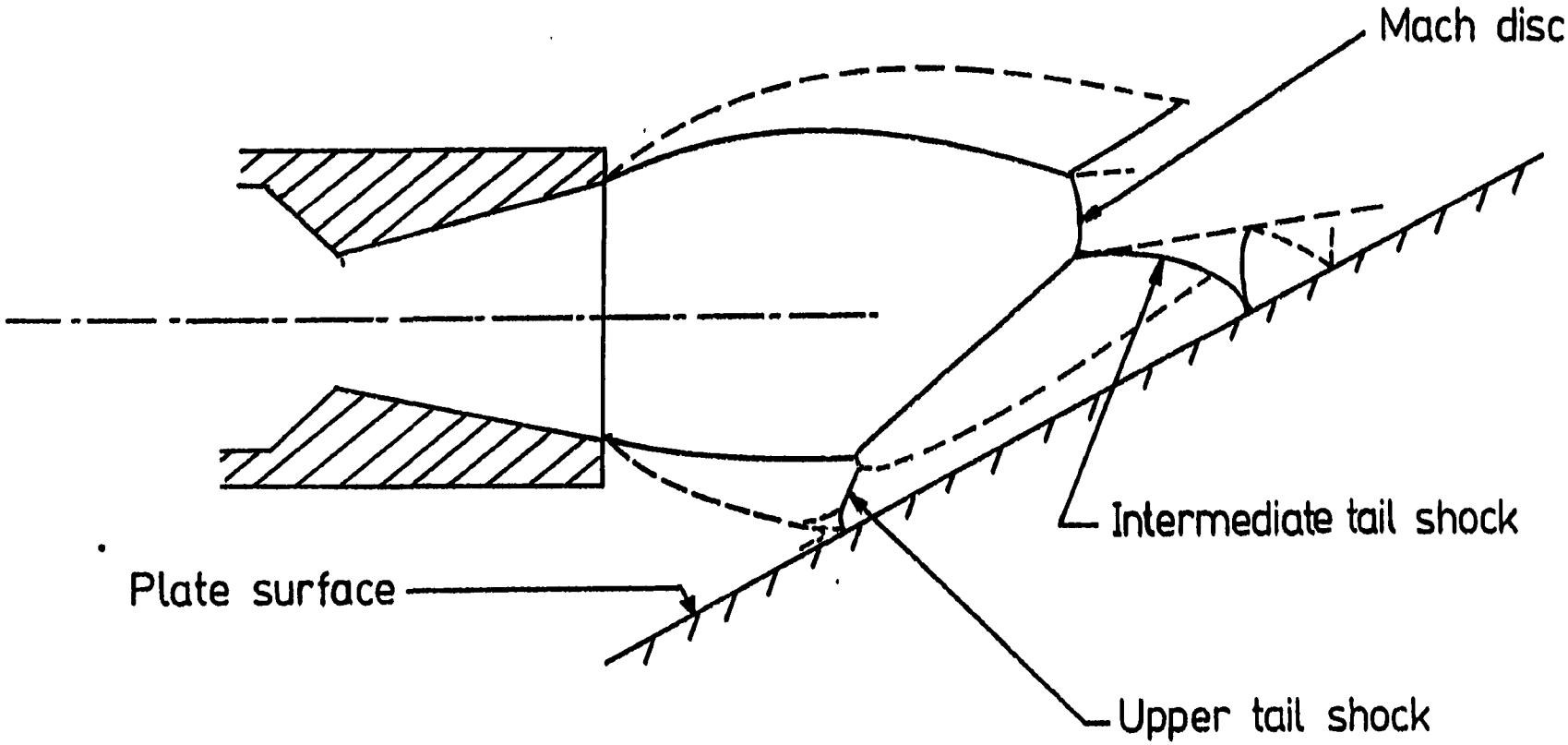

Figure 3.8C : Reconstruction of shadowgraph for the interaction of the jet with the plate surface at $\theta=30^{\circ}$, $Z_n/D_n=2$, [2].

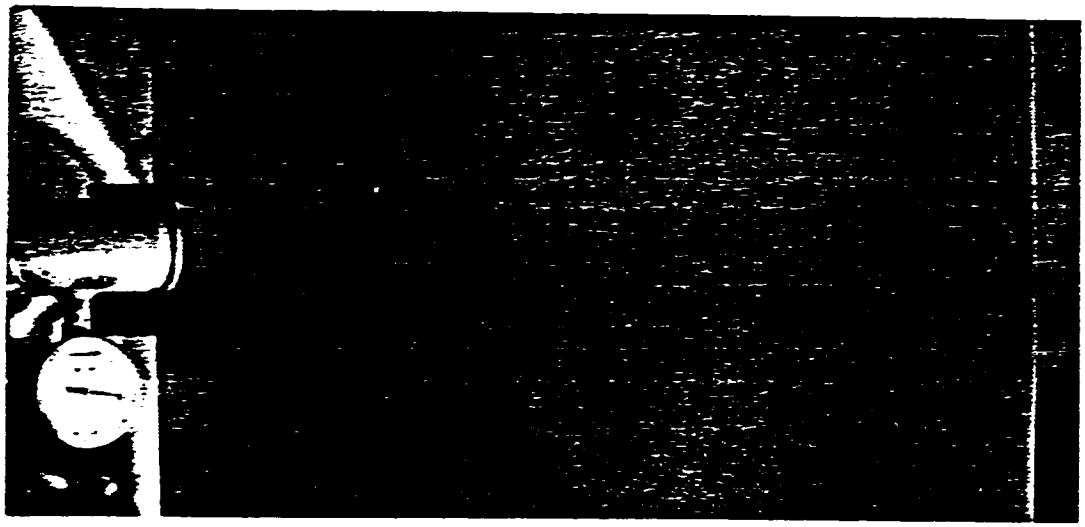

$\vdash\dashv D_n$

Figure 3.9 A : Surface flow visualization for $\theta=30^{\circ}$, PR= 2 and $Z_n/D_n=2.1$.

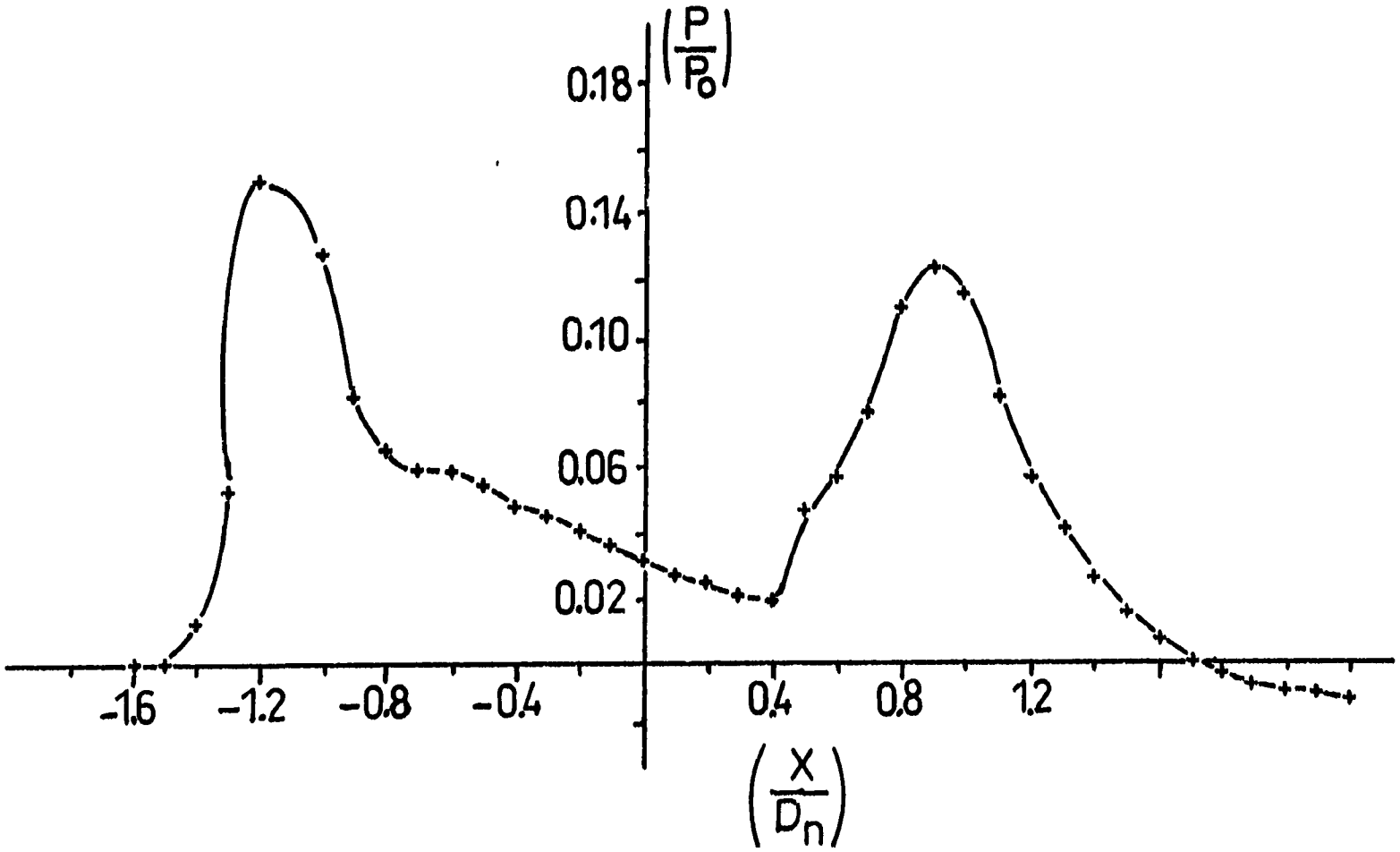

Figure 3.9B: Surface pressure along the centerline for $\theta = 30^{\circ}$, PR = 2 , $(Z_n/D_n) = 2.1$.

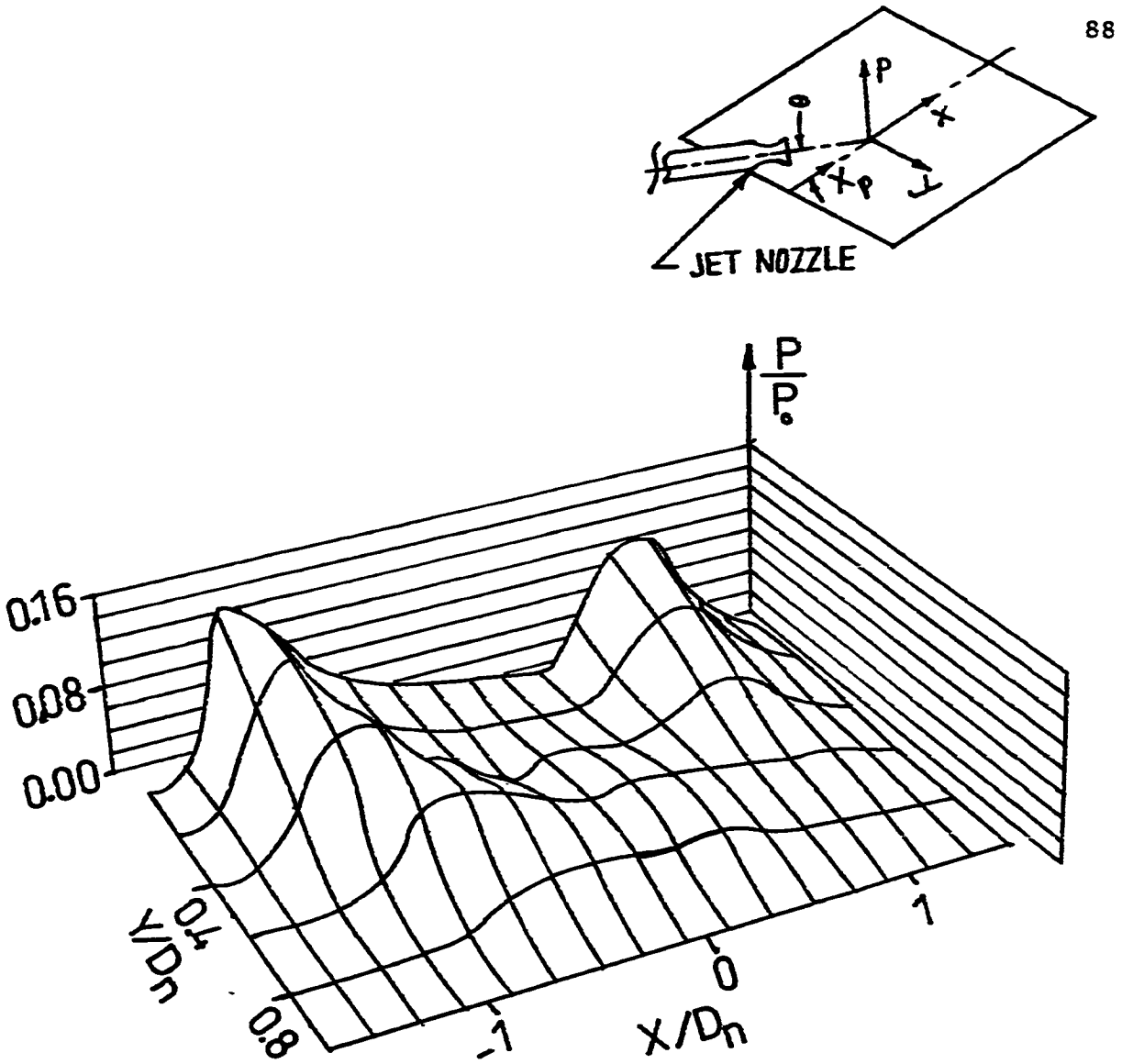

Figure 3.9 C: Surface pressure distribution (half) for $\theta = 30°$, PR = 2 , $(Z_n/D_n) = 2.1$.

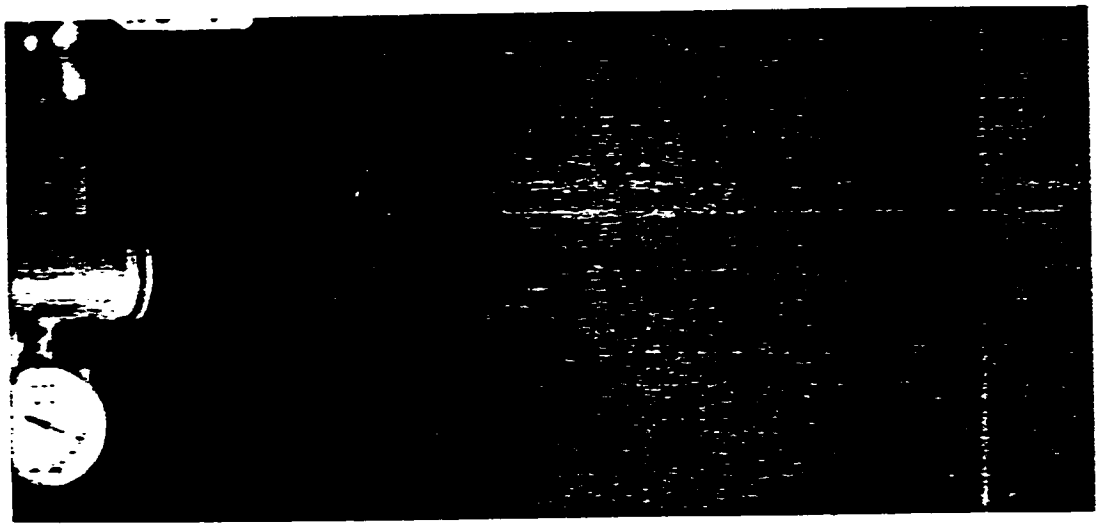

$\vdash\!\dashv D_n$

Figure 3.10 A : Surface flow visualization for $\theta=30°$, PR=2.2 and $Z_n/D_n=7.2$.

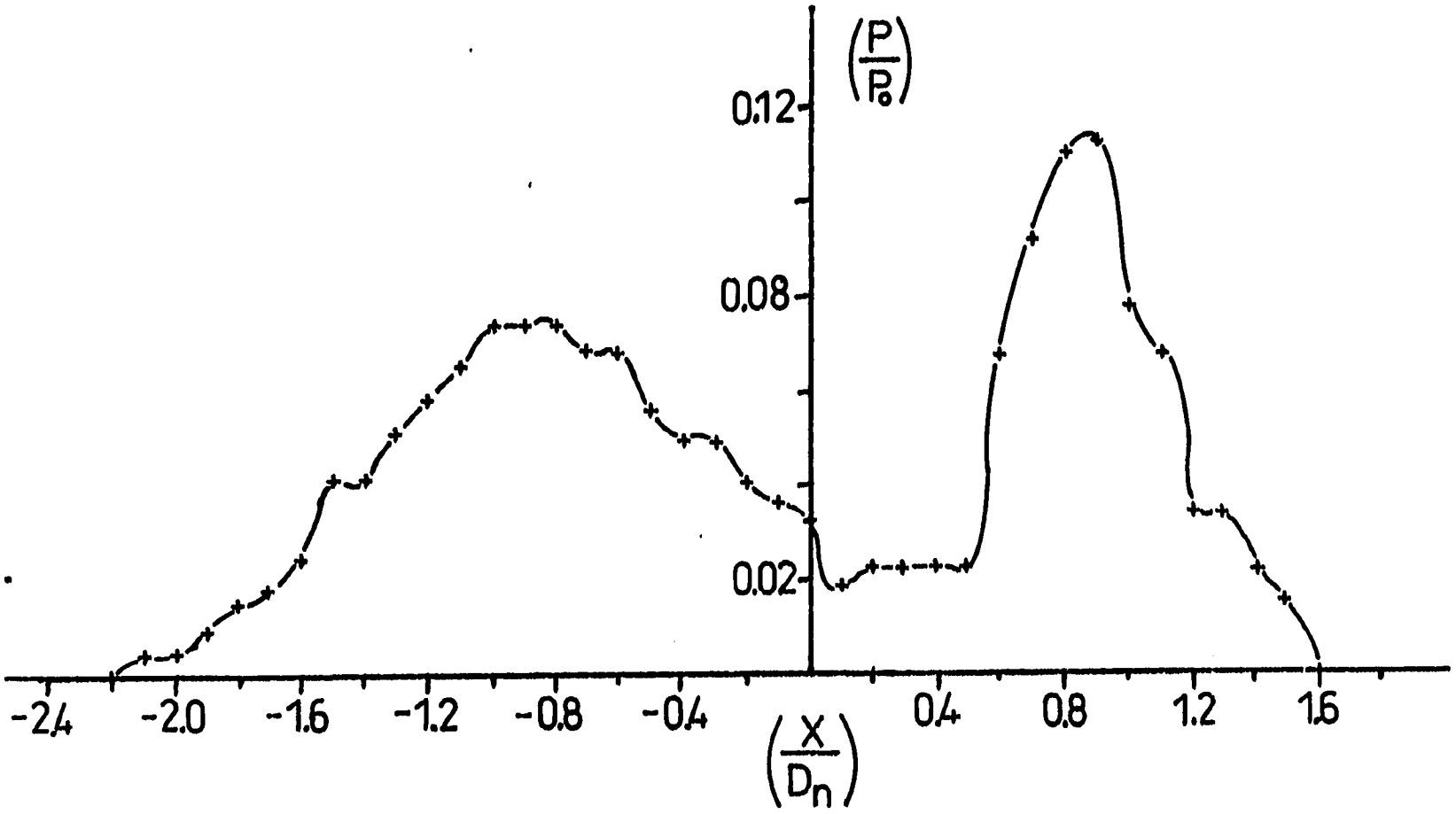

Figure 3.10B: Surface pressure along the centerline for $\theta = 30^{\circ}$, PR = 2.2 , $(Z_n/D_n) = 7.2$.

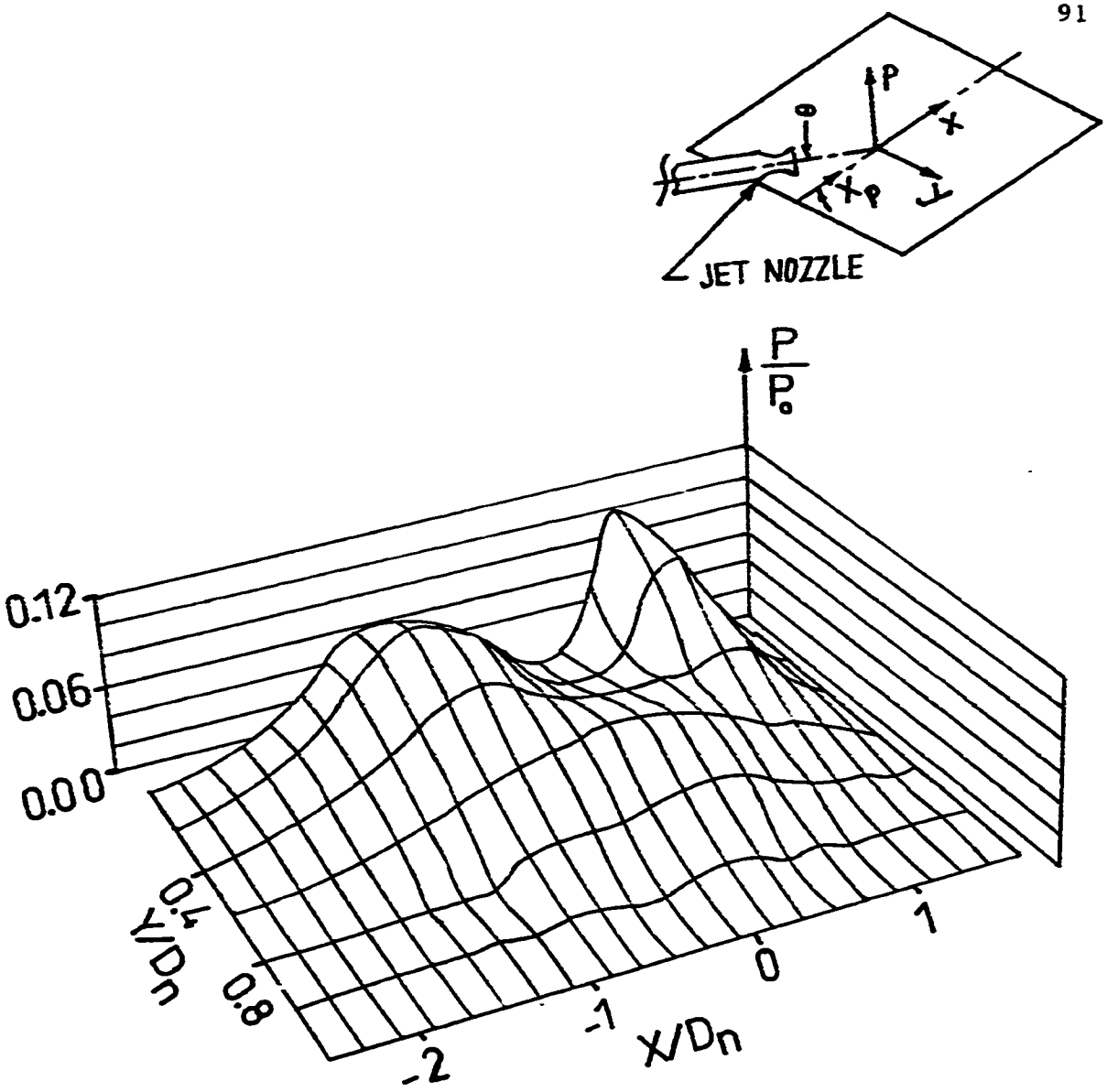

Figure3.10C: Surface pressure distribution (half) for $\theta = 30^{\circ}$, PR=2.2 , $(Z_n/D_n) = 7.2$.

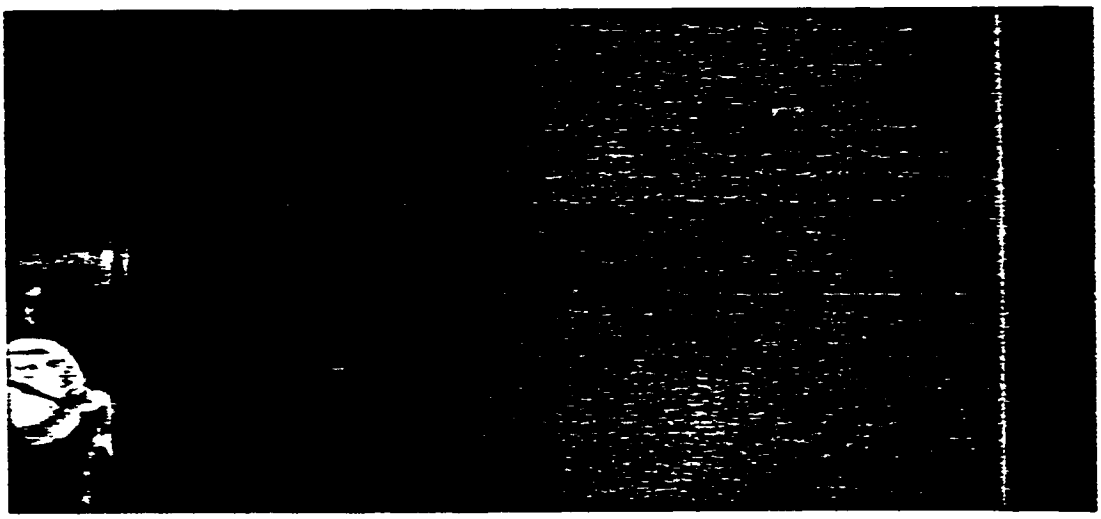

$\vdash\dashv D_n$

Figure 3.11 A: Surface flow visualization for $\theta=20°$, $PR=2.2$ and $Z_n/D_n=7.2$.

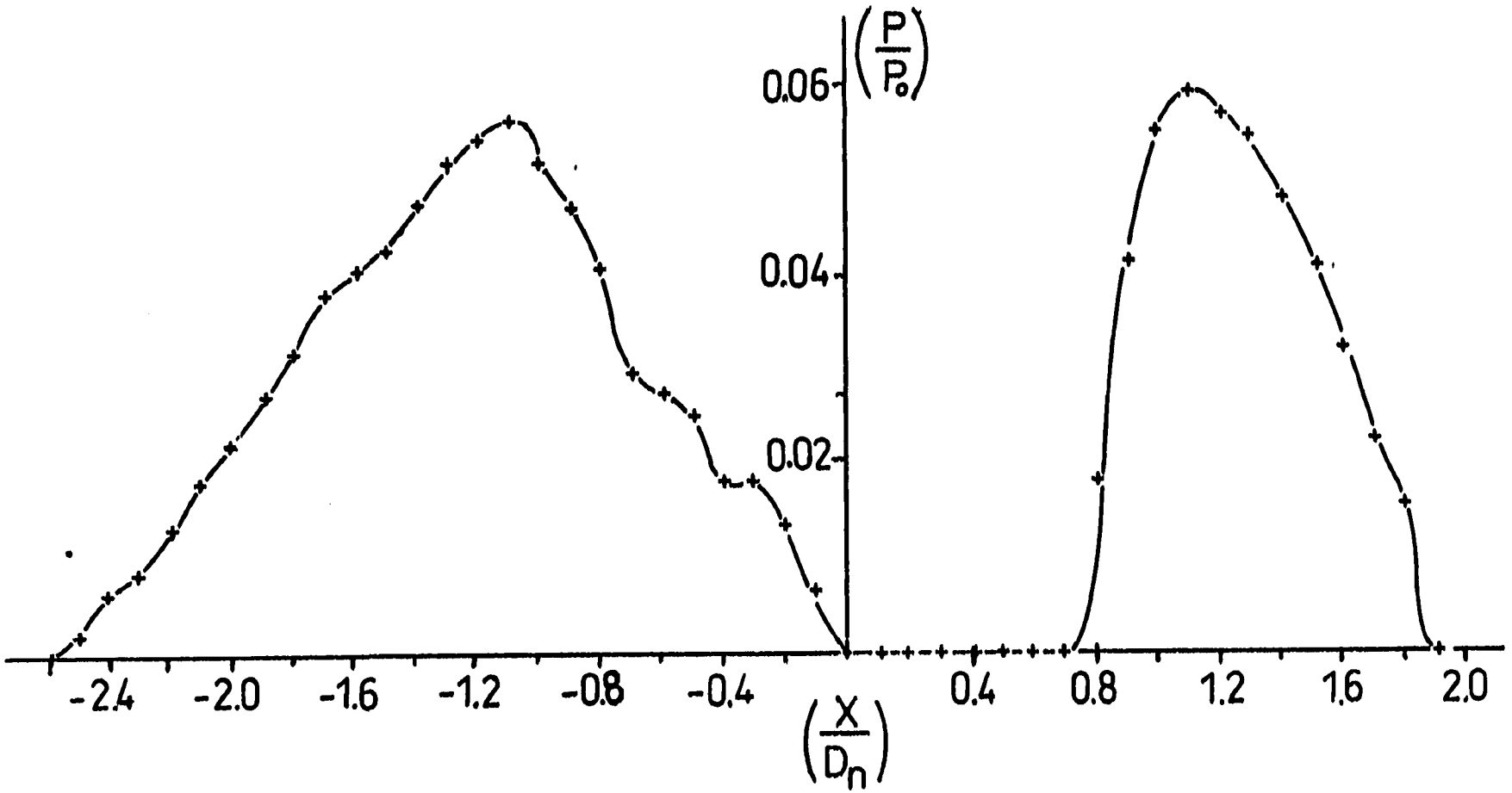

Figure 3.11B: Surface pressure along the centerline for $\theta = 20^{\circ}$, PR=2.2 ,$(Z_n/D_n) = 7.2$.

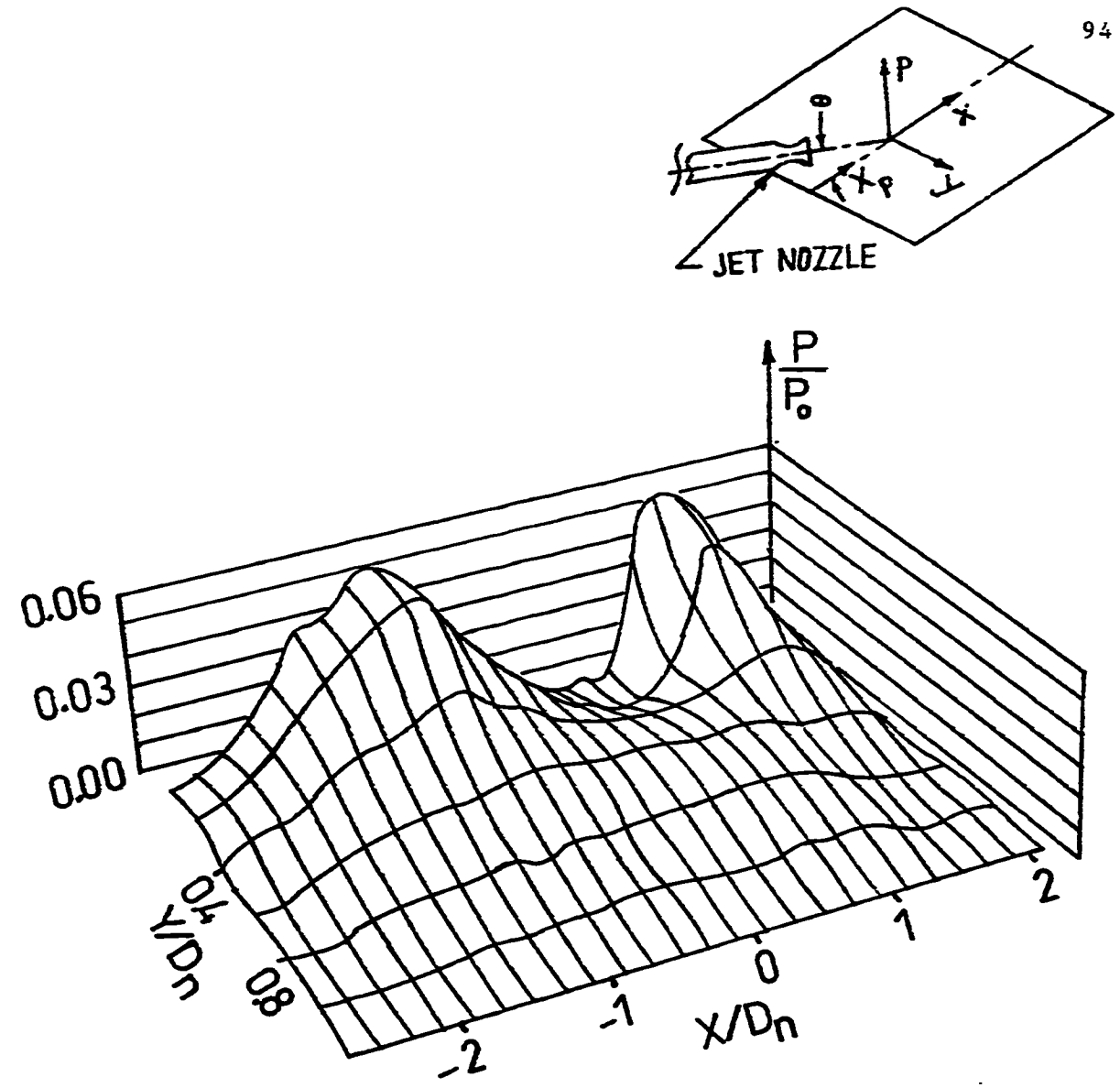

Figure 3.11C: Surface pressure distribution (half) for $\theta = 20^\circ$, PR=2.2, $(Z_n/D_n) = 7.2$.

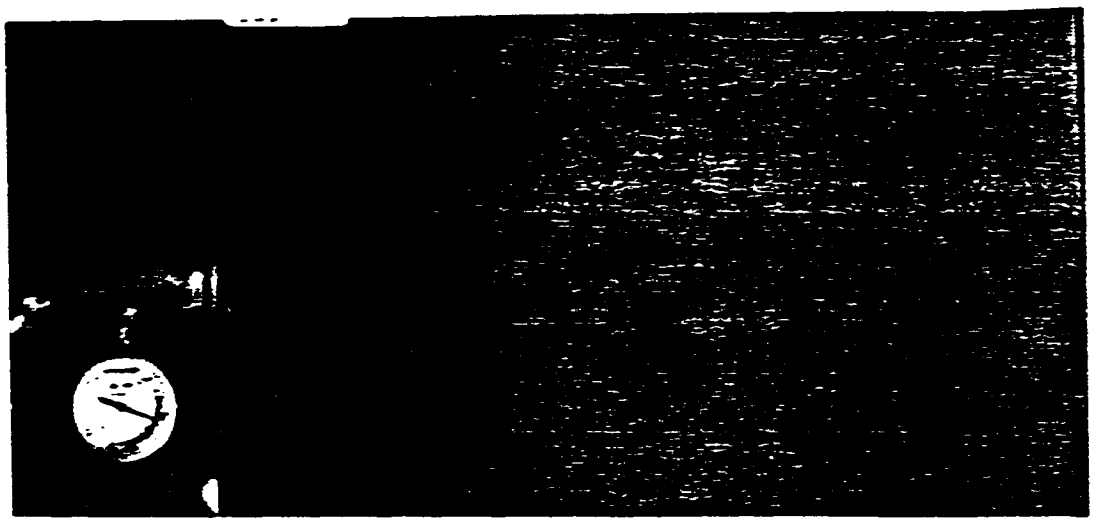

$\vdash\!\dashv D_n$

Figure 3.12 A: Surface flow visualization for $\theta=15°$, PR=2.2 and $Z_n/D_n = 7.2$.

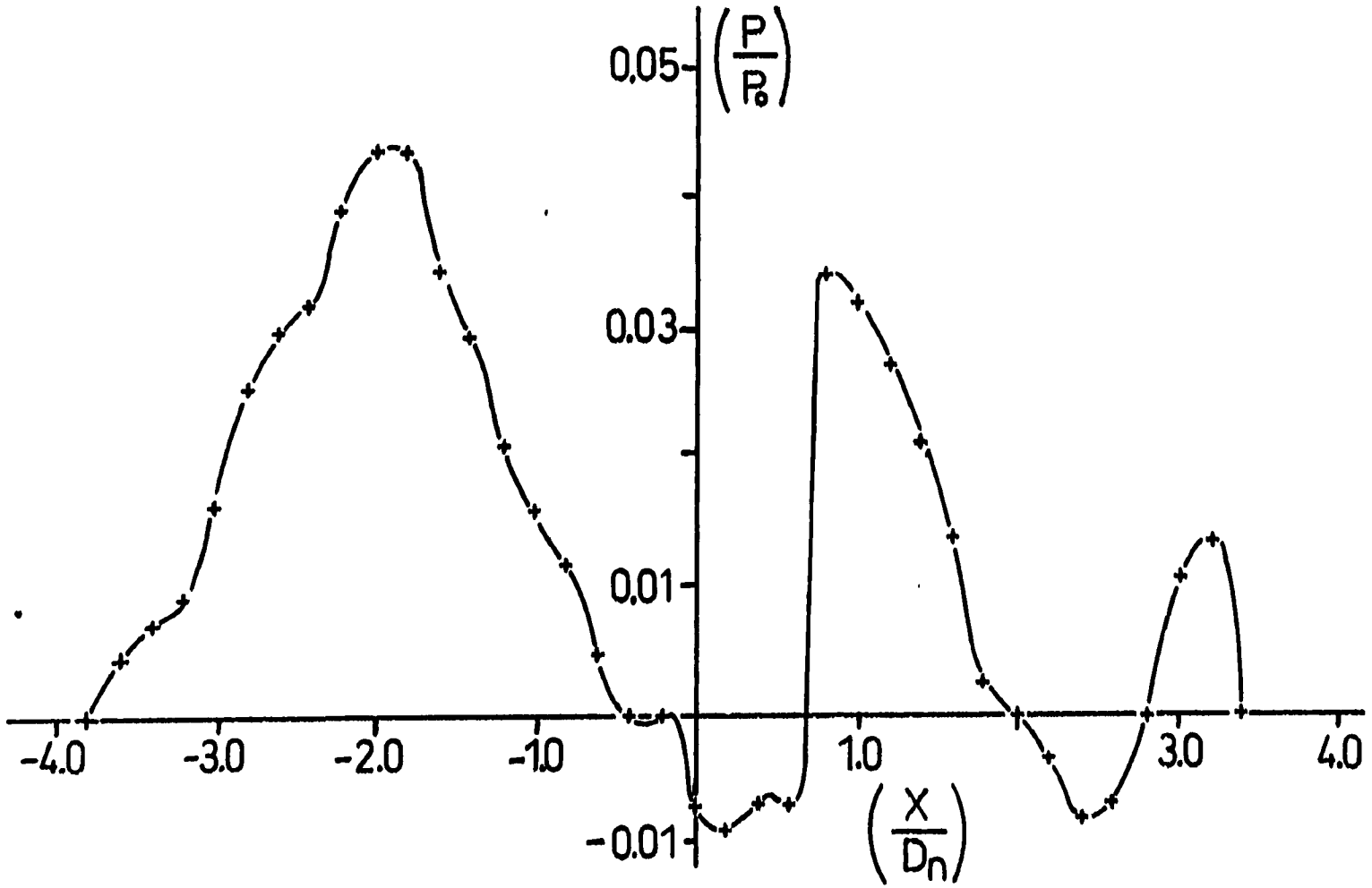

Figure 3.12 B: Surface pressure along the centerline for $\theta = 15^{\circ}$, PR = 2.2 , $(Z_n/D_n) = 7.2$.

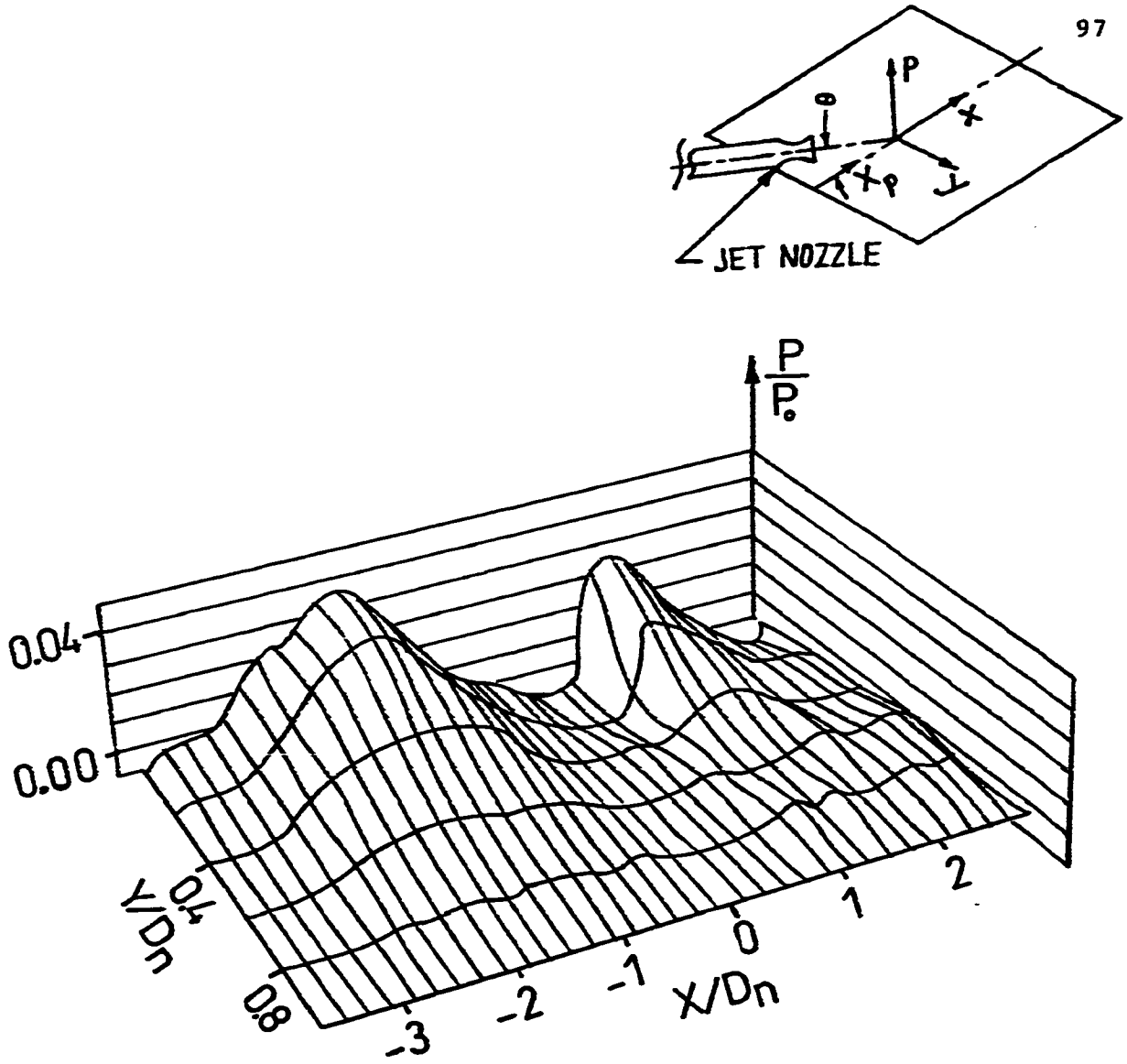

Figure 3.12C: Surface pressure distribution (half) for $\theta = 15^\circ$, PR = 2.2 , $(Z_n/D_n) = 7.2$.

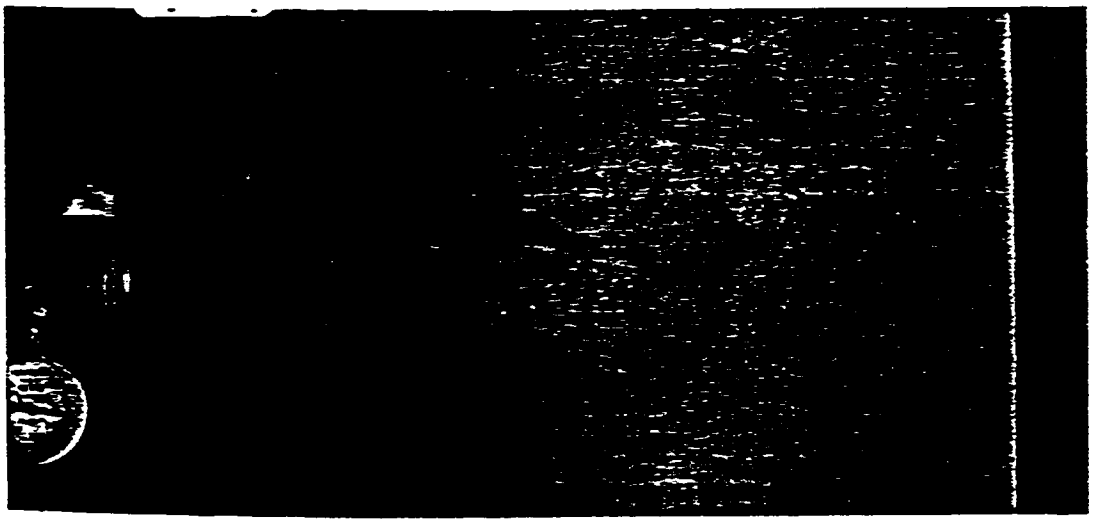

$\vdash\dashv D_n$

Figure 3.13 A: Surface flow visualization for $\theta=10°$, PR=2.2 and $Z_n/D_n=7.2$.

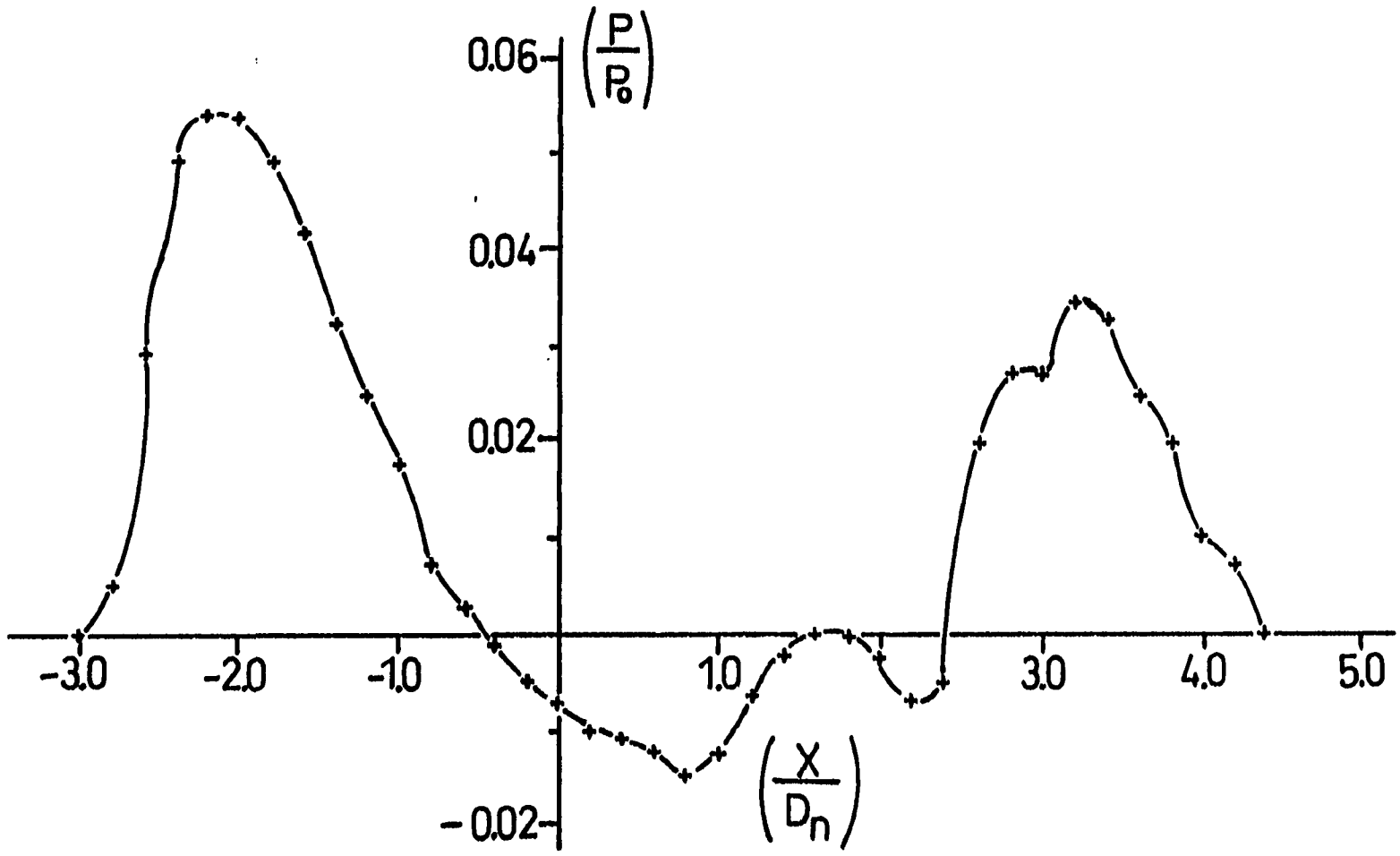

Figure 3.13B: Surface pressure along the centerline for $\theta = 10^{\circ}$, PR=2.2 ,$(Z_n/D_n) = 7.2$.

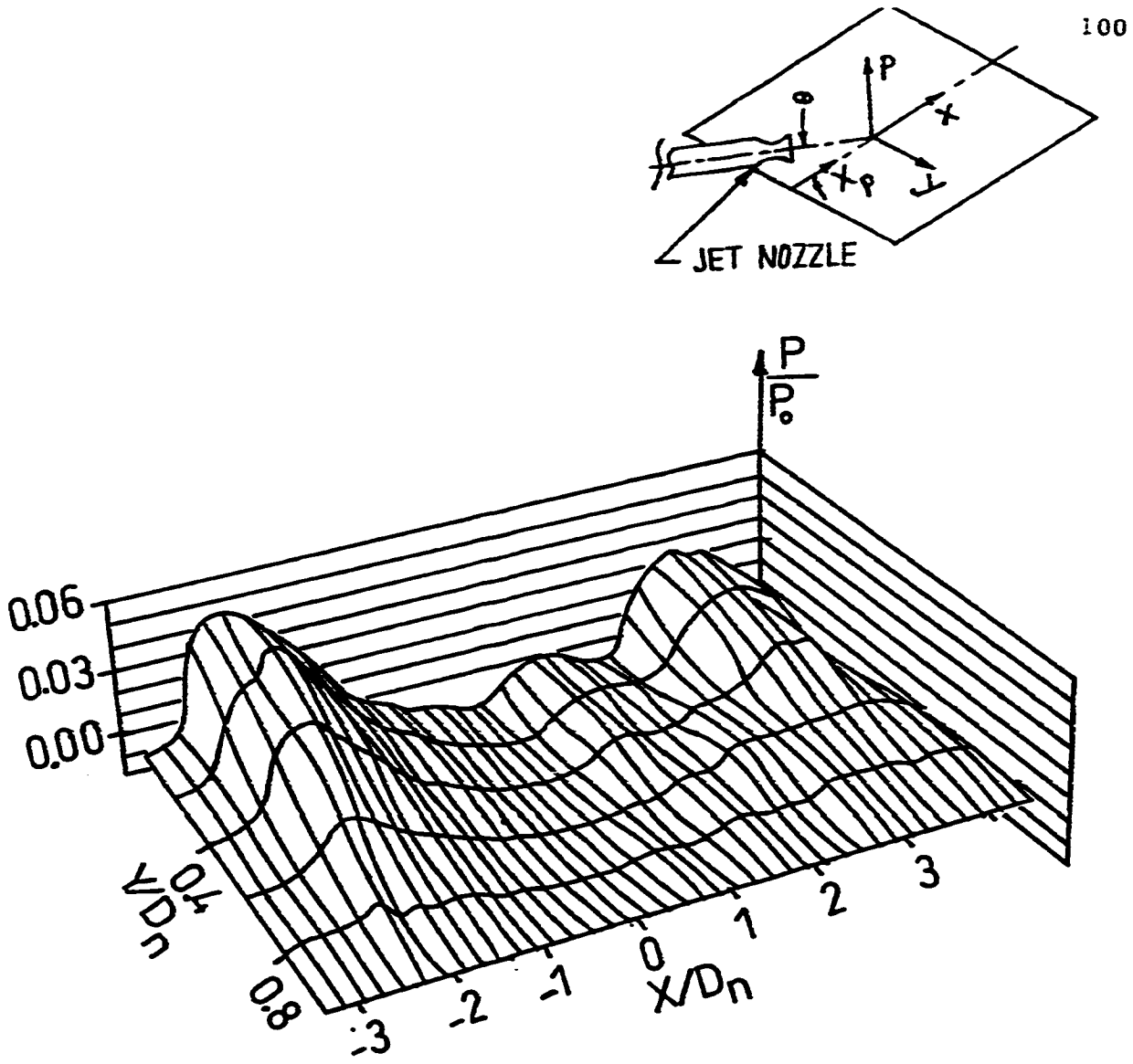

Figure3.13C: Surface pressure distribution (half) for $\theta=10^{\circ}$, $PR=2.2$, $(Z_n/D_n)=7.2$.

$\vdash D_n$

Figure 3.14 A: Surface flow visualization for $\theta = 5°$, PR= 2.2 and $Z_n/D_n = 7.2$.

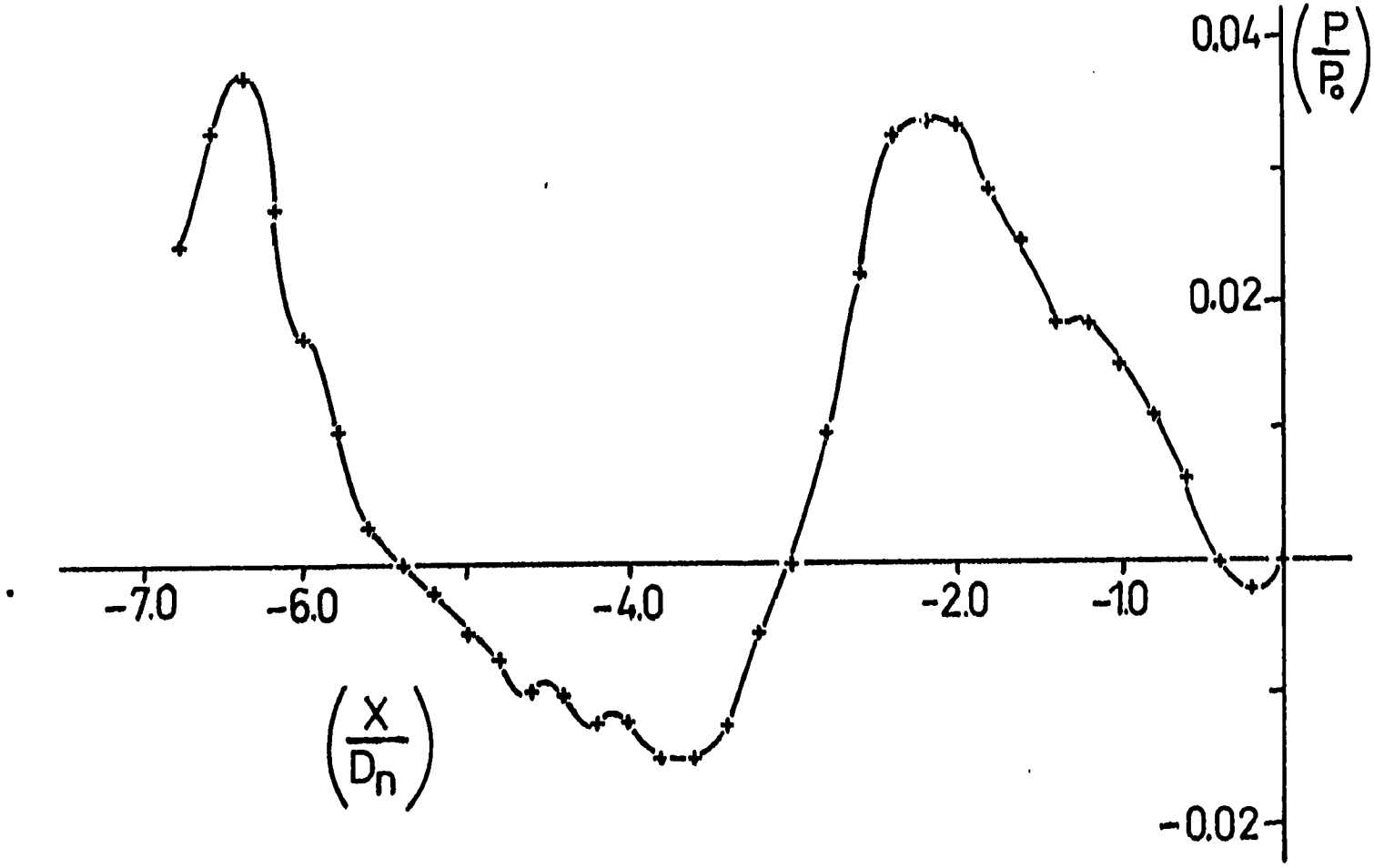

Figure3.14 B: Surface pressure along the centerline for $\theta = 5^{\circ}$, PR = 2.2 , $(Z_n/D_n) = 7.2$.

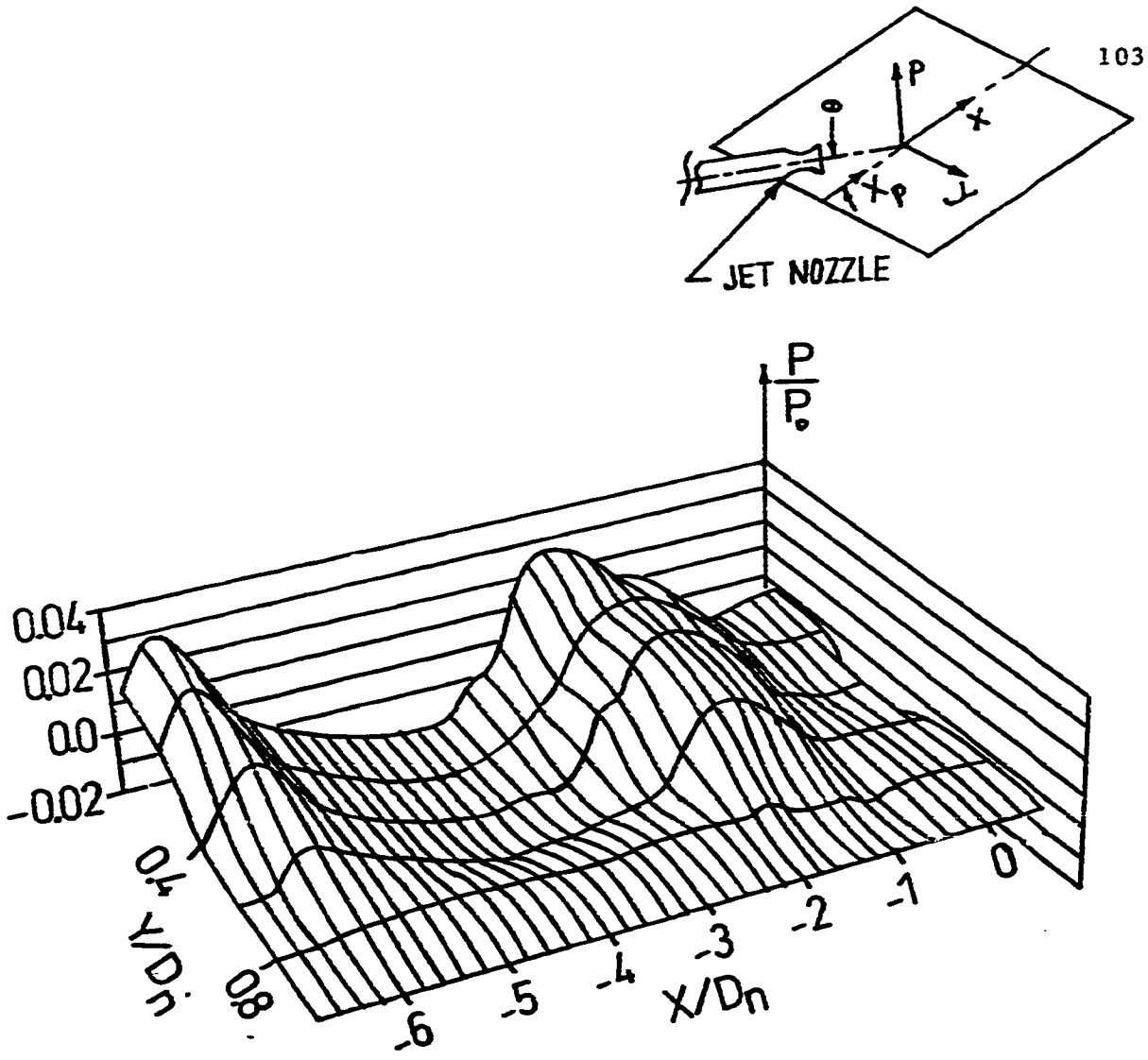

Figure 3.14C: Surface pressure distribution (half) for

$\theta = 5^\circ$, PR = 2.2 , $(Z_n/D_n) = 7.2$

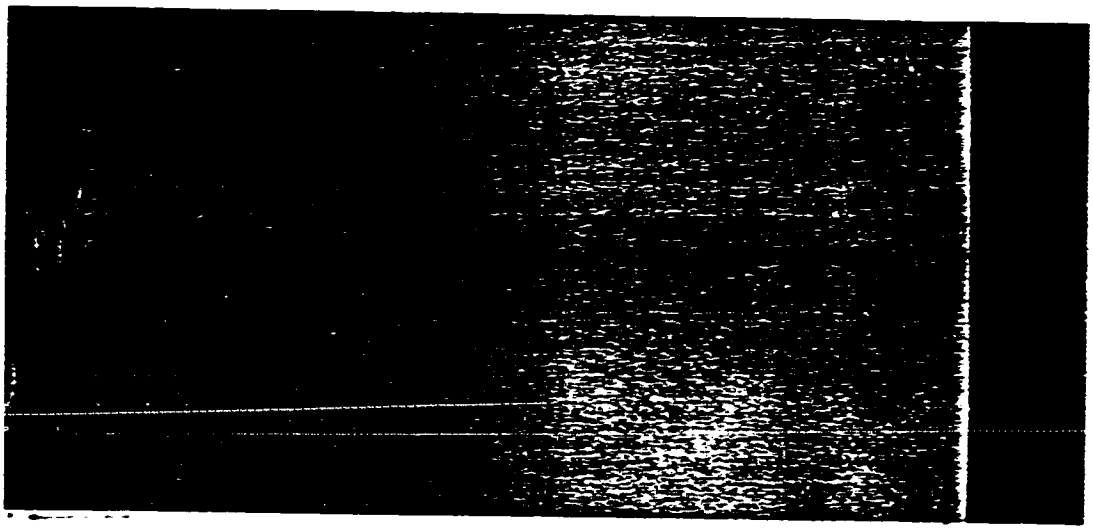

$\vdash D_n$

Figure 3.15 A : Surface flow visualization for $\theta = 0^\circ$, PR=2.2 and $h/D_n = 0.04$.

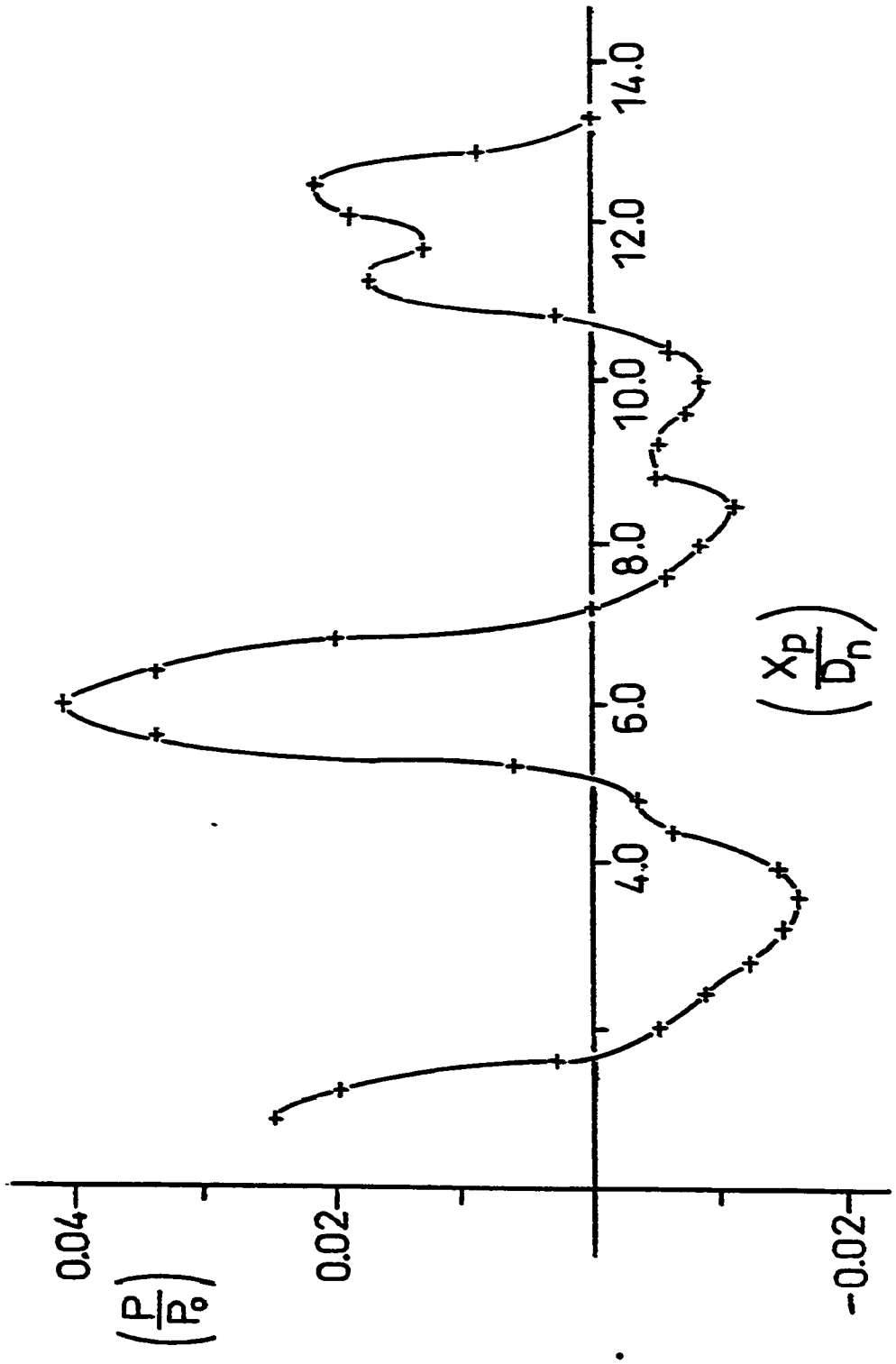

Figure3.15B : Surface pressure along the centerline for $\theta=0^0$, PR=2.2 ,(h/D_h)=0.04 .

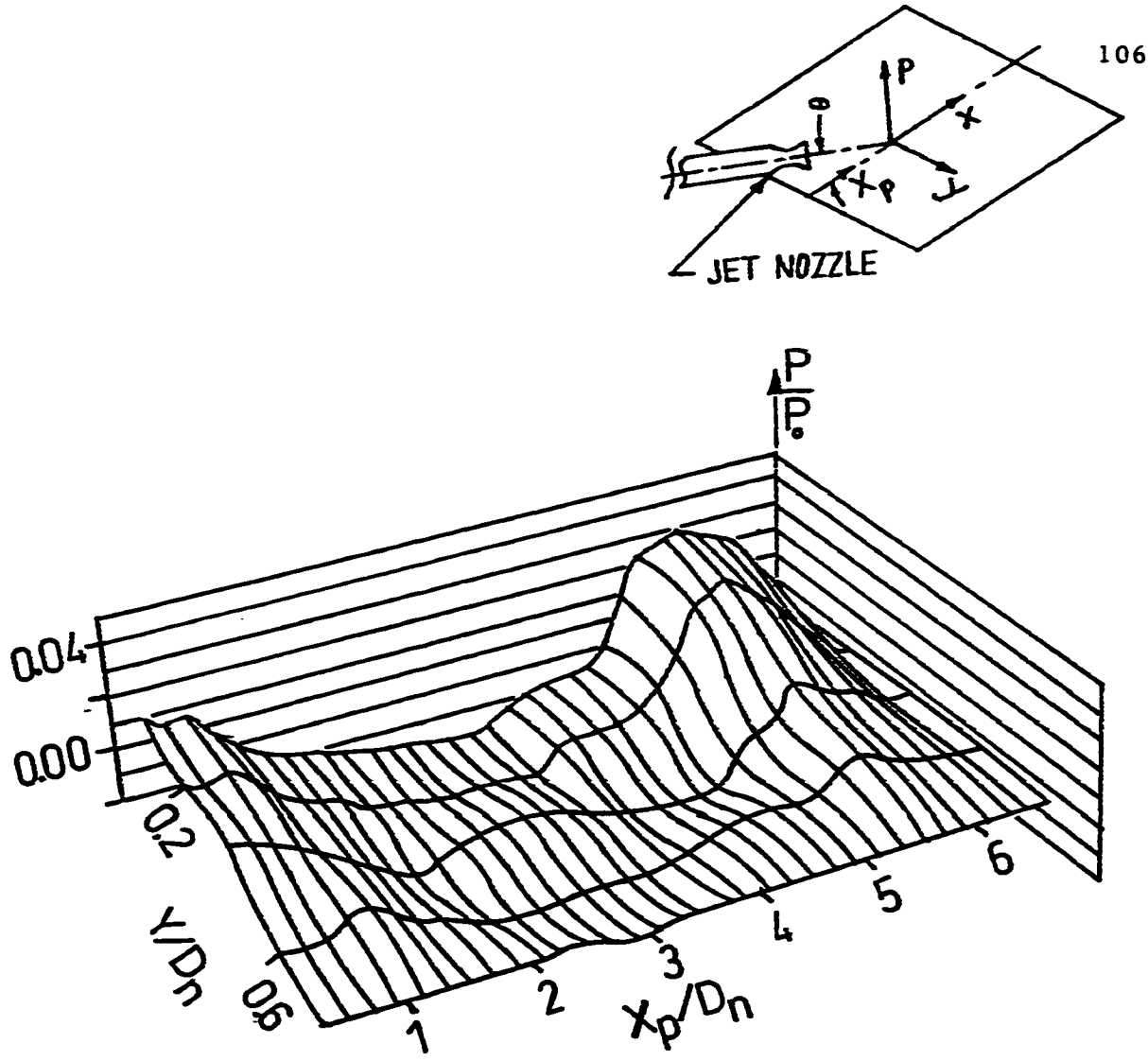

Figure 3.15C: Surface pressure distribution (half) for $\theta = 0°$, PR = 2.2, $(h/D_n) = 0.04$.

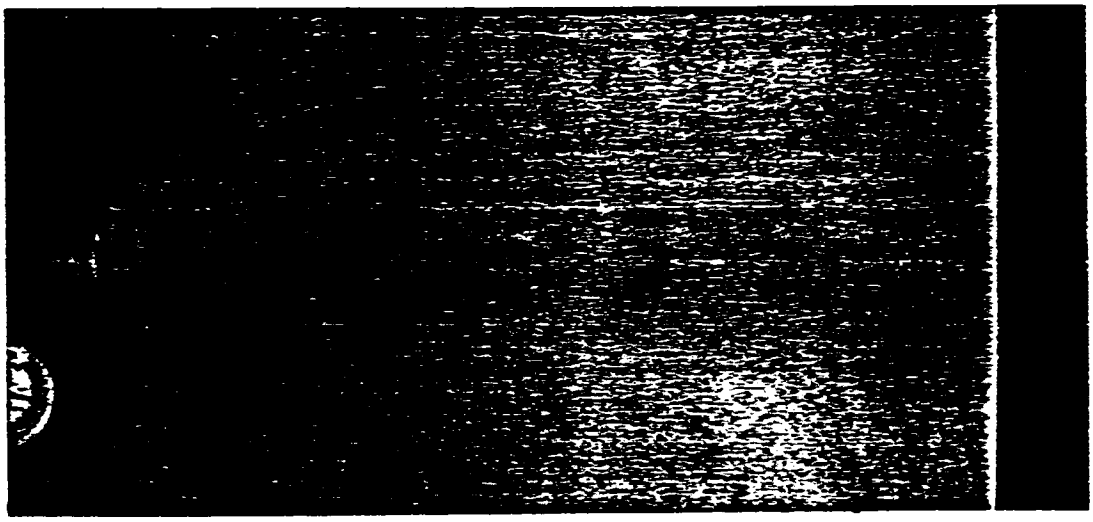

$\vdash D_h$

Figure 3.16 A : Surface flow visualization for $\theta = 0°$, $PR = 2.2$ and $h/D_h = 0.24$.

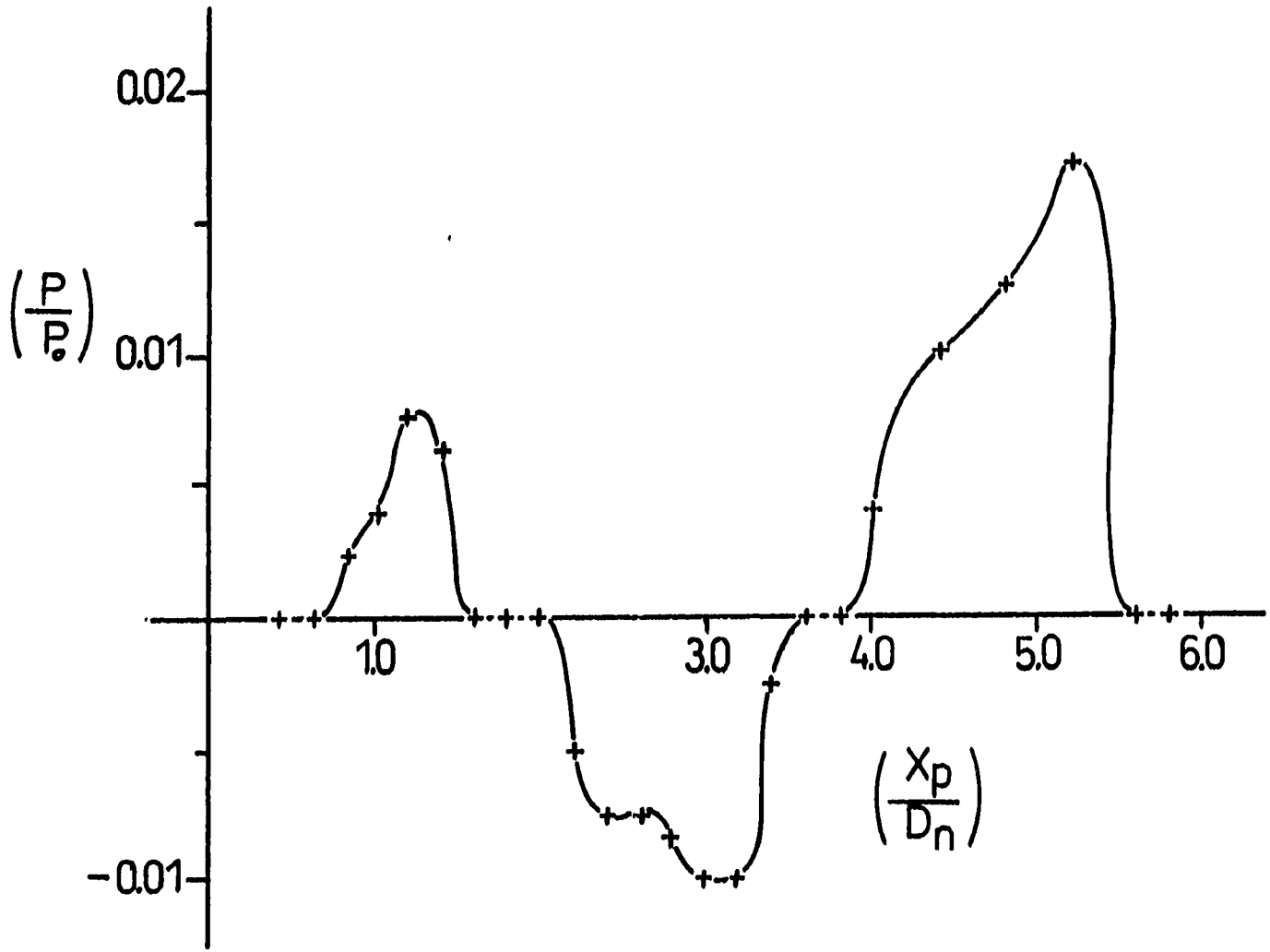

Figure3.16B: Surface pressure along the centerline for $\theta = 0^\circ$, PR=2.2 , $(h/D_n)=0.24$.

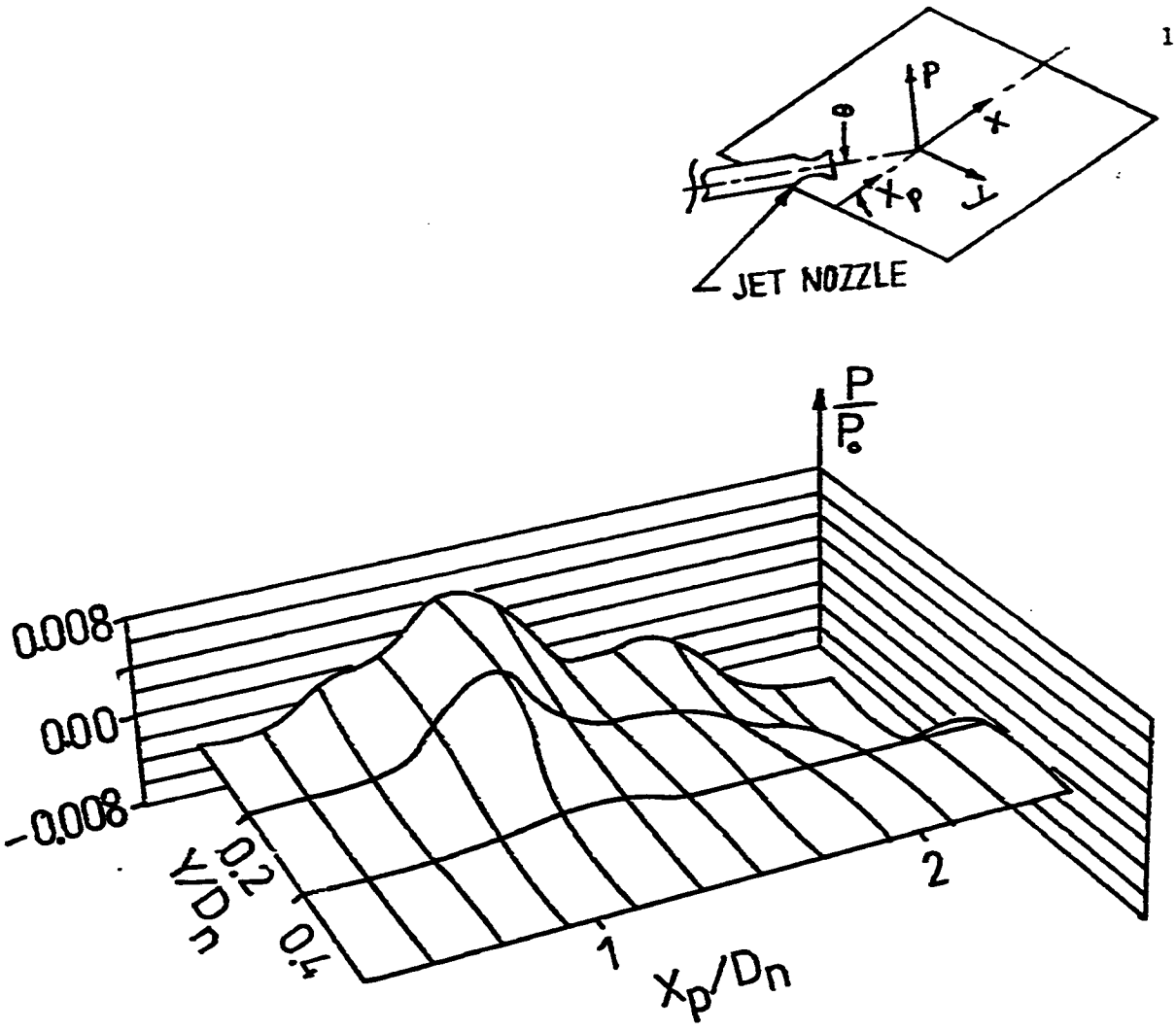

Figure 3.16C: Surface pressure distribution (half) for $\theta = 0°$, PR=2 2 , $(h/D_n) = 0.24$.

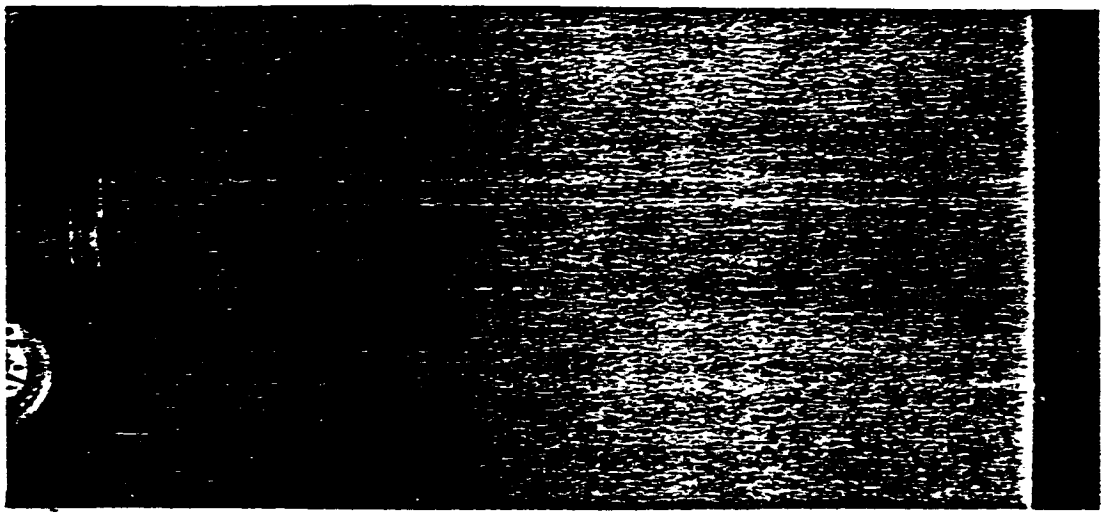

$\vdash D_n$

Figure 3.17 : Surface flow visualization for $\theta = 0°$, $PR = 2.2$ and $h/D_n = 0.5$.

$\vdash\dashv D_n$

Figure 3.18 A: Surface flow visualization for $\theta=-5^{\circ}$, PR=2.2 and $h/D_n=0.04$.

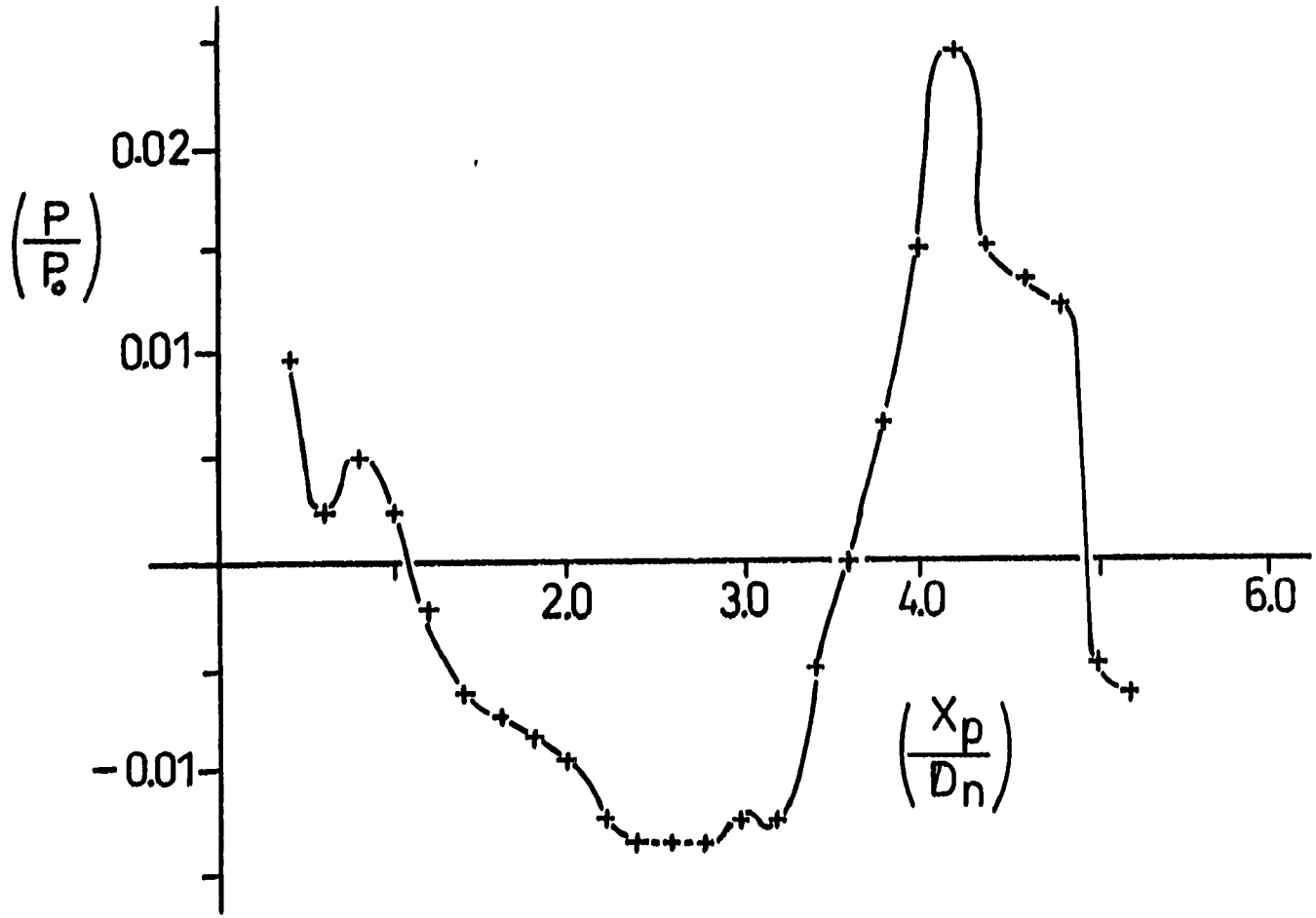

Figure 3.18B: Surface pressure along the centerline for $\theta = -5°$, PR = 2.2 , $(h/D_n) = 0.04$.

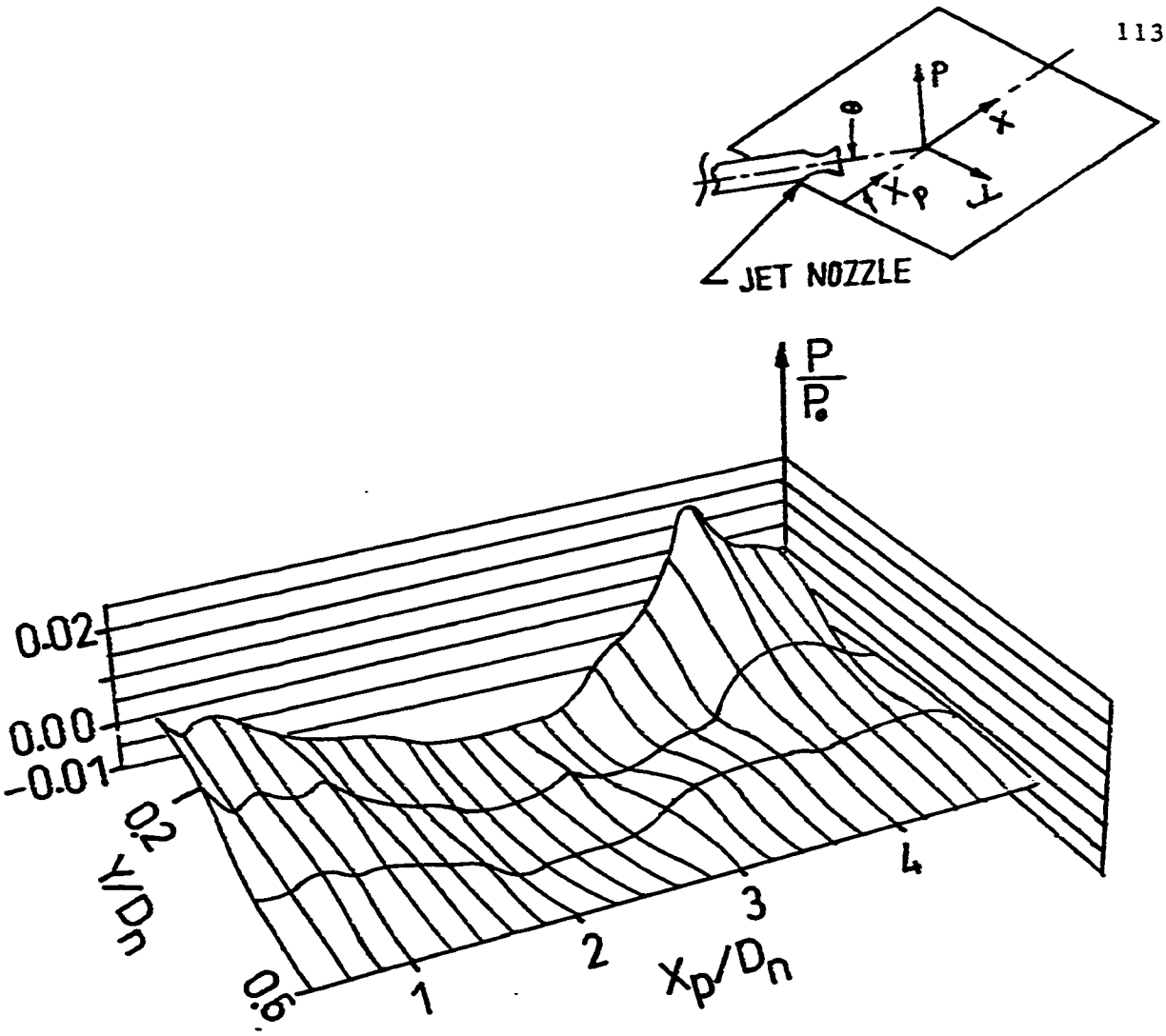

Figure 3.18C: Surface pressure distribution (half) for $\theta = -5^\circ$, PR = 2.2 , $(h/D_n) = 0.04$.

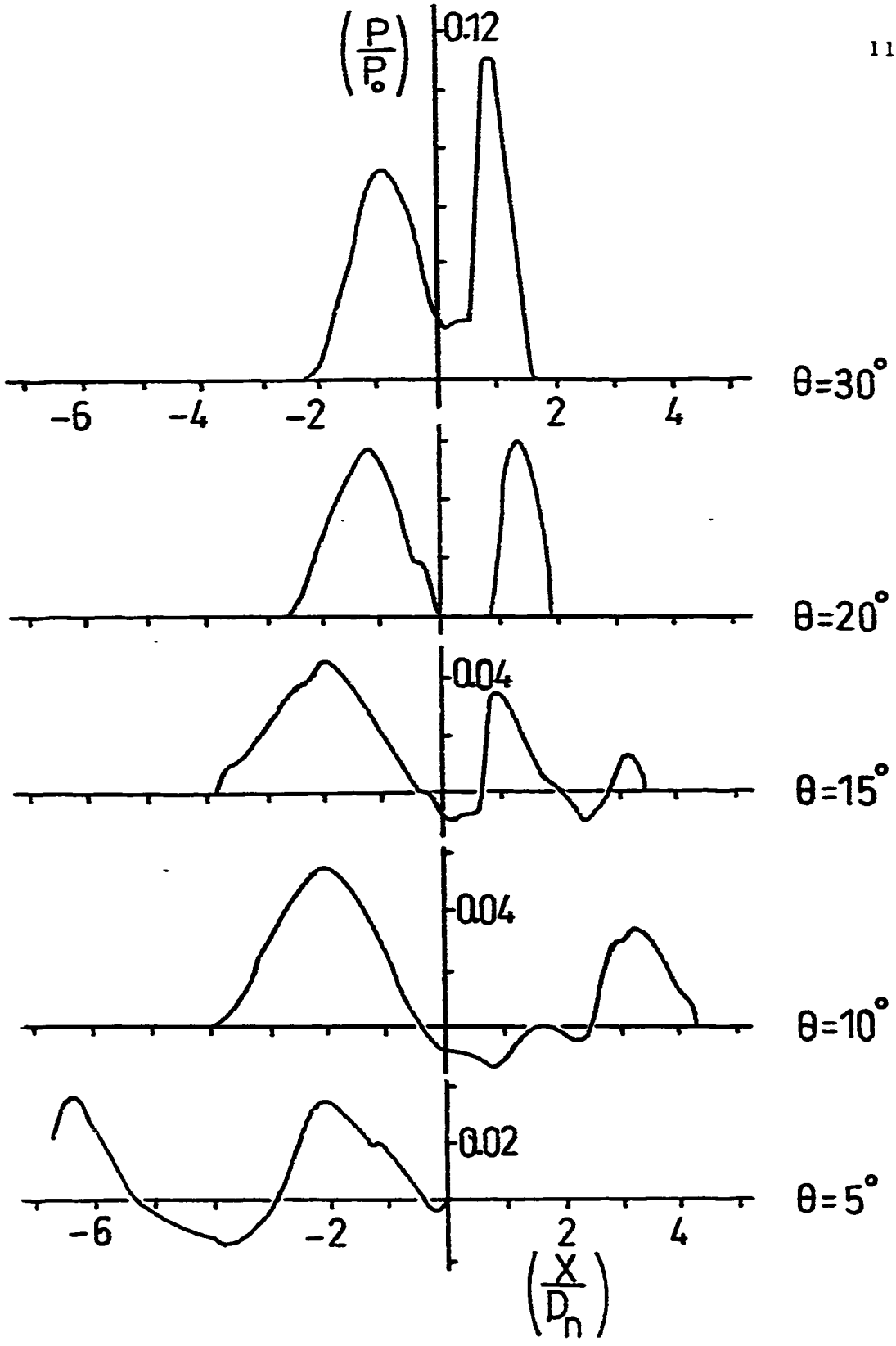

Figure 3.19 A : Center line pressure of the plate surface at different angles.

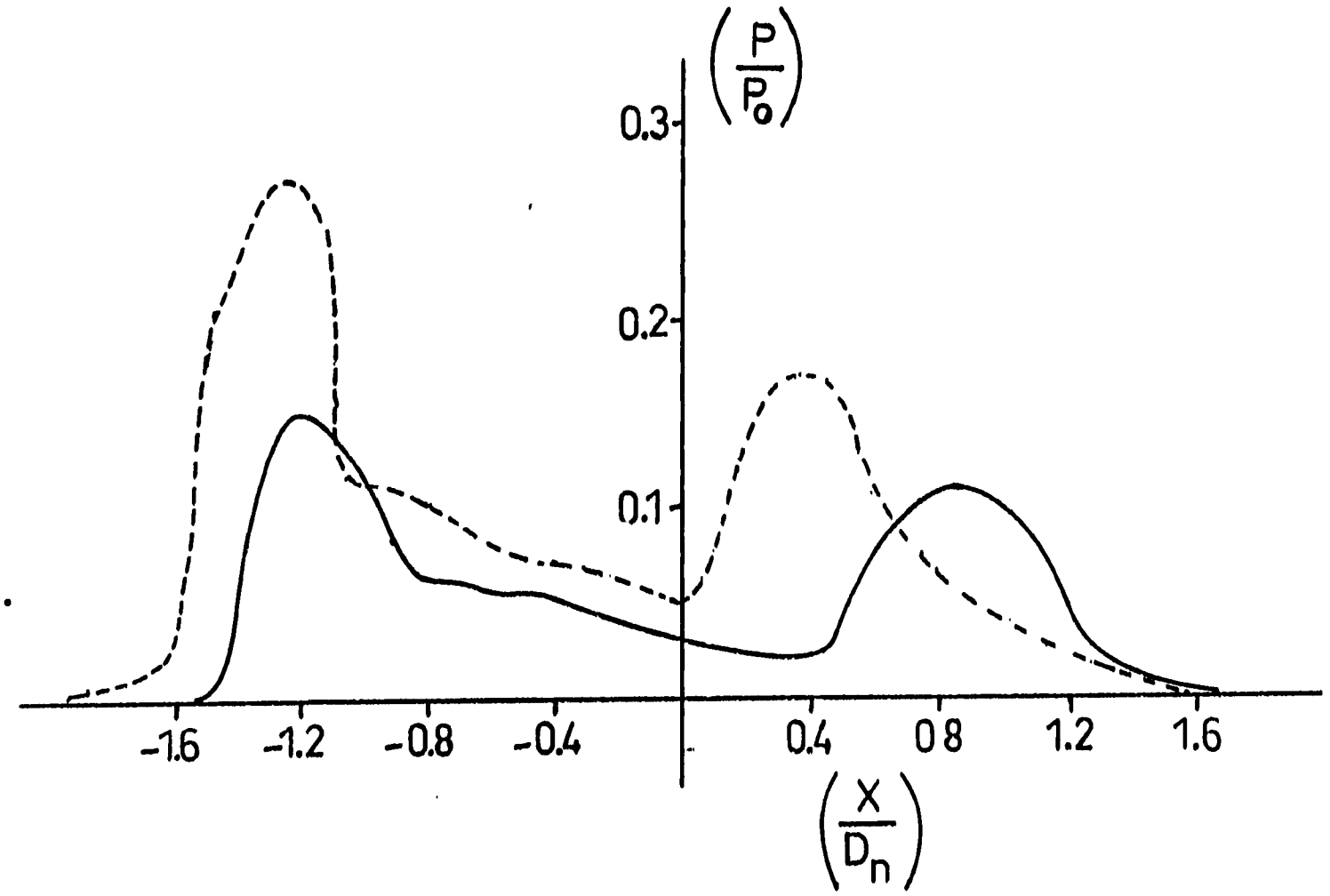

Figure 3.19 B: Center line pressure of the plate surface at $\theta=30^{\circ}$.
—— ($PR=2, Z_n/D_n=2.1$ and $M_n=2.57$); ---, ($Z_n/D_n=2, M_n=2.2$ [Lamont]).

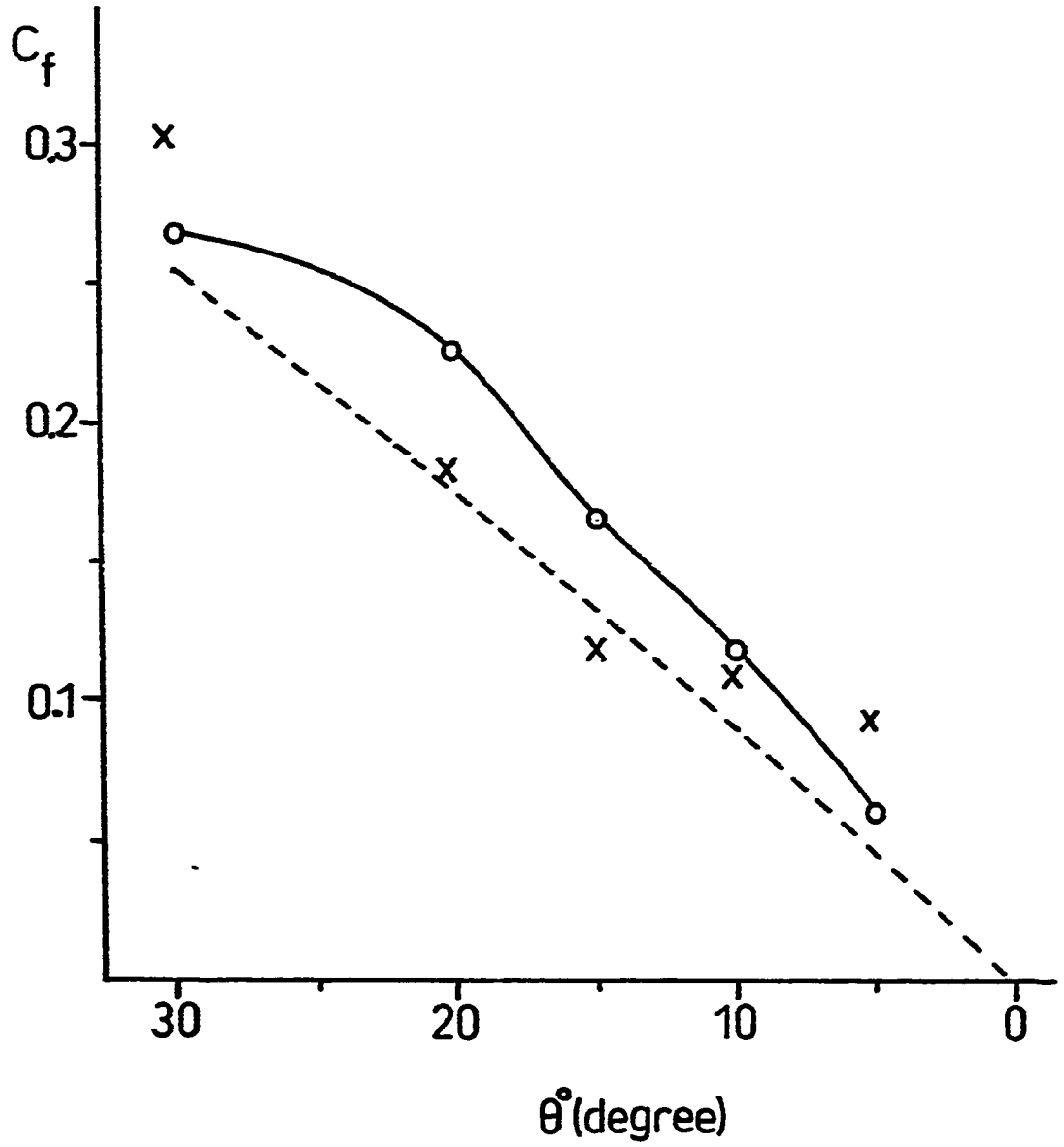

Figure 3.20: Force coefficient for PR= 2.2 , Z_n/D_n=7.2 and M_n=2.57 . --,C_{ft}[2]; -o-,C_{FS}; x,C_{FP} .